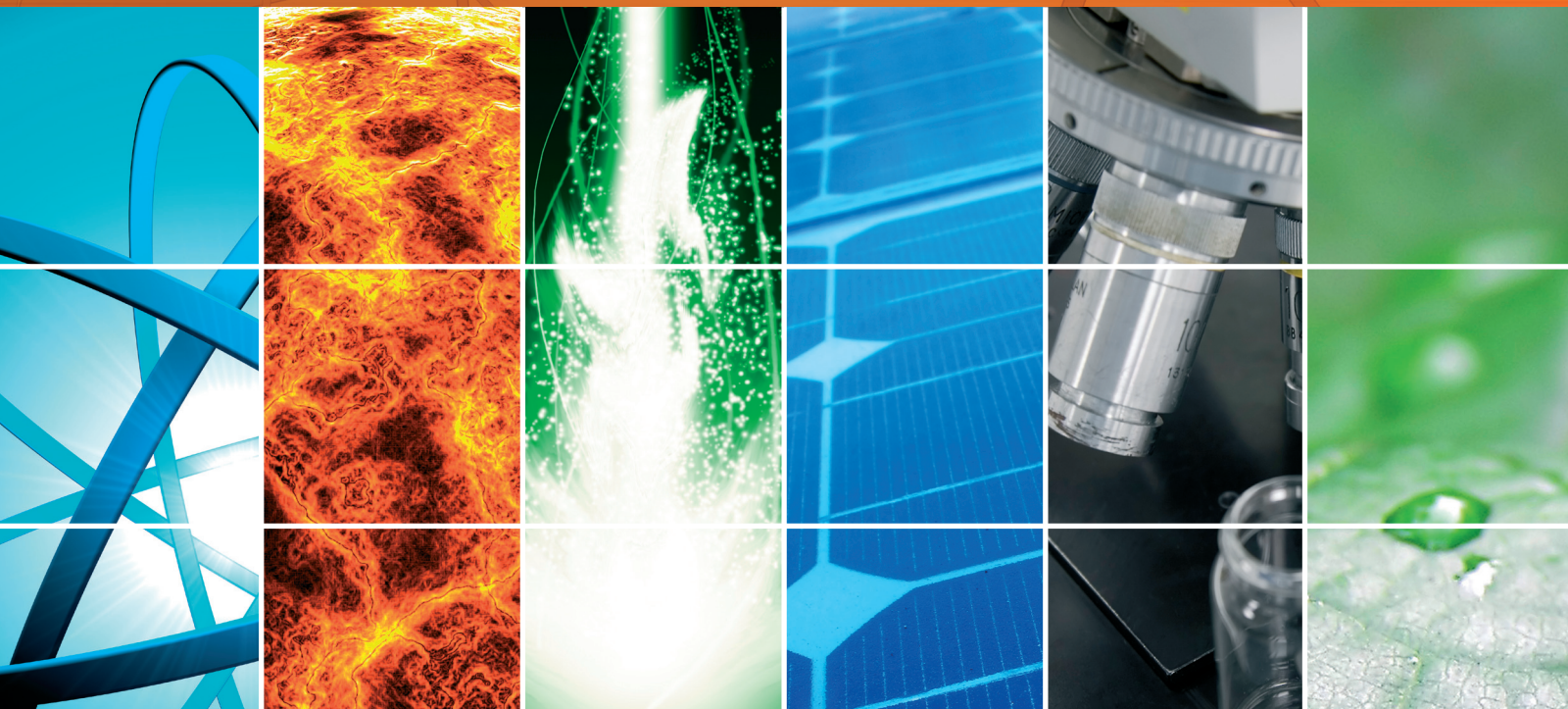


Photomedicine and Photo Nanosystems

Guest Editors: Rodica-Mariana Ion, Tebello Nyokong,
G. Gyulkhandanyan, and Danuta Wrobel





Photomedicine and Photo Nanosystems

International Journal of Photoenergy

Photomedicine and Photo Nanosystems

Guest Editors: Rodica-Mariana Ion, Tebello Nyokong,
G. Gyulkhandanyan, and Danuta Wrobel



Copyright © 2012 Hindawi Publishing Corporation. All rights reserved.

This is a special issue published in "International Journal of Photoenergy." All articles are open access articles distributed under the Creative Commons Attribution License, which permits unrestricted use, distribution, and reproduction in any medium, provided the original work is properly cited.

Editorial Board

M. Sabry Abdel-Mottaleb, Egypt
Muhammad Abdul Rauf, UAE
Nihal Ahmad, USA
Nicolas Alonso-Vante, France
Wayne A. Anderson, USA
Vincenzo Augugliaro, Italy
Detlef W. Bahnemann, Germany
Ignazio Renato Bellobono, Italy
Raghu N. Bhattacharya, USA
Gion Calzaferri, Switzerland
Vikram L. Dalal, USA
D. Demetriou Dionysiou, USA
Abderrazek Douhal, Spain
Samy El-Shall, USA
Beverley Glass, Australia
Shahed Khan, USA

Cooper H. Langford, Canada
Yuexiang Li, China
Gianluca Li Puma, UK
Panagiotis Lianos, Greece
Stefan Lis, Poland
Gilles Mailhot, France
Ugo Mazzucato, Italy
Jacek Miller, Poland
Franca Morazzoni, Italy
Leonardo Palmisano, Italy
David Lee Phillips, Hong Kong
Xie Quan, China
Tijana Rajh, USA
Saffa Riffat, UK
Peter Robertson, UK
J.-Louis Scartezzini, Switzerland

P. Joseph Sebastian, Mexico
Panagiotis Smirniotis, USA
Sam-Shajing Sun, USA
Masanori Tachiya, Japan
Gopal N. Tiwari, India
Veronica Vaida, USA
Roel van De Krol, The Netherlands
Mark van Der Auweraer, Belgium
Johannes Vos, Ireland
David Worrall, UK
F. Yakuphanoglu, Turkey
Jimmy C. Yu, Hong Kong
Klaas Zachariasse, Germany
Jincai Zhao, China

Contents

Photomedicine and Photo Nanosystems, Rodica-Mariana Ion, Tebello Nyokong, G. Gyulkhandanyan, and Danuta Wrobel
Volume 2012, Article ID 127309, 1 page

Inhibitory Effects of Far-Infrared Irradiation Generated by Ceramic Material on Murine Melanoma Cell Growth, Ting-Kai Leung, Chin-Feng Chan, Ping-Shan Lai, Chih-Hui Yang, Chia-Yen Hsu, and Yung-Sheng Lin
Volume 2012, Article ID 646845, 8 pages

Energy Conversion in Protocells with Natural Nanoconductors, Jian Xu, T. Kyle Vanderlick, and David A. LaVan
Volume 2012, Article ID 425735, 10 pages

Development of Polymeric Cargo for Delivery of Photosensitizer in Photodynamic Therapy, Byoung-chan Bae and Kun Na
Volume 2012, Article ID 431975, 14 pages

Nanophotonics for Molecular Diagnostics and Therapy Applications, João Conde, João Rosa, João C. Lima, and Pedro V. Baptista
Volume 2012, Article ID 619530, 11 pages

Mannan-Modified PLGA Nanoparticles for Targeted Gene Delivery, Fansheng Kong, Linfu Ge, Ximin Liu, Ning Huang, and Fang Zhou
Volume 2012, Article ID 926754, 7 pages

Editorial

Photomedicine and Photo Nanosystems

Rodica-Mariana Ion,¹ Tebello Nyokong,² G. Gyulkhandanyan,³ and Danuta Wrobel⁴

¹ *Analytical Department, National Institute for Chemical and Petrochemical Research, 060021 Bucharest, Romania*

² *Chemistry Department, Rhodes University, Grahamstown 6140, South Africa*

³ *Institute of Biochemistry, National Academy of Sciences of Armenia, 0014 Yerevan, Armenia*

⁴ *Department of Molecular Physics, Institute of Physics, Poznan University of Technology, 60-965 Poznań, Poland*

Correspondence should be addressed to Rodica-Mariana Ion, rodica_ion2000@yahoo.co.uk

Received 15 March 2012; Accepted 15 March 2012

Copyright © 2012 Rodica-Mariana Ion et al. This is an open access article distributed under the Creative Commons Attribution License, which permits unrestricted use, distribution, and reproduction in any medium, provided the original work is properly cited.

Considered as a key technology of the 21st century, the nanotechnology is considered a useful tool that may help to develop new and efficient applications, especially in nanomedicine.

Nanomedicine exploits the physical, chemical, and biological properties of materials at the nanometer scale. It is expected to have its substantial impact on preventive medicine, diagnostics, medical imaging, therapy, and drug delivery.

In this special issue of International Journal of Photoenergy, there were presented some basic and engineering researches in the field of nanomedicine and the related biotherapeutic discovery.

This issue covered current topics and recent progress in targeted nanomedicine and therapeutic concepts, photodynamic therapy and regenerative medicine.

The Authors have submitted original research and articles describing the latest scientific and technological research results in the following topics. The topics included the following:

- (i) nanostructures and biomaterials,
- (ii) nanomedicine,
- (iii) nanobiotechnology and nanomedicine,
- (iv) drug discovery and development.

In the name of the editorial team, I want to express my appreciation about the quality, originality, and novelty of works submitted by the authors, and in this respect, we welcome the

proposal of the journal to publish a special number dedicated to the field of nanomedicine.

*Rodica-Mariana Ion
Tebello Nyokong
G. Gyulkhandanyan
Danuta Wrobel*

Research Article

Inhibitory Effects of Far-Infrared Irradiation Generated by Ceramic Material on Murine Melanoma Cell Growth

Ting-Kai Leung,¹ Chin-Feng Chan,² Ping-Shan Lai,³ Chih-Hui Yang,⁴
Chia-Yen Hsu,³ and Yung-Sheng Lin²

¹Department of Radiology, School of Medicine, Taipei Medical University and Hospital, Taipei 110, Taiwan

²Department of Applied Cosmetology and Master Program of Cosmetic Science, Hungkuang University, Taichung 433, Taiwan

³Department of Chemistry, National Chung Hsing University, Taichung 402, Taiwan

⁴Department of Biological Science and Technology, I-Shou University, Kaohsiung 824, Taiwan

Correspondence should be addressed to Yung-Sheng Lin, liny@sunrise.hk.edu.tw

Received 20 April 2011; Revised 9 July 2011; Accepted 9 July 2011

Academic Editor: Rodica-Mariana Ion

Copyright © 2012 Ting-Kai Leung et al. This is an open access article distributed under the Creative Commons Attribution License, which permits unrestricted use, distribution, and reproduction in any medium, provided the original work is properly cited.

The biological effects of specific wavelengths, so-called “far-infrared radiation” produced from ceramic material (cFIR), on whole organisms are not yet well understood. In this study, we investigated the biological effects of cFIR on murine melanoma cells (B16-F10) at body temperature. cFIR irradiation treatment for 48 h resulted in an 11.8% decrease in the proliferation of melanoma cells relative to the control. Meanwhile, incubation of cells with cFIR for 48 h significantly resulted in 56.9% and 15.7% decreases in the intracellular heat shock protein (HSP)70 and intracellular nitric oxide (iNO) contents, respectively. Furthermore, cFIR treatment induced 6.4% and 12.3% increases in intracellular reactive oxygen species stained by 5-(and 6)-carboxyl-2',7'-dichlorodihydrofluorescein diacetate and dihydrorhodamine 123, respectively. Since malignant melanomas are known to have high HSP70 expression and iNO activity, the suppressive effects of cFIR on HSP70 and NO may warrant future interest in antitumor applications.

1. Introduction

Melanomas are one of the major malignant tumors of Caucasian people, with approximately 60,000 new cases of invasive melanoma being diagnosed in the USA each year. According to a WHO report, about 48,000 melanoma-related deaths occur worldwide per year. Melanocytes are normally present in the skin, and they are responsible for producing the dark pigment, melanin. Despite many years of intensive laboratory and clinical research, the greatest chance of a cure is early surgical resection of thin tumors.

Far-infrared radiation (FIR) is the major heat-transmitting radiation of sunlight at wavelengths between 3 μm and 1 mm as defined by the International Commission on Illumination (CIE 1987). FIR, especially that at the range of 3~14 μm , is termed “life light” and has many biological effects. Previous studies demonstrated that FIR has a wide range of applications including increasing the microcirculation, promoting wound healing, modulating sleep, treating

depression, inhibiting tumor proliferation, and processing food [1–6]. Recently, FIR use has been growing in popularity for its health-promoting properties and is an alternative remedy in Japan, China, Taiwan, and Korea. However, the mechanisms underlying these biological effects are still poorly understood. There are few reports investigating the biological effects of FIR, especially those concerned with the effect on cancer cells, such as melanomas.

This study is aimed to investigate the possible biological effects of FIR produced by ceramic material (cFIR) on murine melanoma cells using the B16-F10 cell line. We focused on the effects on cell viability, intracellular heat shock protein (HSP)70, intracellular nitric oxide (iNO), inducible nitric oxide synthase (iNOS), and reactive oxygen species (ROS). The direct suppressive effect on melanoma cells by FIR was investigated. The inhibition of HSP70 synthesis and iNO in tumor cells shows the possible utility of FIR in cancer therapy. After a literature review, we discuss the possible physiological mechanism behind these observations

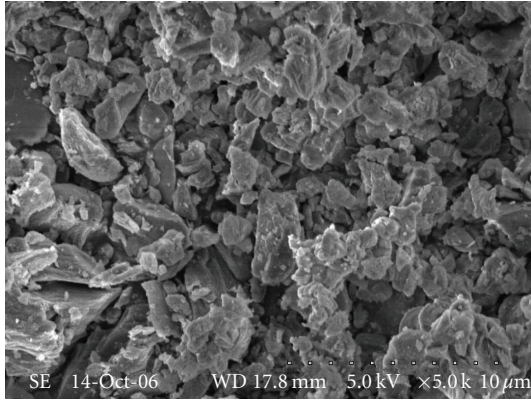


FIGURE 1: SEM picture of cFIR ceramic powder used in this study.

based on past studies detailing related biomolecular factors and future applications.

2. Methods

2.1. Chemicals and Reagents. B16-F10, a murine melanoma cell line (ATCC: CRL-6475), was procured from the Biore-source Collection and Research Center (Hsinchu, Taiwan). Dulbecco's modified Eagle's medium (DMEM), fetal bovine serum (FBS), sodium bicarbonate, antibiotic/anti-mycotic solution, and trypsin/0.52 mM EDTA solution were purchased from Gibco (Grand Island, NY, USA). 3-(4,5-Dimethylthiazol-2-yl)-2,5-diphenyltetrazolium bromide (MTT), phosphate-buffered saline (PBS), dimethyl sulfoxide (DMSO), Hoechst 33342, and phenylmethylsulfonyl fluoride (PMSF) were purchased from Sigma (St. Louis, Mo, USA). The rabbit antihuman HSP70 antibody, anti- β actin antibody, and anti-iNOS antibody were obtained from Stressgen (Victoria, BC, Canada), Abcam (Cambridge, UK), and Calbiochem (San Diego, USA), respectively. 4-Amino-5-methylamino-2',7'-difluorofluorescein (DAF-FM) diacetate and dihydrorhodamine 123 were obtained from Invitrogen (Branford, Conn, USA). 5-(and 6)-Carboxyl-2',7'-dichlorodihydrofluorescein diacetate (Carboxy-H2DCFDA) was obtained from Molecular Probes (Eugene, Ore, USA).

2.2. cFIR Ceramic Powder. As previously reported [7–9], the cFIR ceramic powder consisted of microsized particles (Figure 1) made from numerous mineral oxides, including aluminum oxide, ferric oxide, magnesium oxide, and calcium carbonate. These crushed and irregular-shaped microparticles had an average size of 4.39 μ m. The cFIR emissivity (the ratio of the radiation energy irradiated from a sample relative to an ideal black body, as described by Planck's law) was determined using an SR5000 infrared spectroradiometer (CI, Migdal HaEmek, Israel). The amount of FIR energy reaching the cells was 0.11 J/cm² with FIR at wavelengths between 3 and 14 μ m. Prior to use in cell culture, 180 g of cFIR powder was placed in a plastic bag and sterilized with 75% ethanol and UV light.

2.3. Cell Culture. B16-F10 cells were cultured in DMEM supplemented with 10% FBS, 1.5 g/L sodium bicarbonate,

4.5 g/L glucose, 100 U/mL penicillin, 0.1 mg/mL streptomycin, and 0.25 μ g/mL amphotericin B at 37°C with 5% CO₂ in a humidified incubator. Cells were subcultured at a ratio of 1:5 every third or fifth day. To evaluate the effect of the cFIR powder, cultured cells were divided into a cFIR group and control group that received no cFIR treatment. B16-F10 cells were seeded at a density of 2×10^5 cells/well in 6-well plates. Following previous reports [7–9], enclosed FIR powder was uniformly distributed in a plastic bag, and the bag was inserted directly beneath the cell culture dish in the cFIR group. RAW 264.7 macrophages were used as the positive control to study the antitumor effects.

2.4. Cell Viability and Proliferation. The cell survival rate was quantified using a colorimetric MTT assay that measured mitochondrial activity in viable cells. This method was performed as previously described with slight modifications [10]. In brief, B16-F10 cells were seeded at a density of 2×10^5 cells/well in 6-well plates. Cells were then incubated for 48 h. To evaluate the effect of the cFIR powder, cultured cells were divided into three groups: group C was the control without cFIR influence; group FP24 consisted of cells cultured in a normal environment for 24 h and then cultured with the cFIR powder for another 24 h; group FP48 consisted of cells cultured with the cFIR powder for 48 h. MTT was freshly prepared at 1 mg/mL in PBS, and 800 μ L was added to each well and incubated at 37°C for 4 h. Then, 800 μ L of DMSO was added to each well to dissolve the MTT-formazan crystals. After incubation at 37°C for 10 min, the solution was transferred to a 96-well enzyme-linked immunosorbent assay (ELISA) plate, and the absorbance was measured with a spectrophotometer at 540 nm. The optical density (O.D.) of the control cells was considered to be 100%.

2.5. HSP70. The primary polyclonal rabbit antihuman HSP70 antibody and rabbit anti- β actin antibody were used at a 1:2000 dilution. Blots were developed using a horseradish peroxidase-conjugated goat antirabbit secondary antibody and enhanced chemiluminescence (ECL system, Amersham Biosciences). Analysis was then performed, and differences between the control and experimental groups were quantitatively determined by Winlight32 software (Berthold Technologies).

2.6. iNO. The experimental group included 18 plates with B16-F10 cells receiving cFIR treatment for 48 h. The control group had the same condition but without cFIR treatment. Cells were then stained with DAF-FM diacetate for fluorescence measurements. Fluorescence was analyzed by FACScan flow cytometer (Becton Dickinson, USA), and fluorescence intensity profiles and the mean fluorescence intensities of different treatments of B16-F10 cells were determined for the data analysis.

2.7. iNOS. The iNOS expression was determined by western blotting analysis. At the end of the incubation period, cells were washed with PBS, scraped with a rubber policeman, and sonicated for 2 min in ice-cold solution. Proteins (50 μ g/lane) were separated by electrophoresis on an 8% acrylamide gel and transferred to nitrocellulose, which was then incubated

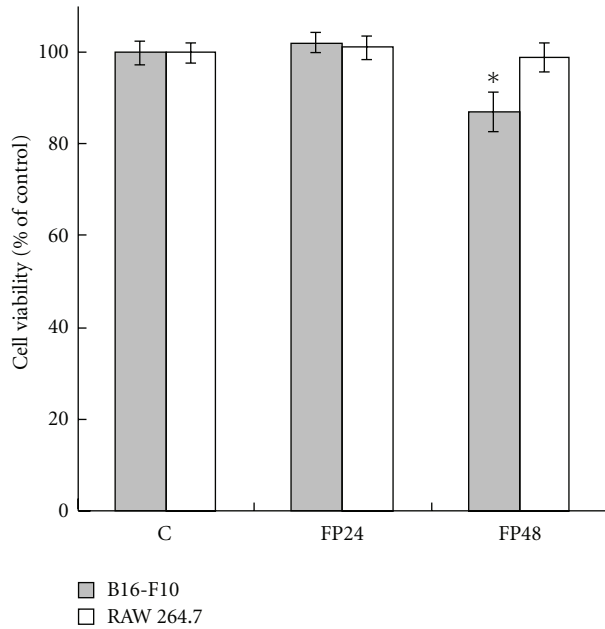


FIGURE 2: The effect of cFIR on B16-F10 and RAW 264.7 cell viability. Groups C, FP 24, and FP48 received cFIR treatment for 0, 24, and 48 h, respectively. Values are expressed as the mean and standard deviation, and the difference between groups was tested using the Wilcoxon test.

with an anti-iNOS antibody at a 1:200 dilution. The bands corresponding to iNOS were visualized by enhanced chemiluminescence.

2.8. ROS. The intracellular ROS level of B16-F10 was measured after 48 h with or without cFIR treatment. Intracellular ROS were detected using Carboxy-H2DCFDA. When oxidized by ROS, Carboxy-H2DCFDA fluoresces green. After incubating cells for 30 min with 1 μ M of Carboxy-H2DCFDA [11], the fluorescence was detected by confocal laser scanning microscopy (SP5, Leica) with excitation and emission wavelengths of 488 and 505–560 nm, respectively.

Intracellular ROS were also measured by flow cytometry. After 48 h with or without cFIR treatment, a dihydrorhodamine 123 working solution was added directly to the medium to reach 25 μ M and then incubated at 37°C for 25 min. Cells were then washed once, resuspended in PBS, and kept on ice for immediate detection by FACScan flow cytometry [12]. Levels of dihydrorhodamine 123 fluorescence represent the values from 10⁴ cells based on an arbitrary scale of fluorescence intensity.

2.9. Apoptosis. A cell that is undergoing apoptosis demonstrates nuclear condensation and DNA fragmentation, which can be detected by staining with Hoechst 33342 and fluorescence microscopy. B16-F10 cells were washed with PBS and stained with Hoechst 33342 (5 mg/mL) for 20 min at room temperature to detect apoptosis. Three independent experiments were used for each group, and at least 100 cells in seven random fields were counted [13].

2.10. Statistical Analysis. All data were measured in triplicate, with experiments repeated at least three times. Data are presented as the mean \pm standard deviation. Statistical significance between the control and cFIR groups was determined using the Wilcoxon test method. A value of $P < 0.05$ was considered statistically significant (*), and $P < 0.01$ was highly significant (**).

3. Results

3.1. Proliferation of Murine Melanoma Cells. Results of the cell viability assays are presented in Figure 2. For groups C (control), FP24 (cFIR irradiated for 24 h), and FP48 (cFIR irradiated for 48 h), cell viabilities were 100% \pm 2.9%, 101.9% \pm 2.5%, and 88.2% \pm 4.8%, respectively. Compared to group C, the rate of proliferation did not significantly change in group FP24, but significantly decreased (11.8% lower) in group FP48. RAW 264.7 macrophages were not affected by cFIR treatment. A significant difference in the inhibitory effect on B16-F10 cell viability was found at 48 h, and we examined HSP70, iNO, iNOS, ROS, and cell apoptosis at 48 h according to the cell viability results.

3.2. HSP70. After B16-F10 cells were treated with or without cFIR for a 48 h interval, levels of HSP70 synthesis were measured by western blotting. To normalize HSP70 contents, we evaluated the ratio of HSP70 to β -actin. Figure 3 shows that intracellular HSP70 production in the cFIR group was significantly less than that of the control group. The relative HSP70 amounts were 0.86 \pm 0.10 in group C and 0.37 \pm 0.07 in group FP48. This result reveals that cFIR significantly inhibited intracellular HSP70 expression by B16-F10 cells.

3.3. iNO. Levels of NO synthesis in group FP48 subjected to a 48 h interval with cFIR treatment and in group C without treatment were measured by the mean fluorescence intensity. Fluorescence intensities were 14 \pm 1.4 in group C and 11.8 \pm 0.5 in group FP48. Figure 4 shows that the iNO production in the cFIR group was significantly less than that of the control group. This result reveals that cFIR inhibited iNO synthesis by B16-F10 cells.

3.4. iNOS. Analysis of iNOS expression for B16-F10 cells subjected to a 48 h interval with or without cFIR treatment was performed by Western blotting. Figure 5 indicates that the normalized mean production of iNOS protein (iNOS/GAPDH) in group C and group FP48 are 2.85 \pm 1.19 and 1.33 \pm 0.75, respectively. This result may reflect the ability of cFIR to suppress iNOS expression by B16-F10 cells.

3.5. ROS. Figure 6 shows the staining of intracellular ROS by confocal laser scanning microscopy. Green spots in the images are stained ROS. Levels of intracellular ROS for the group subjected to a 48-h interval with cFIR treatment (Figure 6(a) right image) exhibited an increased amount compared to the control group (Figure 6(a) left image). The normalized ROS level (average intracellular/extracellular fluorescence intensity) indicated that there was a 6.0% increase in the cFIR group (1.07 \pm 0.04) compared to the control group (1.13 \pm 0.05) as shown in Figure 6(b).

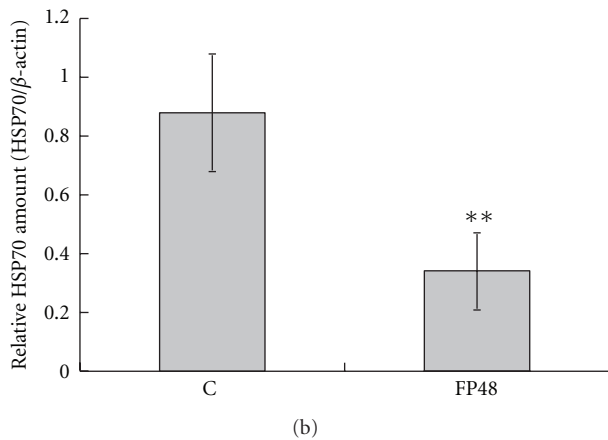
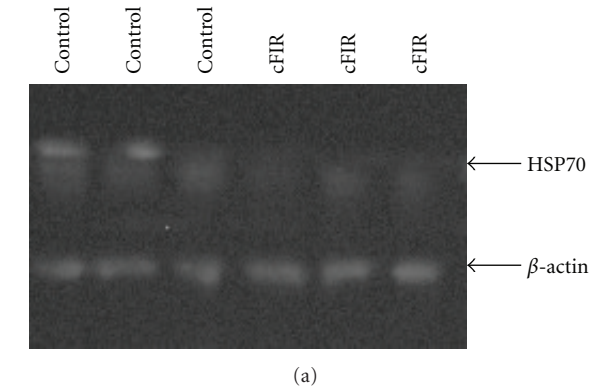


FIGURE 3: Comparison of intracellular HSP70 levels between the control (group C) and cFIR (group FP48) groups. (a) Western blotting gel. (b) The mean and standard deviation of the normalized HSP70 amount (Wilcoxon test).

Figure 7 shows another ROS result by flow cytometry. The mean fluorescence intensities of group C and group FP48 were 127.1 ± 14.1 and 142.7 ± 18.0 ($n = 12$), respectively. Therefore, the intracellular fluorescence intensity of group FP48 showed a 12.3% increase compared to group C. This result is consistent with the finding of confocal laser scanning microscopy (Figure 6).

3.6. Apoptosis. Compared to group C, inhibition of cell proliferation was observed in group FP48 by Hoechst 33342 staining (Figure 8). Compared to group C, cell proliferation was inhibited by $13.2\% \pm 0.8\%$ in group FP48. This result is consistent with the result of the MTT assay in Figure 2. However, only about $1.1\% \pm 0.1\%$ cells with apoptotic changes were observed in group FP48 (arrow in Figure 8(b)). The result indicates that inhibition of cell proliferation in group FP48 was perhaps not through inducing cell apoptosis but by interfering with the cell cycle such as cell growth arrest.

4. Discussion

In this study, we observed that the growth of B16-F10 cells was inhibited after irradiation with cFIR for 48 h (Figure 2) compared to the control group. A previous *in vitro* study [14] revealed that FIR with a heat source (hFIR) inhibited the

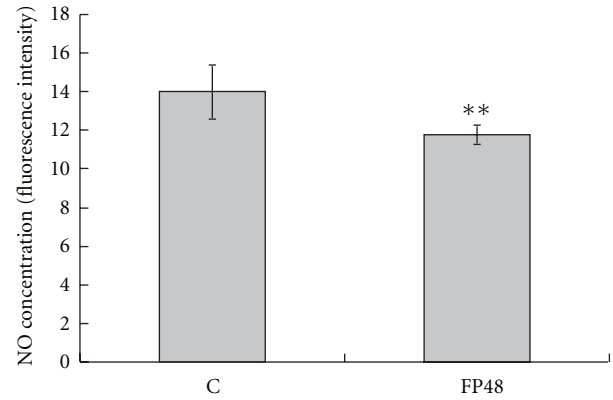


FIGURE 4: Comparison of intracellular NO between the control (group C) and cFIR (group FP48) groups. Expression values are the mean and standard deviation, and the statistical difference was detected by the Wilcoxon test.

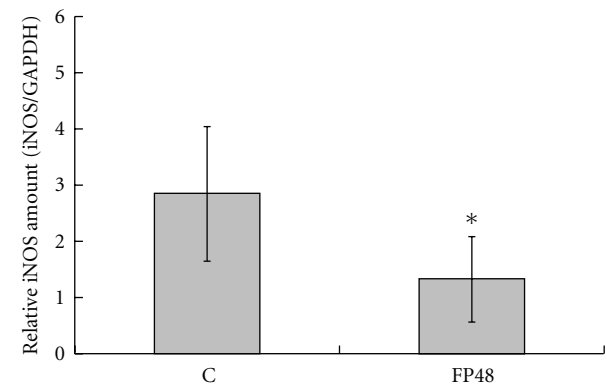


FIGURE 5: Comparison of inducible nitric oxide synthase between the control (group FP48) and cFIR (group FP48) groups. Expression values are the mean and standard deviation, and the difference between groups was tested using the Wilcoxon test.

growth of HeLa cells (a cervical cancer cell line). Similarly, Ishibashi et al.'s [6] demonstrated that hFIR suppressed the proliferation of several types of cancer cells, including HSC3 (tongue squamous cell carcinoma), Sa3 (gingival squamous cell carcinoma), and A549 (pulmonary adenocarcinoma) cell lines. Their results also demonstrated that hFIR has different effects on HSP70 overexpression in cancer cells with different basal levels of HSP70. Based on Ishibashi et al. [6] and our studies, FIR may have potential benefits in the medical treatment of melanomas. However, our study with cFIR differed from that of Ishibashi et al. with hFIR producing a 40°C thermal effect. As is known, HSPs accumulate in cells exposed to a heat source and a variety of other stressful stimuli. In fact, hFIR experiments produce a thermal effect which might overlap with the results of the somathermal cFIR influence on cells.

Gene expression levels of HSPs can determine the fate of cells in response to a death stimulus, and apoptosis-inhibitory HSPs, particularly HSP70, may participate in carcinogenesis [15]. A previous study demonstrated that pancreatic cancer cells expressed significantly higher HSP70

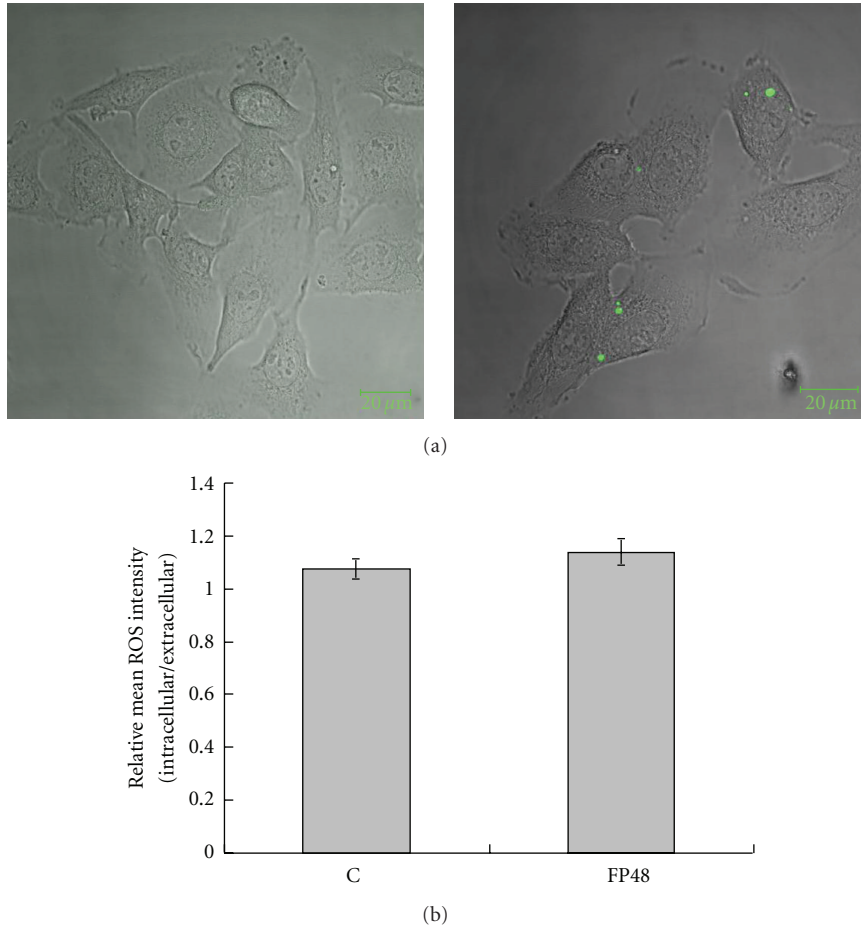


FIGURE 6: Intracellular ROS by confocal laser scanning microscopy. (a) Stained images of ROS in the control group (left) and cFIR group (right). Scale bars = 20 μm. (b) Comparison of normalized mean ROS fluorescence intensity in B16-F10 cells between the control (group C) and cFIR (group FP48) groups.

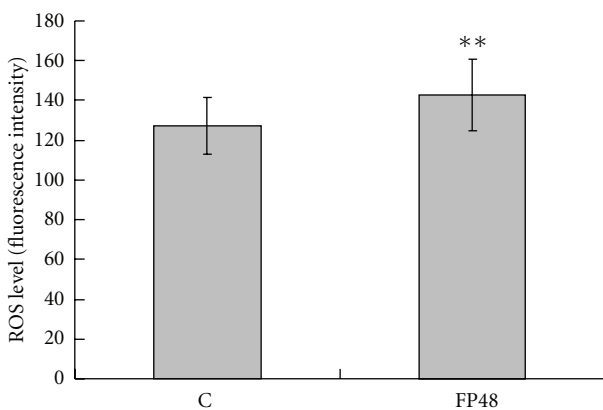


FIGURE 7: Intracellular ROS by flow cytometry. Expression values of the control (group C) and cFIR (group FP48) groups are the mean and standard deviation, and the statistical difference was detected by the Wilcoxon test.

levels compared to nonmalignant ductal cells, which suggests that HSP70 plays a role in tumor cell resistance to apoptosis [16]. They showed increased HSP70 expression in cancer

tissues versus normal tissues from the same pancreatic cancer patient. These findings agree with several reports in the literature showing increased HSP70 expression in a variety of malignant tumors, such as colorectal, breast, and gastric cancers. The importance of these findings strengthens the hypothesis that high levels of HSP70 expression are correlated with increased drug resistance in cancer cell lines. They concluded that the major role of HSP70 was in boosting resistance of pancreatic cancer cells to apoptosis. Gurbuxani et al. [17] showed increased gene expression of HSP70 in tumor cells and proposed that it enhances their immunogenicity. However, HSP70 was also demonstrated to prevent tumor apoptosis. They proved that the reduced level of HSP70 expression in colon cancer cells resulted in a specific immune response by promoting cell death *in vivo*. HSP 70 is overexpressed in malignant melanomas [18] and underexpressed in renal cell cancer [19]. Overexpression of HSP70 in various tumors is associated with enhanced tumorigenicity and resistance to therapy. Conversely, downregulation of Hsp70 in tumor cells was found to enhance tumor regression in certain animal models [20].

HSP was found to be overexpressed by B16-F10 melanoma cells. The HSP70 protein content was shown to

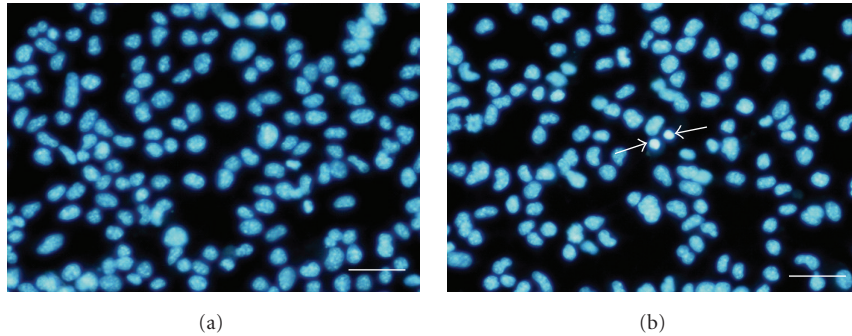


FIGURE 8: Hoechst 33342 staining to detect apoptotic changes. (a) Control group and (b) cFIR group. Scale bars = 50 μm . Arrows indicate very small amounts of apoptotic changes (DNA condensation) in B16-F10 cells treated by cFIR for 48 h.

considerably vary in human melanoma cells from different cell lines, and HSP70 levels in melanoma cells evidently contribute to their resistance to anticancer drugs [21]. HSP70 expression is elevated in many cancers and contributes to tumor cell survival and resistance to therapy. Leu et al. [22] found that tumor cells cultured with an HSP70 inhibitor showed suppressed tumor development, and the survival of mice was enhanced. Stellas et al. [23] showed that using a monoclonal antibody against HSP90 was capable of inhibiting cell invasion and metastasis of B16-F10 melanomas. Galluzzi et al. [24] also demonstrated that a chemical inhibitor of HSP70 exerted prominent tumor-selective cytotoxic effects, thereby lending further support to the future application of HSP70 as a promising target for anticancer therapy. In addition, a previous study conducted by Nylandsted et al. [25] found that depletion of HSP70 may inhibit cancer. The expression of HSP70 is correlated with increased cell proliferation, poor differentiation, lymph node metastases, and poor therapeutic outcomes in human breast cancer [26]. A recent study validated that using an HSP70 inhibitor was capable of inhibiting B16-F10 cell growth [27].

In this study, we also found that NO levels significantly decreased after irradiation with cFIR powder, indicating that the inhibitory effect on the murine melanoma cell line may be associated with lowered levels of NO. Intracellular NO is a highly reactive molecule implicated in numerous physiologic and pathologic processes, which play important roles in nonspecific antitumor immune responses [8, 28, 29]. However, in some circumstances, NO may also lead to tumor expansion and metastasis [28, 30, 31].

In this study, we further found that iNOS production in cFIR group was significantly lower than control group. This finding may reflect that the reduction of iNO is a result of the inhibition of iNOS by cFIR. For murine melanoma cells, a connection between elevated levels of NO after iNOS induction and consequent cancer cell inhibition was previously described [32]. In fact, iNOS was induced by cytokines and LPS in normal melanocytes but not in melanoma cells [33]. The expression of iNOS found in melanoma cells may result in the continuous formation of NO, which may subsequently activate or inhibit physiological processes different from apoptosis but important for tumor progression. The elevation of iNOS and the consequent higher NO levels

were also associated with an increased number of lymphatic vessels, resulting in lymphangiogenesis in melanomas [34]. It was also demonstrated that the loss of iNOS inducibility in melanoma cells showed a well-demarcated difference from normal melanocytes, and this regulation defect was the result of melanocytic transformation and malignancy [31]. Unlimited elevation of NO concentrations in melanomas is expected to promote metastases by maintaining the vasodilator tone of blood vessels in and around the melanoma [35]. It is well recognized that NO is involved in melanoma progression, since the proliferative and metastatic capacities were measured and showed that NO-treated melanoma cells exhibited higher levels of aggressiveness [36]. Therefore, our results showing simultaneous melanoma cell inhibition and a decrease in NO by suppression of iNOS expression can logically be accepted.

ROS are constantly generated and eliminated in biological systems and play important roles in a variety of normal biochemical functions and abnormal pathological processes. Growing evidence suggests that cancer cells exhibit increased intrinsic ROS stress accompanied by increased metabolic activity and mitochondrial malfunction [37]. Previous studies demonstrated that certain agents that generate ROS help preferentially kill cancer cells or inhibit their growth [38–41]. Cancer cells that exhibit increased intrinsic oxidative stress with high levels of cellular ROS and a low antioxidant capacity are more susceptible to chemotherapy. Therefore, there is a therapeutic strategy to treat cancer cells by further increasing ROS using pharmacological agents that directly increase ROS production, inhibit cancer cell antioxidant defenses, or their combination [37, 38].

Based on our current results, we propose that cFIR treatment may induce intracellular ROS production which results in cell growth arrest but not significant apoptosis [41]. On the other hand, cFIR treatment also reduced Hsp70 expression and NO production and resulted in further cell growth inhibition. However, the detailed mechanism is not clear yet, and further investigations are needed to elucidate this.

5. Conclusions

Unlike traditional FIR with a heat source, this study is the first to demonstrate that somathermal cFIR without an

additional thermal effect affected murine melanoma cells and was capable of suppressing the proliferation of B16-F10 cells and inhibiting intracellular NO and HSP70 production. Treatment with cFIR induced intracellular ROS production but did not significantly affect cell apoptosis, leading us to speculate that interference with the cell cycle, such as cell growth arrest, occurred. We deduced that the melanoma inhibitory effect may be a consequence of or share a common pathway with the decreased intracellular HSP70 and NO. Further investigations into the basic biomolecular and physiological mechanisms occurring in melanoma cells following cFIR treatment will help advance future therapeutic applications of cFIR.

Acknowledgment

This work was supported by a Grant from the National Science Council of Taiwan (NSC 99-2622-E-241-003-CC3).

References

- [1] S. Inoue and M. Kabaya, "Biological activities caused by far-infrared radiation," *International Journal of Biometeorology*, vol. 33, no. 3, pp. 145–150, 1989.
- [2] S. C. Lee, S. Y. Kim, S. M. Jeong, and J. H. Park, "Effect of far-infrared irradiation on catechins and nitrite scavenging activity of green tea," *Journal of Agricultural and Food Chemistry*, vol. 54, no. 2, pp. 399–403, 2006.
- [3] S. Y. Yu, J. H. Chiu, S. D. Yang, Y. C. Hsu, W. Y. Lui, and C. W. Wu, "Biological effect of far-infrared therapy on increasing skin microcirculation in rats," *Photodermatology, Photoimmunology & Photomedicine*, vol. 22, no. 2, pp. 78–86, 2006.
- [4] C. C. Lin, C. F. Chang, M. Y. Lai, T. W. Chen, P. C. Lee, and W. C. Yang, "Far-infrared therapy: a novel treatment to improve access blood flow and unassisted patency of arteriovenous fistula in hemodialysis patients," *Journal of the American Society of Nephrology*, vol. 18, no. 3, pp. 985–992, 2007.
- [5] J. F. Tsai, S. Hsiao, and S. Y. Wang, "Infrared irradiation has potential antidepressant effect," *Progress in Neuro-Psychopharmacology and Biological Psychiatry*, vol. 31, no. 7, pp. 1397–1400, 2007.
- [6] J. Ishibashi, K. Yamashita, T. Ishikawa et al., "The effects inhibiting the proliferation of cancer cells by far-infrared radiation (FIR) are controlled by the basal expression level of heat shock protein (HSP) 70A," *Medical Oncology*, vol. 25, no. 2, pp. 229–237, 2008.
- [7] T. K. Leung, C. M. Lee, M. Y. Lin et al., "Far infrared ray irradiation induces intracellular generation of nitric oxide in breast cancer cells," *Journal of Medical and Biological Engineering*, vol. 29, no. 1, pp. 15–18, 2009.
- [8] T. K. Leung, Y. S. Lin, Y. C. Chen et al., "Immunomodulatory effects of far-infrared ray irradiation via increasing calmodulin and nitric oxide production in raw 264.7 macrophages," *Bio-medical Engineering - Applications, Basis and Communications*, vol. 21, no. 5, pp. 317–323, 2009.
- [9] T. K. Leung, Y. S. Lin, C. M. Lee et al., "Direct and indirect effects of ceramic far infrared radiation on the hydrogen peroxide-scavenging capacity and on murine macrophages under oxidative stress," *Journal of Medical and Biological Engineering*. In press.
- [10] A. H. Cory, T. C. Owen, J. A. Barltrop, and J. G. Cory, "Use of an aqueous soluble tetrazolium/formazan assay for cell growth assays in culture," *Cancer Communications*, vol. 3, no. 7, pp. 207–212, 1991.
- [11] M. Sundaresan, Z. X. Yu, V. J. Ferrans, K. Irani, and T. Finkel, "Requirement for generation of H₂O₂ for platelet-derived growth factor signal transduction," *Science*, vol. 270, no. 5234, pp. 296–299, 1995.
- [12] J. A. Smith and M. J. Weidemann, "Further characterization of the neutrophil oxidative burst by flow cytometry," *Journal of Immunological Methods*, vol. 162, no. 2, pp. 261–268, 1993.
- [13] S. Allen, J. Sotos, M. J. Sylte, and C. J. Czuprynski, "Use of hoechst 33342 staining to detect apoptotic changes in bovine mononuclear phagocytes infected with *Mycobacterium avium* subsp. paratuberculosis," *Clinical and Diagnostic Laboratory Immunology*, vol. 8, no. 2, pp. 460–464, 2001.
- [14] F. Teraoka, Y. Hamada, and J. Takahashi, "Bamboo charcoal inhibits growth of HeLa cells in vitro," *Dental Materials Journal*, vol. 23, no. 4, pp. 633–637, 2004.
- [15] C. Didelot, E. Schmitt, M. Brunet, L. Maingret, A. Parcellier, and C. Garrido, "Heat shock proteins: endogenous modulators of apoptotic cell death," *Handbook of Experimental Pharmacology*, vol. 172, pp. 171–198, 2006.
- [16] A. Aghdassi, P. Phillips, V. Dudeja et al., "Heat shock protein 70 increases tumorigenicity and inhibits apoptosis in pancreatic adenocarcinoma," *Cancer Research*, vol. 67, no. 2, pp. 616–625, 2007.
- [17] S. Gurbuxani, J. M. Bruey, A. Fromentin et al., "Selective depletion of inducible HSP70 enhances immunogenicity of rat colon cancer cells," *Oncogene*, vol. 20, no. 51, pp. 7478–7485, 2001.
- [18] N. Ricaniadis, A. Katakaki, N. Agnantis, G. Androulakis, and C. P. Karakousis, "Long-term prognostic significance of HSP-70, c-myc and HLA-DR expression in patients with malignant melanoma," *European Journal of Surgical Oncology*, vol. 27, no. 1, pp. 88–93, 2001.
- [19] U. Ramp, C. Mahotka, S. Heikaus et al., "Expression of heat shock protein 70 in renal cell carcinoma and its relation to tumor progression and prognosis," *Histology and Histopathology*, vol. 22, no. 10, pp. 1099–1107, 2007.
- [20] R. Dressel, C. Grzeszik, M. Kreiss et al., "Differential effect of acute and permanent heat shock protein 70 overexpression in tumor cells on lysability by cytotoxic T lymphocytes," *Cancer Research*, vol. 63, no. 23, pp. 8212–8220, 2003.
- [21] N. V. Gukasova, I. G. Kondrasheva, E. Y. Moskaleva et al., "Hsp70 protein content in human melanoma cells as a factor of resistance to antitumor drugs," *Molecular Medicine*, vol. 1, pp. 15–21, 2009.
- [22] J. I. J. Leu, J. Pimkina, A. Frank, M. E. Murphy, and D. L. George, "A small molecule inhibitor of inducible heat shock protein 70," *Molecular Cell*, vol. 36, no. 1, pp. 15–27, 2009.
- [23] D. Stellas, A. Karameris, and E. Patsavoudi, "Monoclonal antibody 4C5 immunostains human melanomas and inhibits melanoma cell invasion and metastasis," *Clinical Cancer Research*, vol. 13, no. 6, pp. 1831–1838, 2007.
- [24] L. Galluzzi, F. Giordanetto, and G. Kroemer, "Targeting HSP70 for cancer therapy," *Molecular Cell*, vol. 36, no. 2, pp. 176–177, 2009.
- [25] J. Nylandsted, W. Wick, U. A. Hirt et al., "Eradication of glioblastoma, and breast and colon carcinoma xenografts by Hsp70 depletion," *Cancer Research*, vol. 62, no. 24, pp. 7139–7142, 2002.
- [26] J. Nylandsted, M. Rohde, K. Brand, L. Bastholm, F. Elling, and M. Jäättelä, "Selective depletion of heat shock protein 70 (Hsp70) activates a tumor-specific death program that is independent of caspases and bypasses Bcl-2," *Proceedings of the*

- National Academy of Sciences of the United States of America*, vol. 97, no. 14, pp. 7871–7876, 2000.
- [27] A. Yerlikaya, E. Okur, S. Şeker, and N. Erin, “Combined effects of the proteasome inhibitor bortezomib and Hsp70 inhibitors on the B16F10 melanoma cell line,” *Molecular Medicine Reports*, vol. 3, no. 2, pp. 333–339, 2010.
- [28] J. M. Tarr, P. Eggleton, and P. G. Winyard, “Nitric oxide and the regulation of apoptosis in tumour cells,” *Current Pharmaceutical Design*, vol. 12, no. 34, pp. 4445–4468, 2006.
- [29] K. Ivanova, B. Lambers, R. Van Den Wijngaard et al., “Immortalization of human melanocytes does not alter the de novo properties of nitric oxide to induce cell detachment from extracellular matrix components via cGMP,” *In Vitro Cellular and Developmental Biology—Animal*, vol. 44, no. 8–9, pp. 385–395, 2008.
- [30] B. Bonavida, S. Khineche, S. Huerta-Yepey, and H. Garbán, “Therapeutic potential of nitric oxide in cancer,” *Drug Resistance Updates*, vol. 9, no. 3, pp. 157–173, 2006.
- [31] R. Mitra, S. Singh, and A. Khar, “Antitumour immune responses,” *Expert Reviews in Molecular Medicine*, vol. 5, no. 3, pp. 1–19, 2003.
- [32] L. F. Fecker, J. Eberle, C. E. Orfanos, and C. C. Geilen, “Inducible nitric oxide synthase is expressed in normal human melanocytes but not in melanoma cells in response to tumor necrosis factor- α , interferon- γ , and lipopolysaccharide,” *Journal of Investigative Dermatology*, vol. 118, no. 6, pp. 1019–1025, 2002.
- [33] L. C. Jadeski and P. K. Lala, “Nitric oxide synthase inhibition by N(G)-nitro-L-arginine methyl ester inhibits tumor-induced angiogenesis in mammary tumors,” *American Journal of Pathology*, vol. 155, no. 4, pp. 1381–1390, 1999.
- [34] D. Massi, M. C. De Nisi, A. Franchi et al., “Inducible nitric oxide synthase expression in melanoma: Implications in lymphangiogenesis,” *Modern Pathology*, vol. 22, no. 1, pp. 21–30, 2009.
- [35] M. Joshi, J. Strandhoy, and W. L. White, “Nitric oxide synthase activity is up-regulated in melanoma cell lines: a potential mechanism for metastases formation,” *Melanoma Research*, vol. 6, no. 2, pp. 121–126, 1996.
- [36] Z. Yang, S. Yang, B. J. Misner, R. Chiu, F. Liu, and F. L. Meyskens, “Nitric oxide initiates progression of human melanoma via a feedback loop mediated by apurinic/apyrimidinic endonuclease-1/redox factor-1, which is inhibited by resveratrol,” *Molecular Cancer Therapeutics*, vol. 7, no. 12, pp. 3751–3760, 2008.
- [37] H. Pelicano, D. Carney, and P. Huang, “ROS stress in cancer cells and therapeutic implications,” *Drug Resistance Updates*, vol. 7, no. 2, pp. 97–110, 2004.
- [38] E. O. Hileman, J. Liu, M. Albitar, M. J. Keating, and P. Huang, “Intrinsic oxidative stress in cancer cells: a biochemical basis for therapeutic selectivity,” *Cancer Chemotherapy and Pharmacology*, vol. 53, no. 3, pp. 209–219, 2004.
- [39] H. Kudara, E. Tahara, H. J. Kim, D. Lotan, J. Myers, and R. Lotan, “Involvement of Rac in fenretinide-induced apoptosis,” *Cancer Research*, vol. 68, no. 11, pp. 4416–4423, 2008.
- [40] S. Macip, M. Igarashi, L. Fang et al., “Inhibition of p21-mediated ROS accumulation can rescue p21-induced senescence,” *EMBO Journal*, vol. 21, no. 9, pp. 2180–2188, 2002.
- [41] Y. F. Chang, Y. C. Hsu, H. F. Hung et al., “Quercetin induces oxidative stress and potentiates the apoptotic action of 2-methoxyestradiol in human hepatoma cells,” *Nutrition and Cancer*, vol. 61, no. 5, pp. 735–745, 2009.

Research Article

Energy Conversion in Protocells with Natural Nanoconductors

Jian Xu,¹ T. Kyle Vanderlick,¹ and David A. LaVan²

¹ School of Engineering and Applied Science, Yale University, New Haven, CT 06511, USA

² Material Measurement Laboratory, National Institute of Standards and Technology, Gaithersburg, MD 20899, USA

Correspondence should be addressed to David A. LaVan, david.lavan@nist.gov

Received 22 June 2011; Accepted 17 July 2011

Academic Editor: Tebello Nyokong

Copyright © 2012 Jian Xu et al. This is an open access article distributed under the Creative Commons Attribution License, which permits unrestricted use, distribution, and reproduction in any medium, provided the original work is properly cited.

While much nanotechnology leverages solid-state devices, here we present the analysis of designs for hybrid organic-inorganic biomimetic devices, “protocells,” based on assemblies of natural ion channels and ion pumps, “nanoconductors,” incorporated into synthetic supported lipid bilayer membranes. These protocells mimic the energy conversion scheme of natural cells and are able to directly output electricity. The electrogenic mechanisms have been analyzed and designs were optimized using numerical models. The parameters that affect the energy conversion are quantified, and limits for device performance have been found using numerical optimization. The electrogenic performance is compared to conventional and emerging technologies and plotted on Ragone charts to allow direct comparisons. The protocell technologies summarized here may be of use for energy conversion where large-scale ion concentration gradients are available (such as the intersection of fresh and salt water sources) or small-scale devices where low power density would be acceptable.

1. Introduction

Protocells are simplified, synthetic versions of natural cells that can be engineered for specific functions. The protocell designs described here consist of well-characterized molecular components and can be designed to maximize energy conversion [1, 2]. Our protocell designs are inspired by natural cell structures, but are not a simple duplicate of natural cells. These protocells have one or more lipid bilayers [3–5], membranes of back-to-back monolayers of amphiphilic lipid molecules formed by hydrophobic interactions, with appropriate nanoconductors [1, 6–10] to achieve the performance goals. The lipid bilayers would be stabilized, such as on a mesoporous silica [11] or nanofiber support [12]. The nanoconductors incorporated into the membranes can be either natural or engineered [13] membrane proteins, including ion channels and ion pumps [1, 6–10, 14]; they are responsible for the regulation of ionic flux through the lipid bilayer. Channels let ions passively travel along the electrochemical gradient and may be gated to open and close in response to chemical, mechanical, or electrical signals, while pumps actively move ions against the electrochemical gradient but require energy input, for example, from ATP hydrolysis [15, 16]. Ion transport is widely studied in

the context of biology and neuroscience of natural cells [14, 16, 17]. The protocells described here exploit and extend the electrical energy conversion mechanisms found in natural cells by assembling optimized combinations of nanoconductors to maximize energy output.

Emerging energy conversion devices rely on a myriad of technologies, including solid-state materials based on thermoelectric [18–20], piezoelectric [21, 22], and photovoltaic [23, 24] effects. Thermoelectric devices convert a thermal gradient into electric voltage; these devices require the unusual combination of good electrical conductivity and poor thermal conductivity, for example, bismuth telluride (Bi_2Te_3) or its alloys with selenium [18–20, 25, 26]; the energy conversion efficiency of thermoelectric devices is still low (<10%) [18, 19]. Piezoelectric devices convert mechanical strain into charge based on the strain-induced charge separation effect of piezoelectric materials, such as quartz crystals [21, 22] or ZnO nanowires [27]. However, the energy output of piezoelectric devices is low ($\approx 10^4 \text{ J}\cdot\text{m}^{-3}$) [28, 29]; these devices can only satisfy applications with very low power consumption (<mW) [30, 31]. And of course, photovoltaic devices convert light energy into electricity. Single junction thin film photovoltaic devices have energy conversion efficiency up to $\approx 25\%$ [32–34]. Multijunction

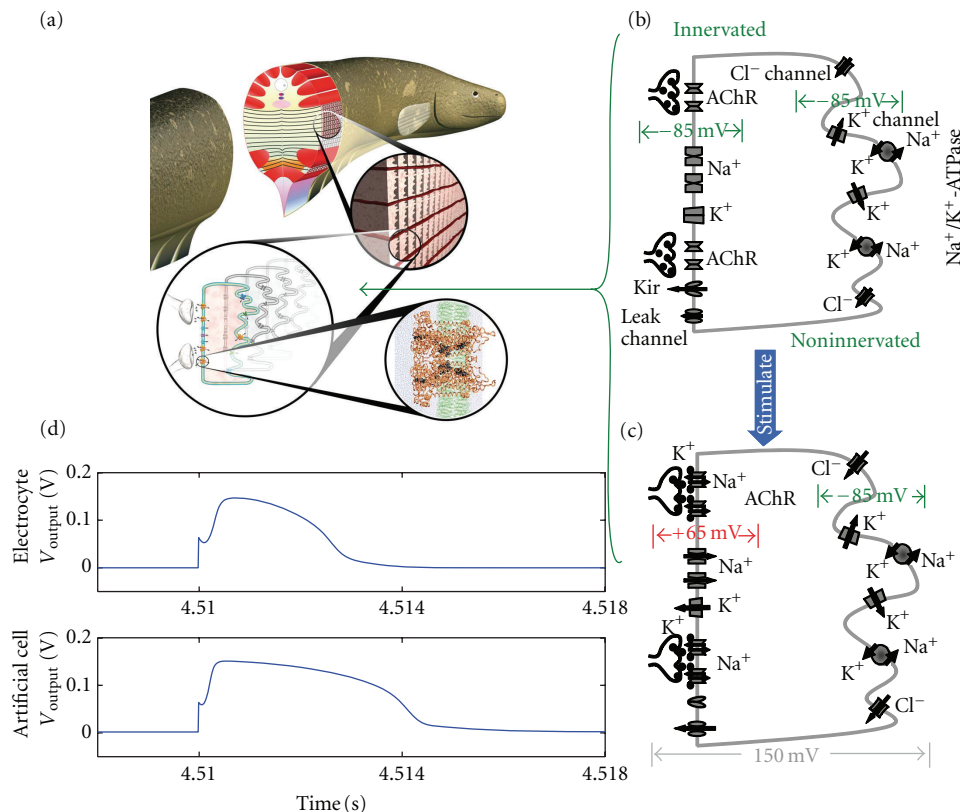


FIGURE 1: The electrogenic mechanism and performance of a protocell with AC output. (a) The anatomy of the electric eel [1]. (b) and (c) The electrocyte in the resting and the stimulated stage [1]. (d) The calculated voltage outputs of the electrocyte and the optimally configured artificial protocell.

inorganic photovoltaic cells convert broader ranges of the available spectrum into electricity; the reported efficiency of multijunction cells has reached $\approx 42\%$ [23, 24].

In contrast to these solid-state materials, individual biological components have significantly higher energy conversion efficiency. For instance, Na^+/K^+ -ATPase, the ubiquitous ion pump, which maintains transmembrane Na^+ and K^+ gradients, actively pumps Na^+ and K^+ against their ion gradients with an efficiency of 75% to 80% using energy from ATP hydrolysis [35, 36]. Another transmembrane protein, F_1 -ATPase, is reported to convert the free energy from ATP hydrolysis into the rotation of F_1 motor with the efficiency close to 100% [37–40]. However, neither of these numbers takes into account losses in the rest of the ATP energy cycle.

Current biological energy conversion schemes usually rely on the formation of an intermediate product (oil, sugar, ethanol, etc.) that can be refined and burned to produce electricity [41, 42] with substantial losses in this step; however, cells also convert chemical energy directly into action potentials, and we have been interested in exploring this “direct to electricity” approach that eliminates the combustion/fuel cell losses. For instance, *Electrophorus electricus* generates electricity to sense in murky water, stun prey, and ward off predators [43, 44]. A mature electric eel can generate substantial electric voltage (open circuit) of 400 V to 600 V [8, 44, 45], with current peaks (short circuit) of

1 A [45, 46]. The electricity is produced by the collective behavior of its electrogenic cells, the “electrocytes”, under the synchronization of its electromotor neurons [8, 45, 47] (Figure 1(a)). The electrocyte generates electricity in the form of action potentials; each electrocyte may produce ≈ 150 mV transcellular potential with typical durations on the order of 3 ms [8, 45]. Many other natural cells produce action potentials with varying amplitudes and durations. For instance, a squid giant axon generates ≈ 100 mV for ≈ 1 ms [17, 48–52]. The electricity is converted from the transmembrane ion gradient through these cell membranes by membrane-protein-regulated ion transport [8, 17, 45].

Artificial protocells designed to mimic and maximize the energy conversion schemes seen in natural electrogenic cells, are an intriguing approach to energy conversion that builds on recent advances in synthetic biology and nanotechnology.

2. Electrogenic Mechanism of Protocells

In the electrocyte, the transmembrane proteins necessary for action potential formation are asymmetrically distributed across two primary membranes (Figure 1(b)) separated by insulating septa [8, 43–45]. The noninnervated membrane exhibits high densities of Na^+/K^+ -ATPase pumps, K^+ channels, and Cl^- channels, which maintain a resting potential of ≈ -85 mV [8, 45, 53]. The innervated membrane

contains high densities of acetylcholine receptors (AChRs) and voltage-gated Na^+ channels, which are responsible for the activation of the action potential (AP); there are also inward rectifier K^+ channels (Kirs) [8], voltage-gated K^+ channels (Kvs) [9], and leak channels [8] on the innervated membrane.

Upon binding of a chemical agonist, acetylcholine (ACh), the ACh receptors (AChR) become permeable to Na^+ and K^+ cations. The opening of AChRs depolarizes the innervated membrane, raising the open probability of voltage-gated Na^+ ion channels (Figure 1(c)) [6, 8, 44]. With positively charged ions (Na^+) flowing into the cell, the innervated membrane potential further increases, which enhances the opening of additional voltage-gated Na^+ channels. This cascade, where ACh receptors open large number of voltage-gated Na^+ channels, results in the formation of an AP on the innervated membrane. The inward rectifier K^+ channels are closed during this stage, which speeds the increase of the membrane potential. At the peak, the innervated membrane potential is +65 mV [8, 53]. Because of the existence of abundant voltage-gated Na^+ ion channels on the innervated membrane, the electrocyte can also be stimulated electrically, that is, injecting current to depolarize the innervated membrane [54, 55].

There are no AChRs or voltage-gated Na^+ ion channels on the noninnervated membrane of the electrocyte (Figure 1(c)) [8, 45, 53]. Therefore, this membrane is unable to respond to either chemical or electrical stimulus. The noninnervated membrane potential remains ≈ -85 mV due to ATPase, K^+ channel, and Cl^- channel activities [8, 45, 53]. At the peak of an action potential, the innervated membrane reaches +65 mV transmembrane potential resulting in a total ≈ 150 mV voltage output across each electrocyte (Figure 1(c)) [8, 45, 53]. This transcellular potential is summed with serial connection of multiple electrocytes. For an electric eel to generate 600 V there must be at least 4000 layers of electrocytes connected in series [53]. In every layer, multiple electrocytes are connected in parallel to increase the current (Figure 1(a)). The insulating septa, composed of dense connective tissues [44, 56], separate the innervated membrane and the noninnervated membrane and prevent the electric charge from being short-circuited within the fish (Figure 1(a)).

After the peak of action potential, the innervated membrane is repolarized with the inactivation of Na^+ channels [6] and the opening of inward rectifier channels and voltage-gated K^+ channels [8, 9]. The leak ion flux further expedites the restoration of membrane potential to the resting state [57].

During the action potential, substantial ion flux occurs through the open ion channels, which results in a net electric current (electric charge flux) from the innervated membrane to the noninnervated membrane. The necessary ion concentration gradient is sustained by the slow and steady action of ion pumps, Na^+/K^+ -ATPase, relying on energy from ATP hydrolysis [35, 36, 58].

A protocell, with the same ion channels/pumps configuration as the natural electrocyte, may imitate the electrogenic mechanism of the natural electric eel. Such a protocell pro-

duces the electricity in the form of an action potential, that is, an alternating current (AC) output. The ion gradient in this protocell is created, and can be recharged, by ATP fueled ion pumps, for example, Na^+/K^+ -ATPase [35, 36, 58]. If other molecular components were added, such as bacteriorhodopsin and F_0F_1 -ATP synthase [59–62], this protocell could be recharged by light energy.

A rechargeable protocell with AC output requires concerted system-level interactions of multiple types of ion channels and at least one type of ion pump [1]. A simplified version, reduced to just one type of ion channel (or channel analogue) would lack the ability to recharge, but would be easier to fabricate and could convert an existing ion concentration gradient into DC current, as shown in Figure 2(a).

One scheme for a protocell with DC output consists of two water droplets with different initial salt concentrations, suspended in an immiscible carrier, such as a mixture of oil and lipid. Because of the hydrophobic interactions, the surface of the water droplet is covered by a monolayer of lipid; when the two water droplets are brought into contact, a lipid bilayer forms at the interface of the two water droplets (as shown in Figure 2(a)) [64–68]. The presence of the bilayer prevents the merging of the two water droplets (Figure 2(b)). If an ion selective channel (or synthetic analogue) is inserted at the interface, ions will flow from the high-concentration droplet to the low-concentration one.

Natural ion channels are not very stable, synthetic channel analogues, such as the *S. aureus* α -hemolysin (α -HL), are useful platforms to dial-in desired channel performance. The wildtype α -HL is normally weakly anion selective [69, 70]; it can also be made cation selective by protein engineering with or without further chemical modification [63, 71]; for instance, 2-sulfonatoethyl methanethiosulfonate- (MTSES-) treated G133C mutant has been reported with cation selectivity of 170 ($g_{\text{K}}/g_{\text{Cl}}$) [63].

When cation selective channels are inserted into the bilayer at the interface of two droplets (Figure 2(a)), there will be unbalanced ion transport, which causes charge separation between the droplets. This charge separation results in a potential difference. In addition, due to the different chemical activities of electrodes submerged in the droplets with different concentrations of salts [72, 73], the electrode reactions also contribute to the potential difference. The total voltage output of such a system is the combination of contributions from selective ion transport and the electrode reactions in the different solutions. The output can power an external circuit, modeled as a resistor (R), as shown in Figure 2(a).

3. Electrogenic Performance of Protocells

Before undertaking the design of an artificial electrocyte, we developed a quantitative model (as described in [1]) to describe the electrogenic mechanism in the natural electrocyte of *Electrophorus electricus* and to evaluate the influence of molecular parameters on the electrogenic performance of the cell; the numerical model served to guide the design of the protocell to optimize the electrogenic performance.

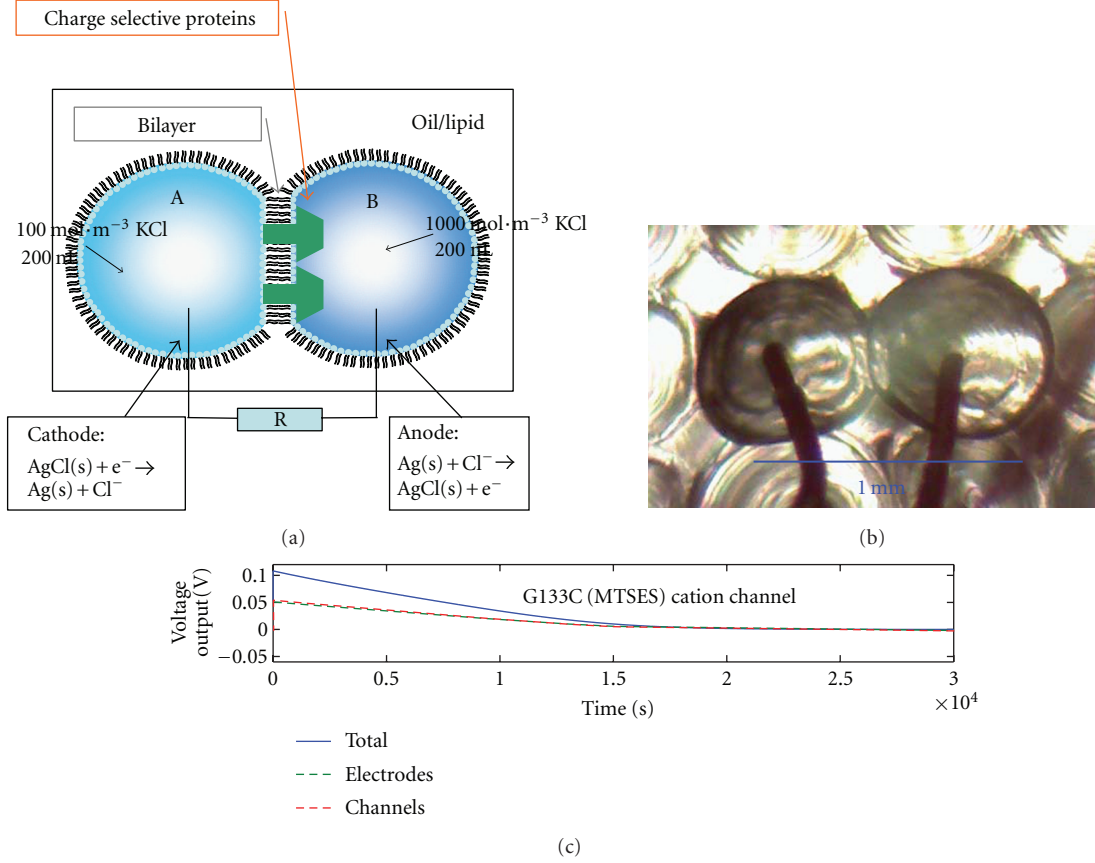


FIGURE 2: The electrogenic mechanism and performance of a protocell with DC output. (a) The schematic of this protocell (not drawn to scale) [2]; (b) the microscopic image of the structure of this protocell (scale bar: 1 mm); (c) the calculated voltage output of this protocell using a cation-selective channel (MTSES-treated G133C α -HL mutant), based on published channel parameters [63]. The total voltage output (E_t) is shown with the contribution from ion transport through the channels (E_r) and contributions from the electrodes (E_c).

To summarize briefly, the ionic current through innervated membrane of the electrocyte (Figure 1(b)) is described by the Hodgkin-Huxley model [17], with currents through the AChR and Kir channels;

$$I = C_M \frac{dV}{dt} + \bar{g}_K n^4 (V - V_K) + \bar{g}_{Na} m^3 h (V - V_{Na}) + \bar{g}_l (V - V_l) + I_{Kir} + I_{AChR}, \quad (1)$$

where I is the current through the innervated membrane, C_M is membrane capacitance, and V is the membrane potential. \bar{g}_K is the maximum conductance of voltage-gated K^+ channel, n determines the open probability of K^+ channel, V_K is the equilibrium potential of K^+ ions; \bar{g}_{Na} and V_{Na} are those of Na^+ channels, m controls the activation of Na^+ channels, and h determines the inactivation of Na^+ channels. \bar{g}_l is the conductance of leak channel and V_l is the potential at which the leak current is zero. I_{Kir} is the current through the inward rectifier channels. I_{AChR} is the current through AChR.

There are K^+ and Cl^- ion channels as well as Na^+/K^+ -ATPase on the noninnervated membrane. The ionic current through the ion channel in the noninnervated membrane (Figure 1(b)) is described by the Goldman-Hodgkin-Katz current equation [6], which depicts the current through

a channel as a function of membrane potential and the ion gradient. The active transport of ions by Na^+/K^+ -ATPase on the noninnervated membrane was modelled with Michaelis-Menten kinetics at a ratio of three Na^+ ions per two K^+ ions [74, 75].

The missing physiological parameters were found numerically by matching the model current output to the nuances of the measured action potential curve on the natural electrocyte with nonlinear least squares [76, 77].

The voltage output of the natural electrocyte is shown in the upper trace of Figure 1(d). The design of the protocell was numerically optimized to maximize the electrogenic performance. The design of the protocell started as a list of natural nanoconductors (i.e., ion channels/pumps), basic biophysical parameters (ion permeabilities, two insulating membranes, etc.); the objective of the numerical optimization was to maximize the electrogenic performance (e.g., single pulse energy output, power output density, or energy conversion efficiency) of the protocell design.

The electrical energy output of an artificial cell is defined as

$$W = \int UI dt, \quad (2)$$

where W is the electrical power output and U and I are the voltage and current applied, over time, t . The single pulse energy output is defined as the energy output during one firing of the action potential. The power output density is defined as the energy output of a single layer of cells in a unit of time and with a unit area of cell membrane.

The energy conversion efficiency Φ of the AC protocell is defined as

$$\Phi = \frac{W_{\text{out}}}{E_{\text{sti}} + E_{\text{ATPase}}/\Phi_{\text{ATP}}}, \quad (3)$$

where W_{out} is the work done across the external circuit, E_{sti} is the energy input from the electrical stimuli, E_{ATPase} is the energy from ATP hydrolysis of Na^+/K^+ -ATPase, and Φ_{ATP} (around 75% to 80%) [78] is the energy conversion efficiency of ATP biosynthesis by oxidation of glucose or fatty acids. The transmembrane ion concentration gradient of the cell is sustained by Na^+/K^+ -ATPase. The pumps are fuelled by ATP hydrolysis [58], consuming 5.9×10^4 J/mol (14 kcal/mol) [79].

The numerical optimization produces a configuration for the protocell that best achieves the design objective. Constrained nonlinear numerical optimization [76, 77] was used to guide the design. One of the constraints was to maintain the total channel density on each membrane while the density of individual type of channels was allowed to change in the algorithm. The resulting protocell, optimized for the electrogenic performance, with the same overall channel densities as the natural electrocyte, may produce action potentials that are longer in duration than the natural electrocyte (Figure 1(d)). The protocell design has both higher power output and greater energy conversion efficiency than a natural electrocyte (Table 1). An optimally configured protocell is predicted to produce $0.545 \text{ W} \cdot \text{m}^{-2}$ per cell; the power output density of the protocells would be linearly dependent on the layers of protocells; a protocell array with dimensions $4.3 \text{ mm} \times 4.3 \text{ mm} \times 3.9 \text{ mm}$ could continuously supply $300 \mu\text{W}$ given a sufficient energy source.

The electrogenic performance of the protocell optimized for DC output was also quantitatively analyzed with a numerical model (as described in [2]). In this protocell, the electric potential (E_t) consists of two components (Figure 2(c)): (1) the electric potential (E_r), due to the ion movement through the ion-selective membrane proteins, for example, α -HL mutants; (2) the electrode potential (E_c), due to the different activities of the two electrodes in solutions of different ion concentration;

$$E_t = E_c + E_r. \quad (4)$$

The electrode potential (E_c) is a function of chloride ion concentrations in the two droplets [72, 73]:

$$E_c = \frac{RT}{F} \ln \frac{a_{\text{Cl}^-, \text{Anode}}}{a_{\text{Cl}^-, \text{Cathode}}} = \frac{RT}{F} \ln \frac{\gamma_B m_B}{\gamma_A m_A}. \quad (5)$$

$a_{\text{Cl}^-, \text{Anode}}$ and $a_{\text{Cl}^-, \text{Cathode}}$ are the chemical activities of chloride ions around the two electrodes; γ_B is the activity coefficient of the ions in the droplet B ; m_B is the molality

($\text{mol} \cdot \text{kg}^{-1}$) of droplet B ; γ_A and m_A are those for the droplet A . R is the gas constant; T is temperature; F is the Faraday constant.

The potential E_r , from the unbalanced ion transport through the ion selective α -HL mutants, is depicted by a simplified version of Hodgkin-Huxley model [17]:

$$I = C \frac{dE_r}{dt} + g_K(E_r - V_K) + g_{\text{Cl}}(E_r - V_{\text{Cl}}). \quad (6)$$

I is the current through the lipid bilayer; C is the membrane capacitance; g_K and g_{Cl} are the K^+ and Cl^- conductance's of the α -HL mutants; V_K and V_{Cl} are the reversal potentials of K^+ and Cl^- ions.

The total voltage output (E_t) of this protocell is coupled electrically by Kirchhoff's laws through the external circuit (Figure 2(a)). As seen in Figure 2(c), the total voltage output E_t is the summation of the potential E_r due to the unbalanced ion transport and the potential E_c due to the chemical activities of electrodes in the different solutions. Over time, E_t of the protocell decreases from the initial value, due to the shrinkage of ion gradient through the lipid bilayer, which comes from both the ion exchange through the proteins and the water exchange through the lipid bilayer; in this procedure, the relative droplet sizes may vary over time. The shrinkage of ion gradient causes the decrease of both E_r (6) and E_c (5). Eventually, the ion concentrations in the two droplets reach equilibrium, which is the end of life of this protocell. During its lifetime, the protocell outputs electricity to power the external circuit (Figure 2(a)); the total energy output density (w) of this protocell is defined as

$$w = \frac{W}{V} = \frac{\int E_t I dt}{V}. \quad (7)$$

W is the energy output of the protocell; V (m^3) is the volume of the protocell.

The energy conversion efficiency is defined as the ratio of the energy output to the free energy stored in the ion concentration gradient. The unitary free energy stored in the concentration gradient, dG_0 ($\text{J} \cdot \text{mol}^{-1}$), is given by [15]

$$dG_0 = RT \ln \left(\frac{S_B}{S_A} \right). \quad (8)$$

S_A and S_B ($\text{mol} \cdot \text{L}^{-1}$) are the ion concentrations of the two droplets; R and T are the gas constant and the temperature.

The critical parameters affecting the electrogenic performance (e.g., energy output density, and energy efficiency) are the ion selectivity and channel density (using α -HL mutants in the model), the lipid bilayer area, the initial ion concentrations, and the volumes of the two droplets and the external resistance. The design was numerically optimized by varying these device parameters using a constrained nonlinear optimization algorithm [76, 77]. The constraints include the solubility of the ions in the water and the upper limit of channel density in the membrane. The objective function was the total electrogenic performance of the protocell over its lifetime—either the energy density or energy conversion efficiency. The optimization algorithm varies the parameters

TABLE 1: The calculated electrogenic performance of three cell types: the natural electrocyte, and the optimized protocell with AC output, and the optimized protocell with DC output.

Cells	Electrocyte	Optimized AC protocell	DC protocell
Maximum power density ($\text{W}\cdot\text{kg}^{-1}$)	3.28	4.19	12.6
Maximum energy density ($\text{W}\cdot\text{h}\cdot\text{kg}^{-1}$)	3.28*	4.19*	1.92
Maximum energy conversion efficiency (%)	14.7	19.7	48 [†]

*: The energy densities of these two cells are estimated based on simulations of one hour continuous output; but the actual energy densities may be even larger with enough ATP supplied; *Electrophorus electricus* can generate low-level action potentials for hours without any sign of exhaustion [80, 81].

†: The protocell designed for DC output can reach an energy conversion efficiency of 48%; but this configuration has impractically low energy density ($1.74 \times 10^3 \text{ J}\cdot\text{m}^{-3}$, i.e., $4.83 \times 10^{-4} \text{ W}\cdot\text{h}\cdot\text{kg}^{-1}$). This protocell designed for maximum energy density ($6.9 \times 10^6 \text{ J}\cdot\text{m}^{-3}$, i.e., $1.92 \text{ W}\cdot\text{h}\cdot\text{kg}^{-1}$) has an energy conversion efficiency of 10%.

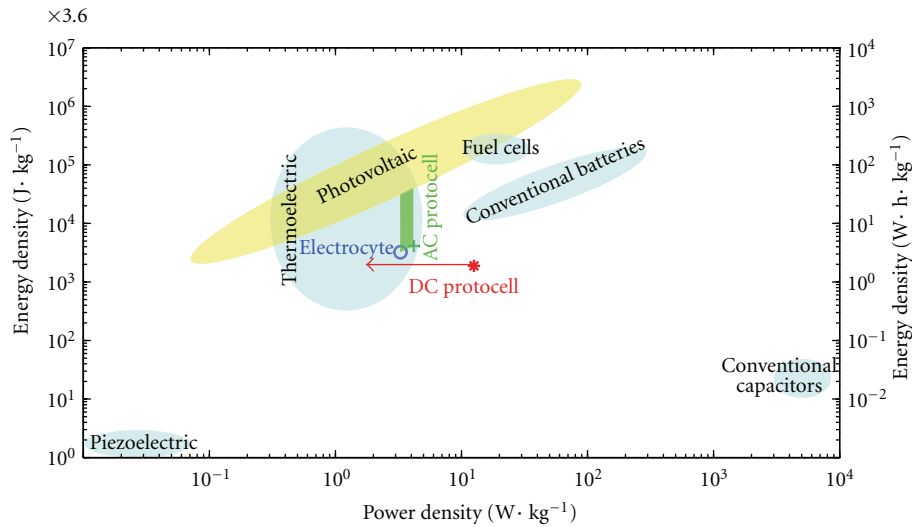


FIGURE 3: Ragone chart comparing the natural electrocyte, AC protocells, and DC protocells with conventional batteries, capacitors, and other energy conversion devices, including piezoelectric, thermoelectric, and photovoltaic devices (data for these other devices from [28, 85, 86, 88–90]). The AC protocell performance is described by a parallelogram; the bottom edge indicates the performance of AC protocells from initial design parameters (i.e., the natural electrocyte, marked with “○”) to the optimal design parameters (marked with “+”) at 1 h continuous output; the top edge indicates the performance of AC protocells at 10 h continuous output; the left and right sides reflect the performance of AC protocells spanning from 1 h to 10 h.

and evaluate the electrogenic performance of the protocell at this set of parameters; the electrogenic performance at this point will be compared to that of the previous set of parameters; based on the comparison results, decisions will be made to either stop the optimization or to further vary the parameters to maximize the electrogenic performance.

The design optimized for maximum energy density output is estimated to produce $6.9 \times 10^6 \text{ J}\cdot\text{m}^{-3}$ energy ($\approx 1.92 \text{ W}\cdot\text{h}\cdot\text{kg}^{-1}$), with an estimated energy conversion efficiency of 10%; the energy density is $\approx 5\%$ that of a lead-acid battery [82, 83]. The energy output calculated for a protocell optimally configured for high-energy density ($6.92 \times 10^6 \text{ J}\cdot\text{m}^{-3}$), with two pairs of droplets with diameters 3.9 cm and 3.3 cm, shows it could power a typical electronic gadget ($\approx 20 \text{ mW}$) for about 10 h.

Higher-energy conversion efficiency can be obtained at the expense of reducing the energy density. The maximum energy conversion efficiency calculated for these protocells reached 48%, but at that point the energy density is quite low ($1.74 \times 10^3 \text{ J}\cdot\text{m}^{-3}$) and not practical for portable applications.

Ragone charts [84–87] compare the performance of electrical energy storage devices, and provide a representation of the energy density related to the speed over which the energy can be delivered (e.g., power density). Conventional batteries and capacitors generally fall towards different ends of a Ragone chart: batteries generally deliver limited power over longer times [84–86]; capacitors generally deliver larger pulses for short times [87]. The Ragone positions of the natural electrocyte, the protocell with AC output and the protocell with DC output are plotted along with other technologies, shown for reference, in Figure 3. The maximum power output of the natural electrocyte (or a protocell with the exact same configuration as the natural electrocyte) is estimated to be $0.427 \text{ W}\cdot\text{m}^{-2}\cdot\text{cell}^{-1}$; each cell layer is $130 \mu\text{m}$ wide; if the mass density of the electrocyte is assumed to be $1 \times 10^3 \text{ kg}\cdot\text{m}^{-3}$ (the major constituent being water), the power density of the natural electrocyte is estimated to be $3.28 \text{ W}\cdot\text{kg}^{-1}$; the power density of the protocell with optimized configuration is estimated to be $4.19 \text{ W}\cdot\text{kg}^{-1}$ (Table 1). Upon stimulus, *Electrophorus*

electricus can generate action potentials for hours without any sign of exhaustion through its main organ [80, 81]; the positions of the natural electrocyte and the AC protocell with optimal design are marked (“○” and “+”) based on simulation results assuming one-hour continuous energy output, but their actual energy densities may be even higher if enough ATP was available. Therefore, the position of the AC protocell in the Ragone chart is described by a parallelogram; the vertical range indicates the performance of AC protocell spanning from 1 h to 10 h at given design parameters, which designates that the actual energy densities of AC protocells could be even larger than the current estimation with enough ATP; the horizontal range of the parallelogram indicates the range of performance of AC protocells from initial design parameters to optimal design parameters.

The protocell designed for DC output is estimated to produce $6.9 \times 10^6 \text{ J} \cdot \text{m}^{-3}$, equivalent to $1.92 \text{ W} \cdot \text{h} \cdot \text{kg}^{-1}$; the average power density is $12.6 \text{ W} \cdot \text{kg}^{-1}$, calculated from the energy density and the lifetime of the protocell (lifetime is limited by the initial concentration and discharge rate in this case). The lifetime scales linearly with the volume; droplets with 10-times larger diameters have 1000-times larger volumes and would have 1000-times longer lifetime but the total energy density available for output would remain the same at $1.92 \text{ W} \cdot \text{h} \cdot \text{kg}^{-1}$. Therefore, the position of the protocell with DC output in the Ragone chart is depicted by a star (*) with dotted lines, indicating that depending on the droplet sizes, the same energy density may be delivered more slowly and at lower power density than the results based on a configuration calculated with droplets of 254 nL and 146 nL. The energy density of the DC protocell is $\approx 5\%$ that of a lead-acid battery [82, 83]; the power density of the DC protocell is comparable to traditional batteries. Compared with other alternative energy conversion devices (Figure 3), the electrogenic performance of protocells is much better than that of the piezoelectric devices and comparable to that of thermoelectric and photovoltaic devices. The photovoltaic devices have dramatically worse performance (e.g., the power density of $\approx 10 \mu\text{W} \cdot \text{cm}^{-2}$) when used indoors than outdoors (power density of $\approx 1.5 \times 10^4 \mu\text{W} \cdot \text{cm}^{-2}$); when compared to the indoor performance, the protocells have larger power density than the photovoltaic devices. In addition, the AC protocell can be recharged using a biological energy source, for example, ATP, which seems appealing for powering implantable devices.

The protocell technologies summarized here may be of use for energy conversion where large-scale ion concentration gradients are available (such as the intersection of fresh and salt water sources) and for those applications where low power density is not a limiting factor.

4. Conclusion

Protocells, by assembling natural and synthetic nanoscale conductors (e.g., ion channels/pumps), provide a new approach to convert chemical energy (or energy stored in a concentration gradient) into electricity. The electrogenic performance of these protocells has been numerically modeled and effectively enhanced by optimization. The optimized

designs produce energy densities sufficiently large for practical applications, from low-power consumer electronics to implantable biomedical devices.

The challenges to this technology lay in creating stable and selective channels and ion pumps—natural membrane proteins are currently purified and inserted into lipid bilayers [91, 92]. Synthetic counterparts of ion channels can be synthesized by protein engineering, such as α -hemolysin and its mutants [63, 71]. Artificial ion channels may also be fabricated by precisely tailoring the radii of SiO_2 nanopores through organic group functionalization [93, 94]. Of course, long-term stability is another concern—the droplet bilayer is one approach, which has been reported to extend bilayer lifetimes [64–68]. Other approaches for stabilizing the lipid bilayer include mesoporous silica [11] or nanofiber support [12]; these porous supports not only stabilize the lipid bilayer but also maintain water accessibility to both sides of the bilayer [12], which is critical for device function. As is done with conventional batteries, multiple protocells could be connected in series and/or parallel to achieve needed voltage and current outputs.

Acknowledgments

This paper was supported in part by the National Institutes of Health through the NIH Roadmap for Medical Research, as part of the National Center for Design of Biomimetic Nanoconductors, award number PHS 2 PN2 EY016570B. The full description of the materials and software used in this paper requires the identification of certain products, materials, and software suppliers. The inclusion of such information should in no way be construed as indicating that such products, materials, or software are endorsed by NIST or are recommended by NIST or that they are necessarily the best products, materials, or software for the purposes described.

References

- [1] J. Xu and D. A. Lavan, “Designing artificial cells to harness the biological ion concentration gradient,” *Nature Nanotechnology*, vol. 3, no. 11, pp. 666–670, 2008.
- [2] J. Xu, F. J. Sigworth, and D. A. Lavan, “Synthetic protocells to mimic and test cell function,” *Advanced Materials*, vol. 22, no. 1, pp. 120–127, 2010.
- [3] W. Hanke and W. Schlue, *Planar Lipid Bilayers: Methods and Applications*, Academic Press, San Diego, Calif, USA, 1993.
- [4] D. Gallez, N. M. C. Pinto, and P. M. Bisch, “Nonlinear dynamics and rupture of lipid bilayers,” *Journal of Colloid And Interface Science*, vol. 160, no. 1, pp. 141–148, 1993.
- [5] P. F. Fahey, D. E. Koppel, L. S. Barak et al., “Lateral diffusion in planar lipid bilayers,” *Science*, vol. 195, no. 4275, pp. 305–306, 1977.
- [6] B. Hille, *Ion Channels of Excitable Membranes*, Sinauer Associates, Sunderland, Mass, USA, 3rd edition, 2001.
- [7] C. M. Armstrong, “Inactivation of the sodium channel. II. Gating current experiments,” *Journal of General Physiology*, vol. 70, no. 5, pp. 567–590, 1977.
- [8] A. Gotter, M. Kaetzel, and J. Dedman, “Electrophorus electricus as a model system for the study of membrane excitability,” *Comparative Biochemistry and Physiology A*, vol. 119, no. 1, pp. 225–241, 1998.

- [9] W. B. Thornhill, I. Watanabe, J. J. Sutachan et al., "Molecular cloning and expression of a Kv1.1-like potassium channel from the electric organ of *Electrophorus electricus*," *Journal of Membrane Biology*, vol. 196, no. 1, pp. 1–8, 2003.
- [10] F. H. Yu and W. A. Catterall, "Overview of the voltage-gated sodium channel family," *Genome Biology*, vol. 4, no. 3, article no. 207, 2003.
- [11] J. Brinker, Y. Lu, A. Sellinger, and H. Fan, "Evaporation-induced self-assembly: nanostructures made easy," *Advanced Materials*, vol. 11, no. 7, pp. 579–585, 1999.
- [12] F. Yi, J. Xu, A. M. Smith, A. N. Parikh, and D. A. Lavan, "Nanofiber-supported phospholipid bilayers," *Soft Matter*, vol. 5, no. 24, pp. 5037–5041, 2009.
- [13] J. J. Kasianowicz, D. L. Burden, L. C. Han, S. Cheley, and H. Bayley, "Genetically engineered metal ion binding sites on the outside of a channel's transmembrane β -barrel," *Biophysical Journal*, vol. 76, no. 2, pp. 837–845, 1999.
- [14] C. Armstrong and B. Hille, "Voltage-gated ion channels and electrical excitability," *Neuron*, vol. 20, no. 3, pp. 371–380, 1998.
- [15] J. Berg, J. Tymoczko, and L. Stryer, *Biochemistry*, W. H. Freeman and Company, New York, NY, USA, 2001.
- [16] I. Levitan and L. Kaczmarek, *The Neuron*, Oxford University Press, New York, NY, USA, 2002.
- [17] A. Hodgkin and A. F. Huxley, "A quantitative description of membrane current and its application to conduction and excitation in nerve," *The Journal of Physiology*, vol. 117, no. 4, pp. 500–544, 1952.
- [18] L. E. Bell, "Cooling, heating, generating power, and recovering waste heat with thermoelectric systems," *Science*, vol. 321, no. 5895, pp. 1457–1461, 2008.
- [19] S. B. Riffat and X. Ma, "Thermoelectrics: a review of present and potential applications," *Applied Thermal Engineering*, vol. 23, no. 8, pp. 913–935, 2003.
- [20] T. Cole, "Thermoelectric energy conversion with solid electrolytes," *Science*, vol. 221, no. 4614, pp. 915–920, 1983.
- [21] R. L. Bunde, E. J. Jarvi, and J. J. Rosentreter, "Piezoelectric quartz crystal biosensors," *Talanta*, vol. 46, no. 6, pp. 1223–1236, 1998.
- [22] Y. S. Fung and Y. Y. Wong, "Self-assembled monolayers as the coating in a quartz piezoelectric crystal immunosensor to detect Salmonella in aqueous solution," *Analytical Chemistry*, vol. 73, no. 21, pp. 5302–5309, 2001.
- [23] R. R. King, D. C. Law, K. M. Edmondson et al., "40% efficient metamorphic GaInP/GaInAs/Ge multijunction solar cells," *Applied Physics Letters*, vol. 90, no. 18, Article ID 183516, 3 pages, 2007.
- [24] A. Barnett, D. Kirkpatrick, C. Honsberg et al., "Very high efficiency solar cell modules," *Progress in Photovoltaics: Research and Applications*, vol. 17, no. 1, pp. 75–83, 2008.
- [25] S. A. Sapp, B. B. Lakshmi, and C. R. Martin, "Template synthesis of bismuth telluride nano wires," *Advanced Materials*, vol. 11, no. 5, pp. 402–404, 1999.
- [26] O. Yamashita, S. Tomiyoshi, and K. Makita, "Bismuth telluride compounds with high thermoelectric figures of merit," *Journal of Applied Physics*, vol. 93, no. 1, pp. 368–374, 2003.
- [27] R. Yang, Y. Qin, L. Dai, and Z. L. Wang, "Power generation with laterally packaged piezoelectric fine wires," *Nature Nanotechnology*, vol. 4, no. 1, pp. 34–39, 2008.
- [28] S. Roundy, E. S. Leland, J. Baker et al., "Improving power output for vibration-based energy scavengers," *IEEE Pervasive Computing*, vol. 4, no. 1, pp. 28–36, 2005.
- [29] S. Roundy, P. K. Wright, and J. M. Rabaey, *Energy Scavenging for Wireless Sensor Networks: With Special Focus on Vibrations*, Springer, New York, NY, USA, 2004.
- [30] J. A. Paradiso and T. Starner, "Energy scavenging for mobile and wireless electronics," *IEEE Pervasive Computing*, vol. 4, no. 1, pp. 18–27, 2005.
- [31] A. Iino, K. Suzuki, M. Kasuga, M. Suzuki, and T. Yamanaka, "Development of a self-oscillating ultrasonic micro-motor and its application to a watch," *Ultrasonics*, vol. 38, no. 1–8, pp. 54–59, 2000.
- [32] K. Ramanathan, M. A. Contreras, C. L. Perkins et al., "Properties of 19.2% efficiency ZnO/CdS/CuInGaSe₂ thin-film solar cells this article is a US Government work and is in the public domain in the USA," *Progress in Photovoltaics: Research and Applications*, vol. 11, no. 4, pp. 225–230, 2003.
- [33] P. Liska, K. R. Thampi, M. Gratzel et al., "Nanocrystalline dye-sensitized solar cell/copper indium gallium selenide thin-film tandem showing greater than 15% conversion efficiency," *Applied Physics Letters*, vol. 88, Article ID 203103, 3 pages, 2006.
- [34] G. J. Bauhuis, P. Mulder, J. J. Schermer, E. J. Haverkamp, J. van Deelen, and P. K. Larsen, "High efficiency thin film GaAs solar cells with improved radiation hardness," in *Proceedings of the 20th European Photovoltaic Solar Energy Conference*, pp. 468–471, Barcelona, Spain, June 2005.
- [35] J. C. Skou, "The identification of the sodium pump," *Bioscience Reports*, vol. 18, no. 4, pp. 155–169, 1998.
- [36] F. Cornelius, "The sodium pump," in *ATPases (Biomembranes A Multi-Volume Treatise)*, A. G. Lee, Ed., p. 133, JAI Press, London, UK, 1996.
- [37] J. K. Lanyi and A. Pohorille, "Proton pumps: mechanism of action and applications," *Trends in Biotechnology*, vol. 19, no. 4, pp. 140–144, 2001.
- [38] H. Noji, R. Yasuda, M. Yoshida, and K. Kinoshita, "Direct observation of the rotation of F₁-ATPase," *Nature*, vol. 386, pp. 299–302, 1997.
- [39] T. Elston, H. Wang, and G. Oster, "Energy transduction in ATP synthase," *Nature*, vol. 391, pp. 510–513, 1998.
- [40] W. Junge, H. Sialaff, and S. Engelbrecht, "Torque generation and elastic power transmission in the rotary F₀F₁-ATPase," *Nature*, vol. 459, pp. 364–370, 2009.
- [41] R. M. Allen and H. P. Bennetto, "Microbial fuel-cells," *Applied Biochemistry and Biotechnology*, vol. 39, no. 1, pp. 27–40, 1993.
- [42] K. Rabaey and W. Verstraete, "Microbial fuel cells: novel biotechnology for energy generation," *Trends in Biotechnology*, vol. 23, no. 6, pp. 291–298, 2005.
- [43] R. D. Machado, W. D. Souza, G. Cotta Pereira, and G. D. O. Castro, "On the fine structure of the electrocyte of *Electrophorus electricus* L.," *Cell and Tissue Research*, vol. 174, no. 3, pp. 355–366, 1976.
- [44] C. Mermelstein, M. Costa, and V. Neto, "The cytoskeleton of the electric tissue of *Electrophorus electricus*, L.," *Anais da Academia Brasileira de Ciencias*, vol. 72, no. 3, pp. 341–351, 2000.
- [45] M. Altamirano, "Electrical properties of the innervated membrane of the electroplax of electric eel," *Journal of cellular physiology*, vol. 46, no. 2, pp. 249–277, 1955.
- [46] R. T. Cox, C. W. Coates, and M. V. Brown, "Electric tissue-relations between the structure, electrical characteristics, and chemical processes of electric tissue," *Journal of General Physiology*, vol. 28, no. 3, pp. 187–212, 1945.
- [47] W. S. Hoar, *Fish Physiology: Sensory Systems and Electric Organs*, Academic Press, New York, NY, USA, 1971.

- [48] A. Hodgkin and A. Huxley, "Measurement of current-voltage relations in the membrane of the giant axon of *Loligo*," *The Journal of Physiology*, vol. 116, no. 4, pp. 424–448, 1952.
- [49] A. Hodgkin and A. Huxley, "Currents carried by sodium and potassium ions through the membrane of the giant axon of *Loligo*," *Journal of Physiology*, vol. 116, no. 4, pp. 449–472, 1952.
- [50] A. Hodgkin and A. Huxley, "The components of membrane conductance in the giant axon of *Loligo*," *The Journal of Physiology*, vol. 116, no. 4, pp. 473–496, 1952.
- [51] A. Hodgkin and A. Huxley, "The dual effect of membrane potential on sodium conductance in the giant axon of *Loligo*," *Journal of Physiology*, vol. 116, no. 4, pp. 497–506, 1952.
- [52] A. L. Hodgkin and B. Katz, "The effect of temperature on the electrical activity of the giant axon of the squid," *The Journal of Physiology*, vol. 108, no. 1, p. 37, 1949.
- [53] R. Keynes and H. Ferreira, "Membrane potentials in the electroplates of the electric eel," *Journal of Physiology*, vol. 119, pp. 315–351, 1953.
- [54] S. Shenkel and F. Bezanilla, "Patch recordings from the electrocytes of electrophorus: Na channel gating currents," *Journal of General Physiology*, vol. 98, no. 3, pp. 465–478, 1991.
- [55] H. A. Lester, J. P. Changeux, and R. E. Sheridan, "Conductance increases produced by bath application of cholinergic agonists to Electrophorus electroplaques," *Journal of General Physiology*, vol. 65, no. 6, pp. 797–816, 1975.
- [56] M. L. S. Souza, C. F. Freitas, M. A. O. Domingos et al., "Identification and distribution of chondroitin sulfate in the three electric organs of the electric eel, *Electrophorus electricus* (L.)," *Comparative Biochemistry and Physiology B*, vol. 146, no. 2, pp. 227–233, 2007.
- [57] Y. Nakamura, S. Nakajima, and H. Grundfest, "Analysis of spike electrogenesis and depolarizing K inactivation in electroplaques of *Electrophorus electricus*, L," *The Journal of General Physiology*, vol. 49, no. 2, p. 321, 1965.
- [58] C. Tanford, "Equilibrium state of ATP-driven ion pumps in relation to physiological ion concentration gradients," *Journal of General Physiology*, vol. 77, no. 2, pp. 223–229, 1981.
- [59] H. J. Choi and C. D. Montemagno, "Artificial organelle: ATP synthesis from cellular mimetic polymersomes," *Nano Letters*, vol. 5, no. 12, pp. 2538–2542, 2005.
- [60] D. Bald, T. Amano, E. Muneyuki et al., "ATP synthesis by F₀F₁-ATP synthase independent of noncatalytic nucleotide binding sites and insensitive to azide inhibition," *Journal of Biological Chemistry*, vol. 273, no. 2, pp. 865–870, 1998.
- [61] B. Pitard, P. Richard, M. Dunach, and J. L. Rigaud, "ATP synthesis by the F₀F₁ ATP synthase from thermophilic *Bacillus* PS3 reconstituted into liposomes with bacteriorhodopsin 2. Relationships between proton motive force and ATP synthesis," *European Journal of Biochemistry*, vol. 235, no. 3, pp. 779–788, 1996.
- [62] B. Pitard, P. Richard, M. Dunach, G. Girault, and J. L. Rigaud, "ATP synthesis by the F₀F₁ ATP synthase from thermophilic *Bacillus* PS3 reconstituted into liposomes with bacteriorhodopsin 1. Factors defining the optimal reconstitution of ATP synthases with bacteriorhodopsin," *European Journal of Biochemistry*, vol. 235, no. 3, pp. 769–778, 1996.
- [63] P. G. Merzlyak, M. F. P. Capistrano, A. Valeva, J. J. Kasianowicz, and O. V. Krasilnikov, "Conductance and ion selectivity of a mesoscopic protein nanopore probed with cysteine scanning mutagenesis," *Biophysical Journal*, vol. 89, no. 5, pp. 3059–3070, 2005.
- [64] M. A. Holden, D. Needham, and H. Bayley, "Functional bionetworks from nanoliter water droplets," *Journal of the American Chemical Society*, vol. 129, no. 27, pp. 8650–8655, 2007.
- [65] W. L. Hwang, M. A. Holden, S. White, and H. Bayley, "Electrical behavior of droplet interface bilayer networks: experimental analysis and modeling," *Journal of the American Chemical Society*, vol. 129, no. 38, pp. 11854–11864, 2007.
- [66] M. A. Creasy and D. J. Leo, "Droplet interface bilayer characteristics formed over a synthetic porous substrate," in *Proceedings of The International Society for Optical Engineering (SPIE '09)*, vol. 7291, Nanosensors, Biosensors, and Info-Tech Sensors and Systems, March 2009.
- [67] S. A. Sarles and D. J. Leo, "Regulated attachment method for reconstituting lipid bilayers of prescribed size within flexible substrates," *Analytical Chemistry*, vol. 82, no. 3, pp. 959–966, 2010.
- [68] S. A. Sarles and D. J. Leo, "Physical encapsulation of droplet interface bilayers for durable, portable biomolecular networks," *Lab on a Chip*, vol. 10, no. 6, pp. 710–717, 2010.
- [69] L.-Q. Gu and H. Bayley, "Interaction of the noncovalent molecular adapter, β -cyclodextrin, with the staphylococcal α -hemolysin pore," *Biophysical Journal*, vol. 79, no. 4, pp. 1967–1975, 2000.
- [70] S. A. Glazier, D. J. Vanderah, A. L. Plant, H. Bayley, G. Valincius, and J. J. Kasianowicz, "Reconstitution of the pore-forming toxin α -hemolysin in phospholipid/18-octadecyl-1-thiahexa(ethylene oxide) and phospholipid/n-octadecanethiol supported bilayer membranes," *Langmuir*, vol. 16, no. 26, pp. 10428–10435, 2000.
- [71] S. Y. Noskov, W. Im, and B. Roux, "Ion permeation through the α -hemolysin channel: theoretical studies based on Brownian dynamics and Poisson-Nernst-Planck electrodiffusion theory," *Biophysical Journal*, vol. 87, no. 4, pp. 2299–2309, 2004.
- [72] W. J. Hamer and Y. C. Wu, "Osmotic coefficients and mean activity coefficients of uni-univalent electrolytes in water at 25 C," *Journal of Physical and Chemical Reference Data*, vol. 1, no. 4, pp. 1047–1075, 1972.
- [73] E. Amado G and L. H. Blanco, "Osmotic and activity coefficients of aqueous solutions of KCl at temperatures of 283.15, 288.15, 293.15 and 298.15 K: a new isopiestic apparatus," *Fluid Phase Equilibria*, vol. 226, no. 1-2, pp. 261–265, 2004.
- [74] J. Novotny and E. Jakobsson, "Computational studies of ion-water flux coupling in the airway epithelium. I. Construction of model," *American Journal of Physiology*, vol. 270, no. 6, pp. C1751–C1763, 1996.
- [75] J. Novotny and E. Jakobsson, "Computational studies of ion-water flux coupling in the airway epithelium. II. Role of specific transport mechanisms," *American Journal of Physiology*, vol. 270, no. 6, pp. C1764–C1772, 1996.
- [76] J. More, "The Levenberg-Marquardt algorithm: implementation and theory," *Numerical Analysis*, vol. 630, pp. 105–116, 1978.
- [77] T. S. Ahearn, R. T. Staff, T. W. Redpath, and S. I. K. Semple, "The use of the Levenberg-Marquardt curve-fitting algorithm in pharmacokinetic modelling of DCE-MRI data," *Physics in Medicine and Biology*, vol. 50, no. 9, pp. N85–N92, 2005.
- [78] H. Kammermeier, "Efficiency of energy conversion from metabolic substrates to ATP and mechanical and chemiosmotic energy," *Basic Research in Cardiology*, vol. 88, supplement 2, pp. 15–20, 1993.
- [79] P. C. Caldwell and H. Schirmer, "The free energy available to the sodium pump of squid giant axons and changes in the sodium efflux on removal of the extracellular potassium," *Journal of Physiology*, vol. 181, pp. 25P–26P, 1965.

- [80] J. S. Nelson, *Fishes of the World*, Wiley, 2006.
- [81] P. Moller, *Electric Fishes: History and Behavior*, Chapman & Hall, London, UK, 1995.
- [82] B. Hariprakash, A. U. Mane, S. K. Martha, S. A. Gaffoor, S. A. Shivashankar, and A. K. Shukla, "A low-cost, high energy-density lead/acid battery," *Electrochemical and Solid-State Letters*, vol. 7, no. 3, pp. A66–A69, 2004.
- [83] T. Juergens and R. F. Nelson, "A new high-rate, fast-charge lead/acid battery," *Journal of Power Sources*, vol. 53, no. 2, pp. 201–205, 1995.
- [84] G. Delille and B. Francois, "A review of some technical and economic features of energy storage technologies for distribution system integration," in *Proceedings of the Electrical Machines, Drives and Power Systems (ELMA '08)*, pp. 67–72, 2008.
- [85] J. M. Miller, "Energy storage technology markets and application's: ultracapacitors in combination with lithium-ion," in *Proceedings of the 7th International Conference on Power Electronics (ICPE '07)*, pp. 16–22, October 2007.
- [86] P. Van den Bossche, F. Vergels, J. Van Mierlo, J. Matheys, and W. Van Autenboer, "SUBAT: an assessment of sustainable battery technology," *Journal of Power Sources*, vol. 162, no. 2, pp. 913–919, 2006.
- [87] J. M. Miller and R. Smith, "Ultra-capacitor assisted electric drives for transportation," in *Proceedings of the IEEE International Electric Machines and Drives Conference*, vol. 2, pp. 670–676, June 2003.
- [88] C. Knight, J. Davidson, and S. Behrens, "Energy options for wireless sensor nodes," *Sensors*, vol. 8, no. 12, pp. 8037–8066, 2008.
- [89] K. Yoshida, S. Tanaka, S. Tomonari, D. Satoh, and M. Esashi, "High-energy density miniature thermoelectric generator using catalytic combustion," *Journal of Microelectromechanical Systems*, vol. 15, no. 1, pp. 195–203, 2006.
- [90] G. L. Bennett, "Space nuclear power: opening the final frontier," in *Proceedings of the 4th International Energy Conversion Engineering Conference and Exhibit*, San Diego, Calif, USA, 2006.
- [91] E. Recio-Pinto, D. Duch, S. Levinson, and B. W. Urban, "Purified and unpurified sodium channels from eel electroplax in planar lipid bilayers," *Journal of General Physiology*, vol. 90, no. 3, pp. 375–395, 1987.
- [92] S. Shenkel, E. C. Cooper, W. James, W. Agnew, and F. Sigworth, "Purified, modified eel sodium channels are active in planar bilayers in the absence of activating neurotoxins," *Proceedings of the National Academy of Sciences of the United States of America*, vol. 86, no. 23, pp. 9592–9596, 1989.
- [93] Y.-B. Jiang, G. Xomeritakis, Z. Chen et al., "Sub-10 nm thick microporous membranes made by plasma-defined atomic layer deposition of a bridged silsesquioxane precursor," *Journal of the American Chemical Society*, vol. 129, no. 50, pp. 15446–15447, 2007.
- [94] N. Liu, R. A. Assink, and C. J. Brinker, "Synthesis and characterization of highly ordered mesoporous thin films with-COOH terminated pore surfaces," *Chemical Communications*, vol. 9, no. 3, pp. 370–371, 2003.

Review Article

Development of Polymeric Cargo for Delivery of Photosensitizer in Photodynamic Therapy

Byoung-chan Bae and Kun Na

Department of Biotechnology, The Catholic University of Korea, 43-1 Yeokkok2-dong, Wonmi-gu, Bucheon-si, Gyeonggi-do 420-743, Republic of Korea

Correspondence should be addressed to Kun Na, kna6997@catholic.ac.kr

Received 15 May 2011; Accepted 28 June 2011

Academic Editor: Tebello Nyokong

Copyright © 2012 B.-c. Bae and K. Na. This is an open access article distributed under the Creative Commons Attribution License, which permits unrestricted use, distribution, and reproduction in any medium, provided the original work is properly cited.

Photodynamic therapy (PDT), which employs photosensitizers (PSs), a light source with appropriate wavelength, and oxygen molecules, has potential for the treatment of various tumors and nononcological diseases due to its high efficiency in directly producing cellular death, vascular shutdown, and immune activation. After the clinical success of Photofrin (porphyrin derivative), many PSs were developed with improved optical and chemical properties. However, some weak points such as low solubility and nonspecific phototoxicity induced by hydrophobic PSs still remain. In order to overcome these problems, various polymeric carriers for PS delivery have been intensively developed. Here, we report recent approaches to the development of polymeric carriers for PS delivery and discuss the physiological advantages of using polymeric carriers in PDT. Therefore, this paper provides helpful information for the design of new PSs without the weaknesses of conventional ones.

1. Introduction

The therapeutic application of light began in 1900 when Raab reported that the combination of acridine orange and light could destroy living organisms (paramecium) [1].

Recently, photodynamic therapy (PDT) has been intensively studied and employed as a modality for the treatment of various tumors and nononcological diseases due to its unique properties [2, 3]. This modality involves a non-invasive process that has minimal nonspecific effects on normal tissues, although some problems such as high cost and short-term period for retreatment still remain. PDT was first approved for skin cancer by the Canadian FDA in 1994. As illustrated in Figure 1 [4] PSs exposed to light of an appropriate wavelength are excited to singlet states (S_1). PSs can relax back to ground state by emitting a fluorescent photon (S_0) or be excited to triplet states via intersystem crossing (ISC; T_1). From triplet excited states, PSs can relax back to ground state by emitting a phosphorescent photon or by transferring energy to another molecule via radiationless transition [5]. In addition, PSs can transfer energy to other molecules via type I and type II reaction processes. In the type I reaction, free radicals formed by

hydrogen- or electron-transfer from PSs react with oxygen, thereby producing reactive oxygen species (ROS), including superoxide (O_2^-) and peroxide anions (O_2^{2-}). In the type II reaction, PSs in the excited triplet state directly transfer energy to molecular oxygen in a triplet ground state (3O_2), resulting in the formation of highly reactive singlet oxygen (1O_2). In PDT, these ROS oxidize (photodamage) subcellular organelles and other biomolecules, leading to light-induced cell death. Indeed, PDT using PSs has been used to treat esophageal cancer in the United States and Canada, early- and late-stage lung cancer in The Netherlands, bladder cancer in Canada, and early-stage lung, oesophageal, gastric, and cervical cancers in Japan [6].

In this review, we focused on the key factors of PSs (PS type, light source, and oxygen molecules) in PDT, since the side effects and efficacy of PDT are determined by the properties of the PS. PSs were divided in three generations: 1st generation was based on porphyrin (first clinically used product) [5], 2nd generation was chlorin derivatives for improvement of solubility in water [7–10], and 3rd generation was polymeric PS with enhanced target specificity [11–17].

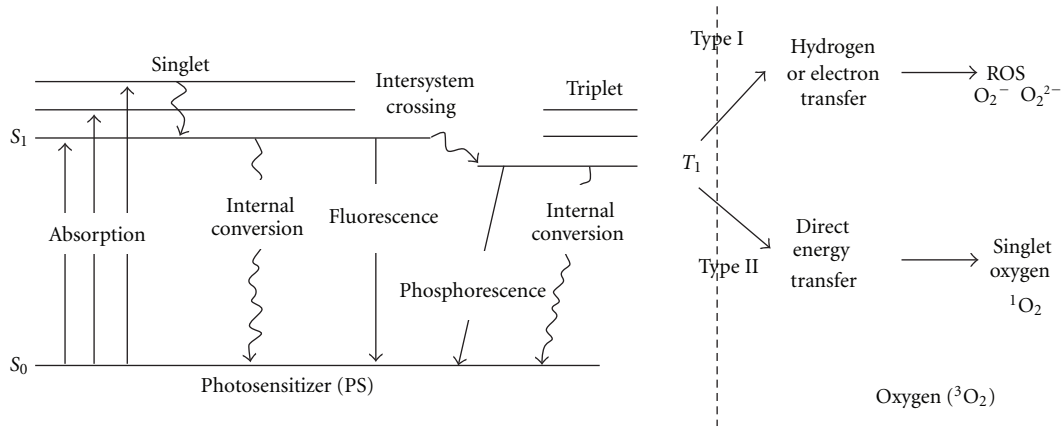


FIGURE 1: Jablonski diagram showing energy transfer from photosensitizers (PSs) to molecular oxygen [4].

TABLE 1: Approved or currently on-trial PSs [2].

Sensitizer	Trade name	Potential indications	Activation wavelength
HPD (partially purified), porfimer sodium	Photofrin	Cervical endobronchial, oesophageal, bladder, gastric cancer, and brain tumors	630 nm
BPD-MA	Verteporfin	Basal-cell carcinoma	689 nm
m-THPC	Foscan	Head and neck tumors prostate and pancreatic tumors	652 nm
5- ALA	Levulan	Basal-cell carcinoma, head and neck, and gynaecological tumors	635 nm
5-ALA-methylester	Metvix	Diagnosis of brain, head and neck, and bladder tumors	375~400 nm
5-ALA-benzylester	Benzvix	Basal-cell carcinoma	635 nm
5-ALA-hexylester	Hexvix	Gastrointestinal cancer	635 nm
SnETs	Purlytin	Diagnosis of bladder tumors	375~400 nm
Boronated protoporphyrin	BOPP	Cutaneous metastatic breast cancer, basal-cell carcinoma, Kaposi's sarcoma, and prostate cancer	664 nm
HPPH	Photochlor	Brain tumors	630 nm
Lutetium texaphyrin	Lutex	Basal-cell carcinoma	665 nm
Phthalocyanine-4	Pc4	Cervical, prostate, and brain tumors	732 nm
Taporfin sodium	Talaporfin	Cutaneous/subcutaneous lesions from diverse solid tumor origins	670 nm
		Solid tumors from diverse origins	664 nm

* 5-ALA: 5-aminolevulinic acid; BPD-MA: benzoporphyrin derivative-monoacid ring A; HPD: hematoporphyrin derivative; HPPH: 2-(1-Hexyl-oxyethyl)-2-divinyl pyropheophorbide-alpha; mTHPC: meta-tetrahydroxyphenylchlorin; SnET2: tin ethyl etiopurine.

2. Photosensitizers (PSs)

The most commonly used and studied PSs to date are porphyrin derivatives such as Photofrin and Photogem. These materials are 1st generation PSs and are among the most useful PSs for clinical trials (Table 1) [2]. These PSs have absorption maxima in the red portion of the spectrum and are efficient singlet oxygen generators. Red absorption maxima allow activating light to penetrate deeper into tissue. However, these PSs readily accumulate and stay in normal skin for a longtime, leading to severe sunburning and photo-reaction. Their side effects are inhibited by avoiding daylight and high-energy light, or by wearing protective clothing and sunglasses for approximately 6 weeks after treatment, all of which constitute a major limitation in clinical trials.

To solve these problems, many researchers have synthesized 2nd generation PSs, which have improved physical properties such as high water solubility and photo-adsorption coefficient compared to 1st generation PSs (Figure 2). For this, second-generation PSs aim to have absorption maxima at wavelengths longer than 630 nm, since 1st generation PSs display relatively weak absorption at 630 nm that does not allow for optimal light penetration. Therefore, after a useful 2nd generation PS is identified, it is tested *in vitro* and *in vivo* for PDT activity [18].

Second-generation PSs based on chlorin show rapid clearance from the skin, and they were approved by the Japanese government and EU in 2003 [19–21]. Thus, PDT with 2nd generation PSs can reduce skin phototoxicity. However, the patient must stay in a darkened room for at

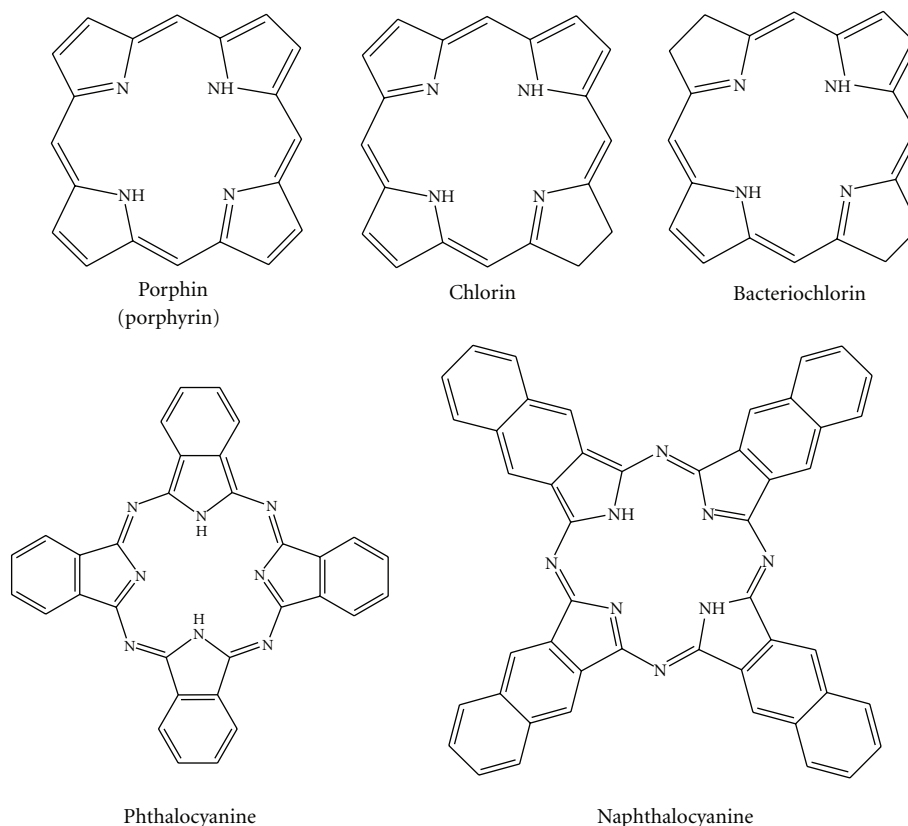


FIGURE 2: Chemical structure of various PSs.

least 2 weeks, and high target efficiency to the tumor site is required. To solve these problems, 3rd generation PSs were developed by chemical conjugation with biocompatible polymer and encapsulation in nanoparticles by physical interaction in order to reduce the toxicity to normal tissues and maximize tumor specificity. In particular, generation of PSs is often carried out by fluorescence resonance energy transfer (FRET), which can control the photoactivity of PSs by changing the environmental conditions. FRET is a distance-dependent interaction between the electronic excited states of two dye molecules in which excitation is transferred from a donor molecule to an acceptor molecule without emission of a photon [22].

3. Polymeric Carrier for Delivery of PSs

As mentioned above, PDT is often accompanied with long-lasting skin toxicity, which is a major limitation in its clinical application [2, 3, 5]. This effect is mainly due to the hydrophobic and nonspecific properties of PSs [23]. To improve the poor water solubility of PSs, a new concept was developed using polymeric carriers. In 1992, Kopeček's group began a study using a polymer-PS conjugate [24]. They reported N-(2-hydroxypropyl)methacrylamide (HPMA) copolymer containing mesochlorin e_6 monoethylene diamine disodium salt (Mce_6). The Mce_6 was bound via pendant enzymatically degradable oligopeptide side chains (G-F-L-G) in one copolymer and was attached through

noncleavable side chains (G) in the other. Preliminary experiments were also undertaken to compare their localization/retention behavior and their tumoricidal activities *in vivo* (A/J mice; C1300 neuroblastoma). The results of localization/retention experiments found that Mce_6 bound to the non-cleavable copolymer was retained in the tumor and other tissues for a prolonged time period compared to free Mce_6 or Mce_6 bound to cleavable copolymer. Light activation of Mce_6 from the cleavable copolymer resulted in a substantially more potent biological response *in vivo* than did the permanently bound Mce_6 . It was thus hypothesized and indirectly supported by photophysical data that both of the polymer-photosensitizer complexes are aggregated (or conformationally altered) under physiological conditions due to their hydrophilic/hydrophobic properties. In buffer at pH 7.4, the quantum yield of singlet oxygen generation by free Mce_6 was three-fold higher than that by Mce_6 bound to non-cleavable copolymer; adding detergent increased the quantum yield of singlet oxygen generation to a value consistent with that of free Mce_6 . *In vivo*, if a sufficient time lag is allowed after drug administration for tumor cell lysosomal enzymes to cleave Mce_6 from the polymer containing degradable side chains, then Mce_6 is released in free form and behaves similar to the free drug. The other approach using a dendrimeric PS system was reported by Kataoka's group [17, 25]. In that report, to enhance the efficacy of PDT, a new photosensitizer formulation, that is, dendrimer phthalocyanine- (DPC-) encapsulated polymeric

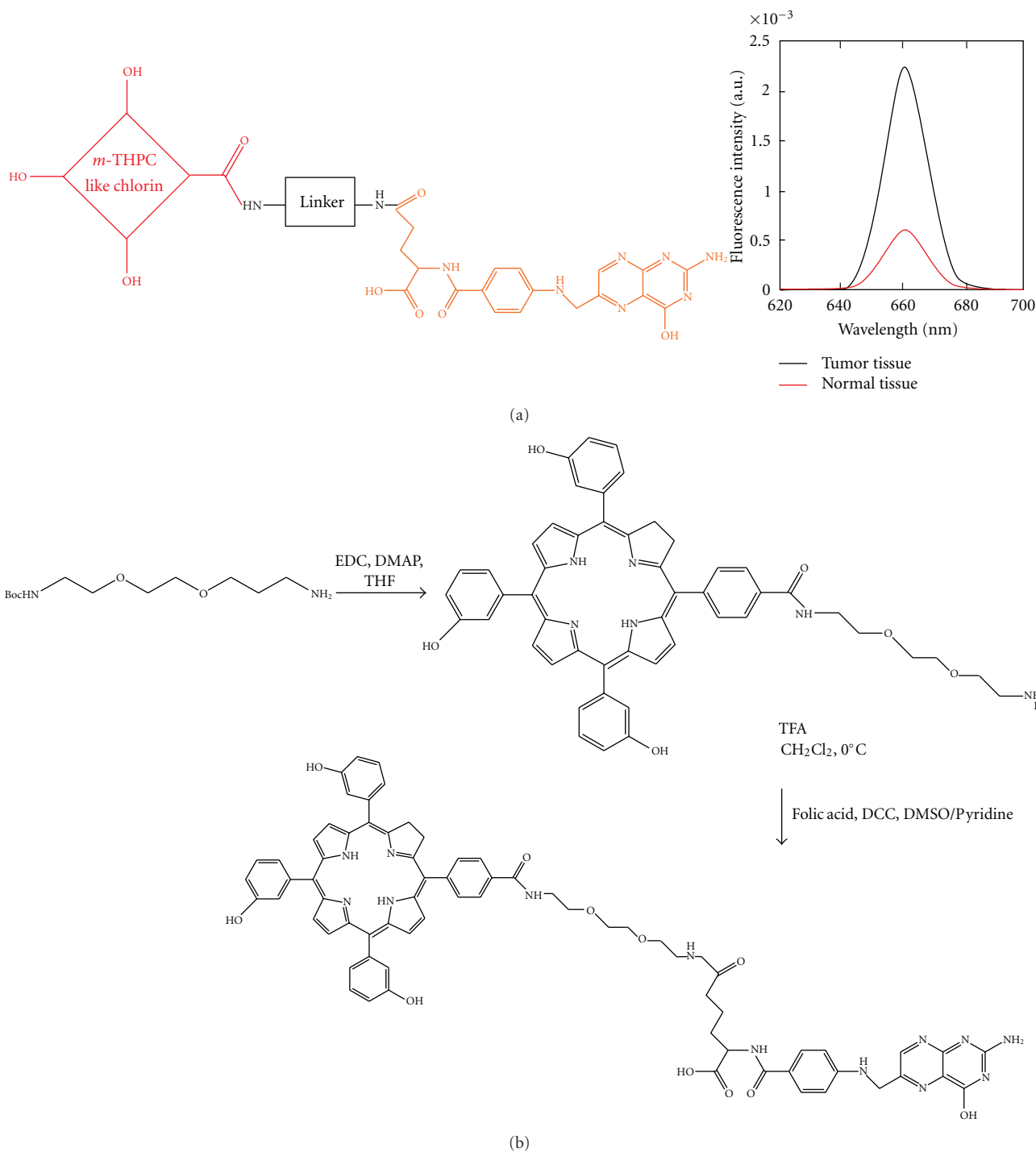


FIGURE 3: Chemical synthetic method and target specificity of folate conjugate with chlorin-based tris(3-Hydroxyphenyl)-4-carboxyphenylchlorin [37].

micelle (DPC/m), was developed. DPC/m induced efficient and rapid cell death accompanied by characteristic morphological changes, such as blabbing of cell membranes, when the cells were photoirradiated using a low-power halogen lamp or high-power diode laser. Fluorescent microscopic observation using organelle-specific dyes demonstrated that DPC/m might accumulate in the endo-/lysosomes; however,

upon photoirradiation, DPC/m might be promptly released into the cytoplasm and photodamage the mitochondria, which may account for the enhanced photocytotoxicity of DPC/m. This study also demonstrated that DPC/m displays significantly higher PDT efficacy *in vivo* than clinically used Photofrin (polyhematoporphyrin esters) in mice bearing human lung adenocarcinoma A549 cells. Furthermore,

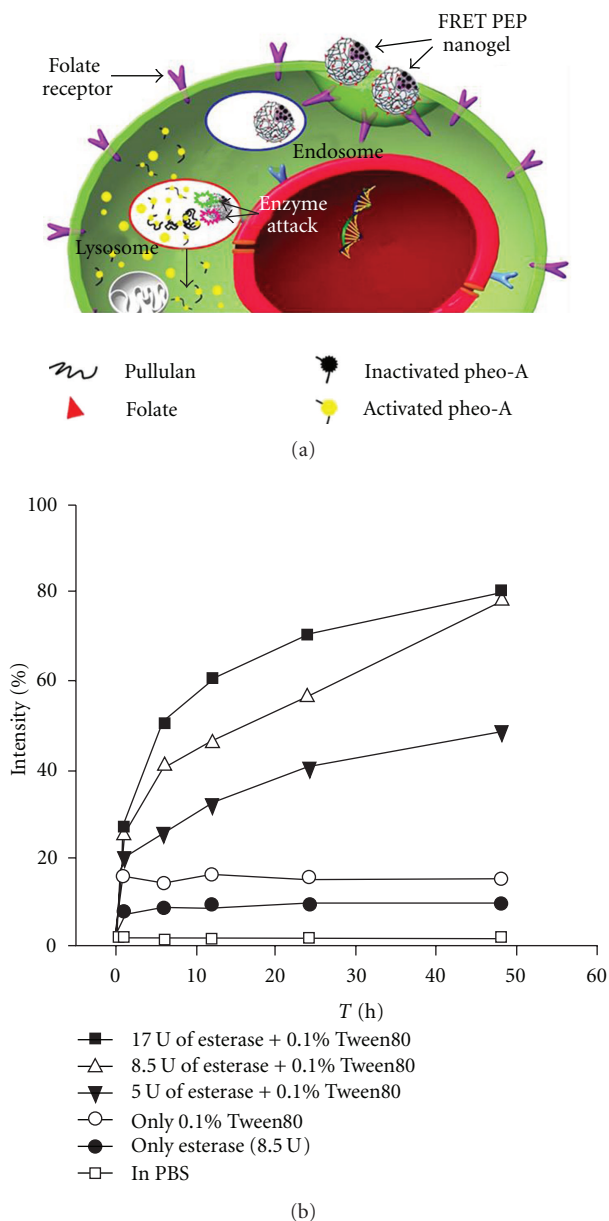


FIGURE 4: Conceptual image of the changes in photoactivity of polymeric carrier for PSs in cells (a). Enzymatic activation of polymeric carrier for PSs photoactivity. (b) Esterase effect according to time and concentration [12].

DPC/m-treated mice did not show skin phototoxicity, which was also observed in the PHE-treated mice, under the tested conditions. These results strongly suggest the usefulness of DPC/m in clinical PDT. These systems are an attempt in PDT to enhance the tumor-specificity of PSs.

To date, a variety of polymeric carriers, including polymer-PS conjugates [26, 27], PS-loaded nanocarriers [15], long-circulating liposomes [28], and polymeric micelles [29–33], have been developed due to their passive targeting properties, which increase tumor-selective accumulation due to enhanced microvascular permeability via impaired lymphatic drainage in tumor tissue, a phenomenon which

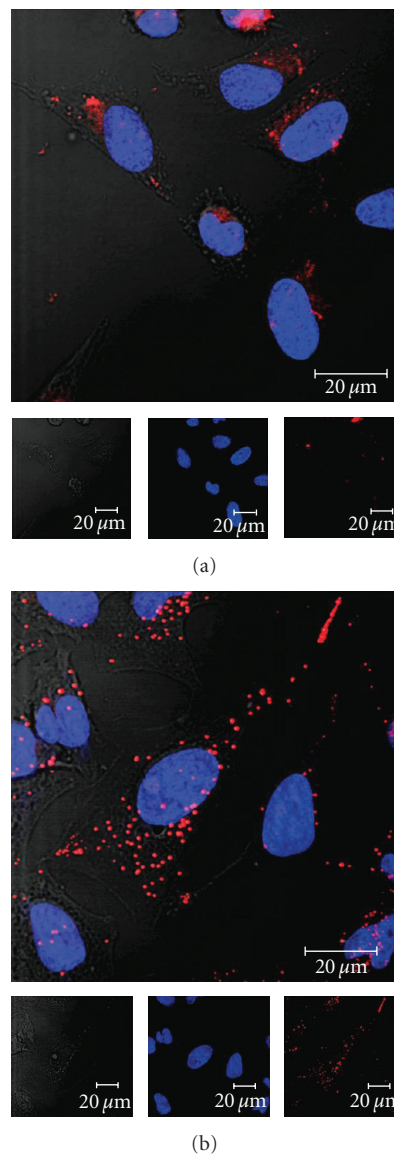


FIGURE 5: Confocal microscopic images of fixed HeLa cells incubated with polymeric carrier for PSs (b) or free PSs (a) for 6 h [13].

Maeda et al. termed the enhanced permeability and retention (EPR) effect [34–36].

4. Polymeric Photosensitizer from Conjugation between Biocompatible Polymer and PSs

Conjugation technology was employed to improve the low tumor specificity of PSs. The method to conjugate a target specific ligand such as folate to PSs (Figure 3) operates by slightly increasing target specificity toward the tumor site [37]. However, different from expectations, the conjugates create new interactions between the molecules, due to high hydrophobicity or π - π stacking, which results in low stability. On the other hand, to improve the poor water solubility of PSs, simple substitutions with hydrophilic groups (carboxyl, sulfate groups) were studied. Unfortunately, this study led

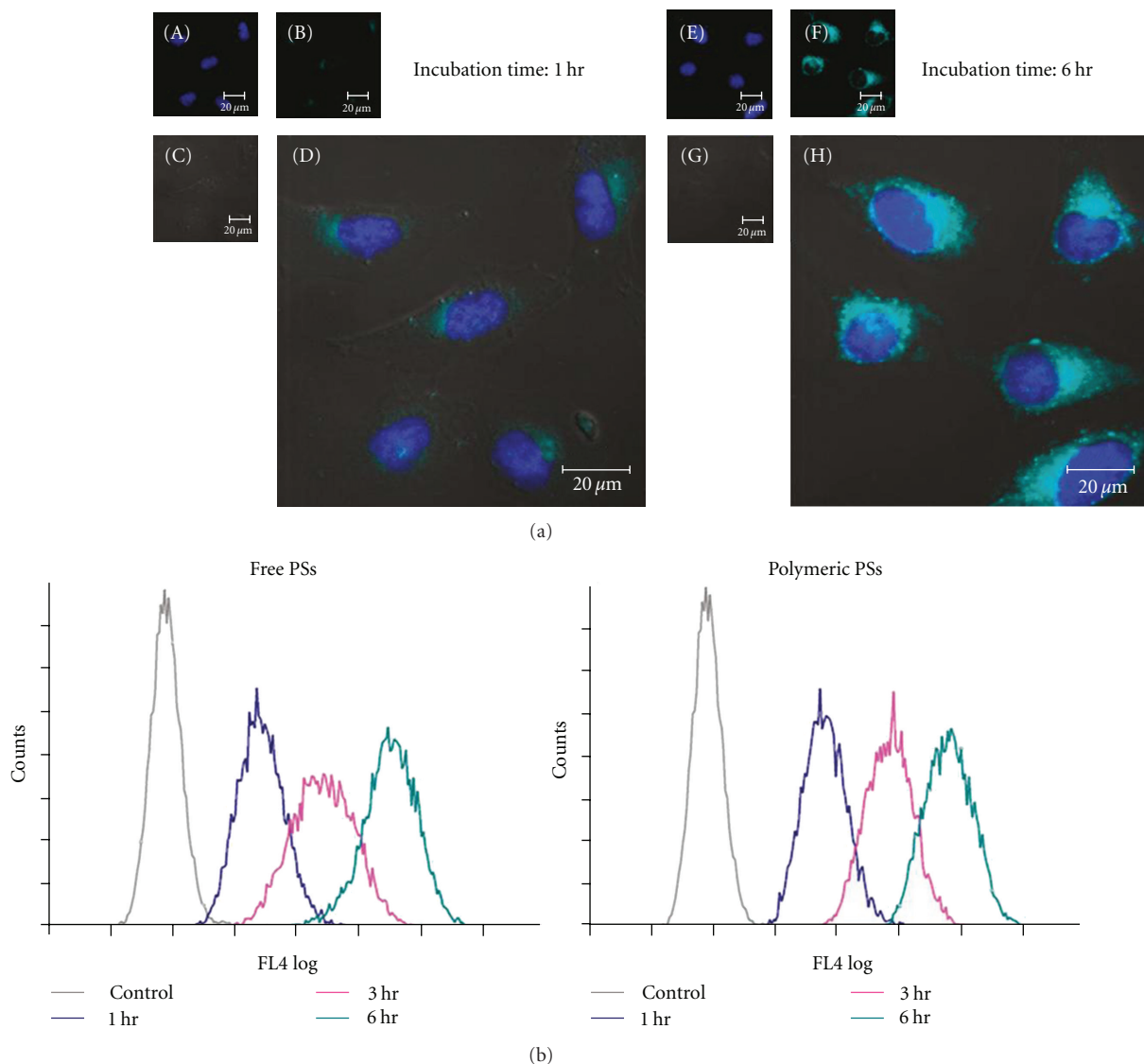


FIGURE 6: (a) Confocal laser scanning microscopic image of cellular internalization of CSA-based polymeric PSs in HeLa cells with incubation times of 1 and 6 h, (b) fluorescence-activated cell sorting (FACS) data of HeLa cells treated with (left) free Ce6 or (right) Ac-CS/Ce6 3 for 1 (blue), 3 (purple), and 6 h (green) [39].

to quick clearance of PSs from the body, resulting in an increased injection dose. Indeed, Laserphyrin chlorin derivative substituted with carboxyl group requires a six-times higher dose than that of porphyrin [38]. Therefore, polymeric PSs composed of conjugate of biocompatible polymer and PS have been investigated to improve water solubility and tumor targeting via EPR. Polymeric PSs may also provide easy purification by using precipitation and dialysis methods.

PSs are characterized by high solubility in aqueous solution, slow clearance from the body, and great specificity for tumors via the EPR effect. In particular, carriers show a self-quenching effect for controlling PS phototoxicity in the circulation, suppressing it via fluorescence resonance energy transfer (FRET) effect until they reach the target site, at which point the suppression can be rapidly reversed by the environmental conditions such as the enzyme [11–13, 39] and pH [16].

The enzymatically triggered photoactivity of polymeric PSs for tumor targeting was achieved by two methods based on the location of the enzyme, either extracellular or intracellular.

First, we reported the enzymatically triggered photoactivity of polymeric PSs by enzyme present in the cellular compartments. The concept of the system is shown in Figure 4(a). The system requires a ligand to uptake into the cell. Our group reported this system using pullulan/folate conjugate since folate receptor is overexpressed in tumor cells [40–43]. The conjugate did not show photoactivity during blood circulation due to self-quenching of PSs (FRET effect). However, when the conjugate was internalized in the cancer cells via receptor-mediated endocytosis, photoactivity was restored due to loss of the FRET effect by enzymatic attack within cellular compartments such as lysosomes. As shown in Figure 4(b), when the esterase was treated with surfactant

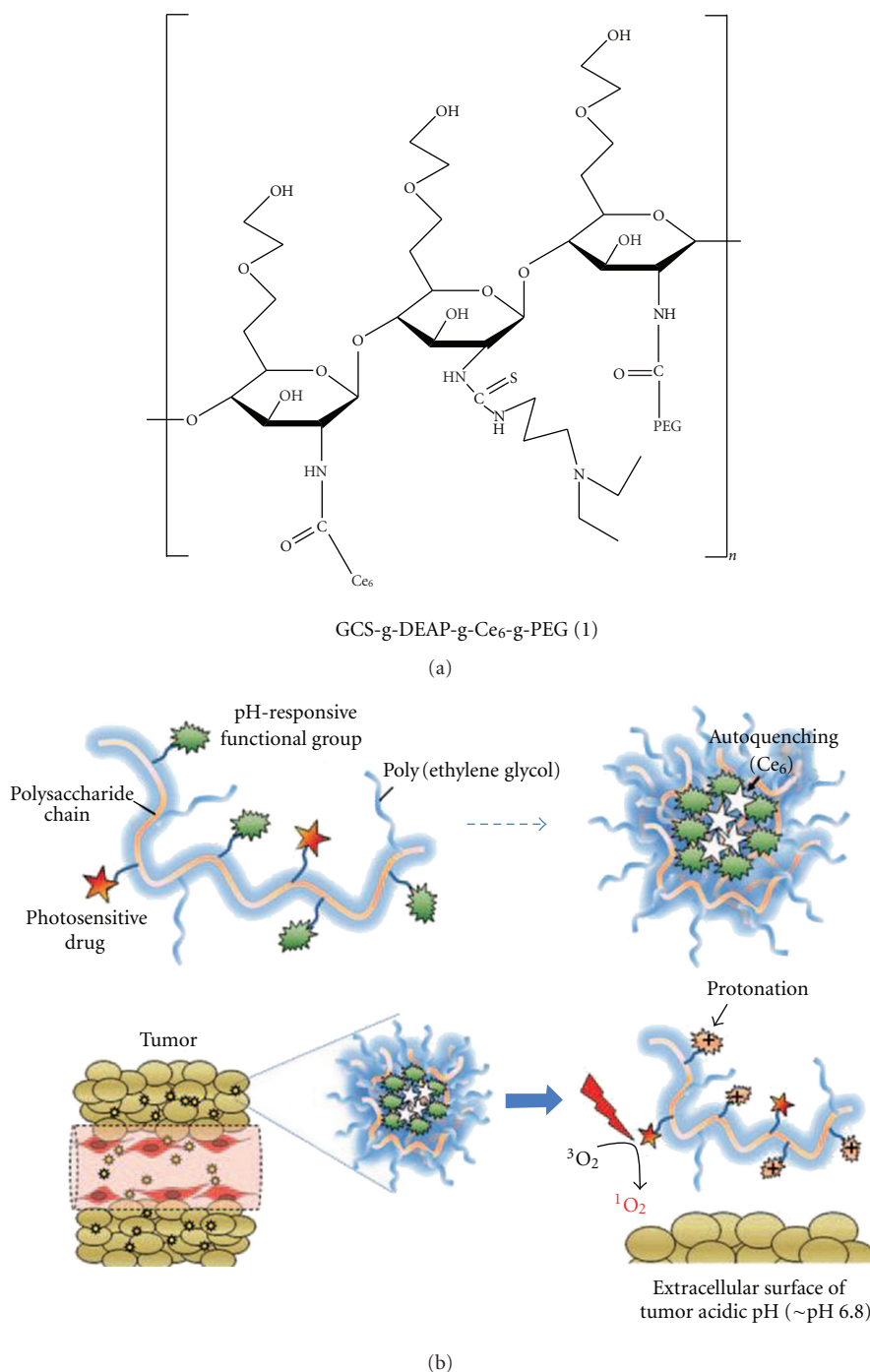


FIGURE 7: (a) Chemical structure of pH-sensitive polymeric carrier for PSs. (b) Schematic concept for a proposed polymeric carrier for PSs [16].

(0.1% Tween 80), polymeric PSs fluorescence dramatically increased to almost 80% of that of free PSs in organic solvent (DMSO or DMF). The intensity increased in proportion to the enzyme concentration, indicating that fluorescence was recovered by the enzymatic cleavage of the ester bond between pullulan and PSs. This suggests that as the polymeric PS is conjugated with the target ligand, it is easily internalized into the target cell. The property is very important to the accumulation of polymeric PSs at tumor site. Polymeric PSs

entrapped at the tumor site via the EPR effect prevent the accumulation of other polymeric PSs at the site by blocking narrow blood vessels. Thus, entrapped polymeric PSs are rapidly internalized into the tumor cells to enhance their accumulation rate.

Our group reported polymeric PSs produced by conjugation of PSs with polymer possessing a target such as hyaluronic acid (HA) and chondroitin sulfate (CS) [13, 39]. HA is a natural polymer common in the human body.

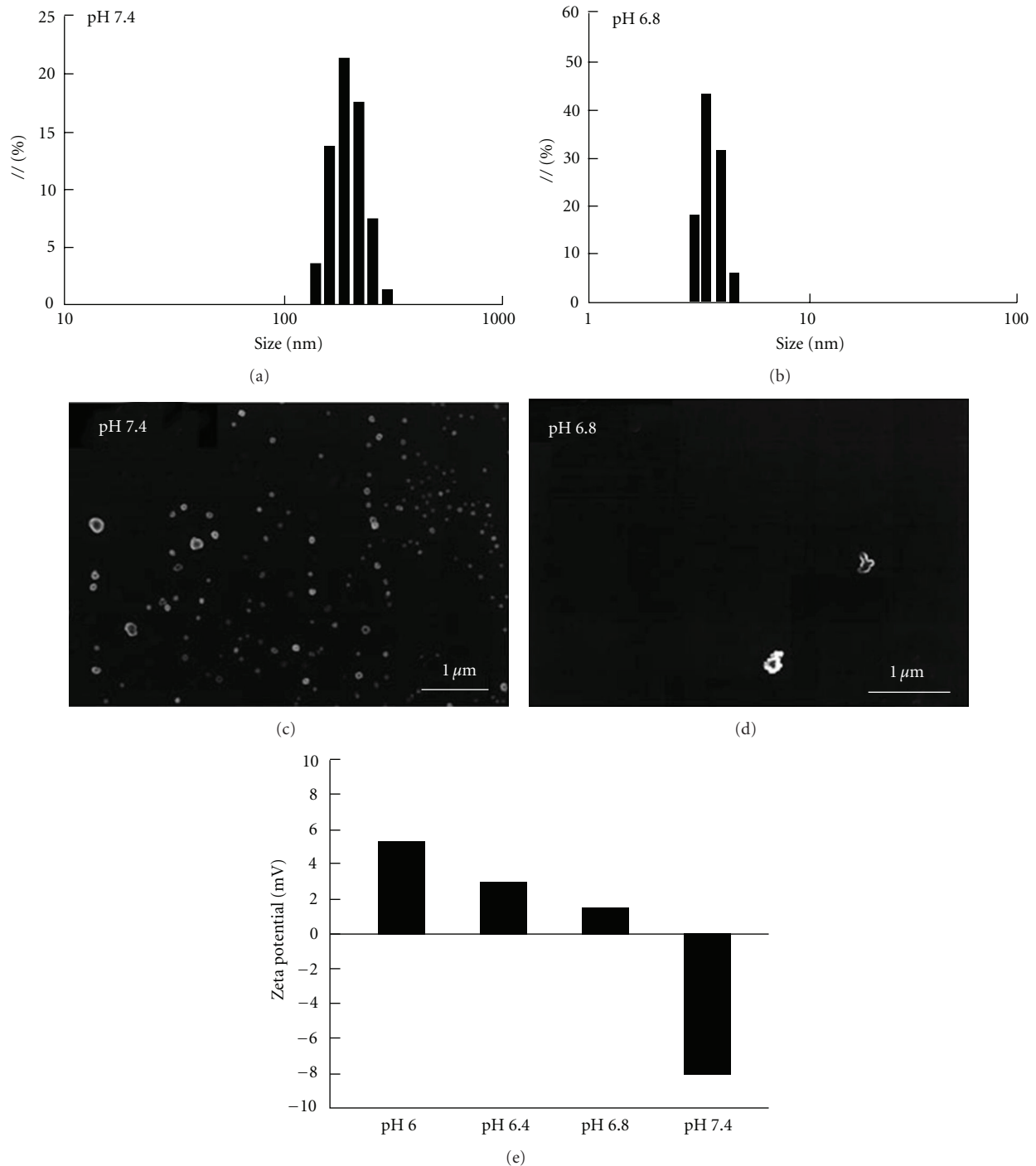


FIGURE 8: Characteristics of the polymeric carrier-PSs conjugate. Particle-size distribution of polymeric PSs (0.1 mgmL^{-1}) at (a) pH 7.4 (PBS 150 mM) and (b) pH 6.8 (PBS 150 mM) by Zetasizer. Field-emission scanning electron microscopic (FE/SEM) images of polymeric PSs at pH 7.4 (c) and pH 6.8 (d). (e) Zeta-potential change for polymeric PSs (0.1 mgmL^{-1} , pH 7.4–6.0, PBS 150 mM) at different pH values [16].

It interacts with CD44 receptor, which is overexpressed in specific tumor cells [13, 44–46]. HA was acetylated prior to being dissolved in organic solvent and then conjugated with different amounts of PSs, resulting in the formulation of self-organizing polymeric PSs in aqueous solutions. The polymeric PS obtained was below 200 nm in size with a monodisperse size distribution. It was rapidly internalized

into HeLa cells via an HA-induced endocytosis mechanism, a process that was blocked by the application of excess HA polymer (Figure 5). The results of the study indicate that HA-based polymeric PSs can potentially be applied in PDT. More recently, acetylated-chondroitin sulfate (CSA)/PS conjugates were synthesized via the formation of an ester linkage between CSA and PSs [39]. These conjugates in

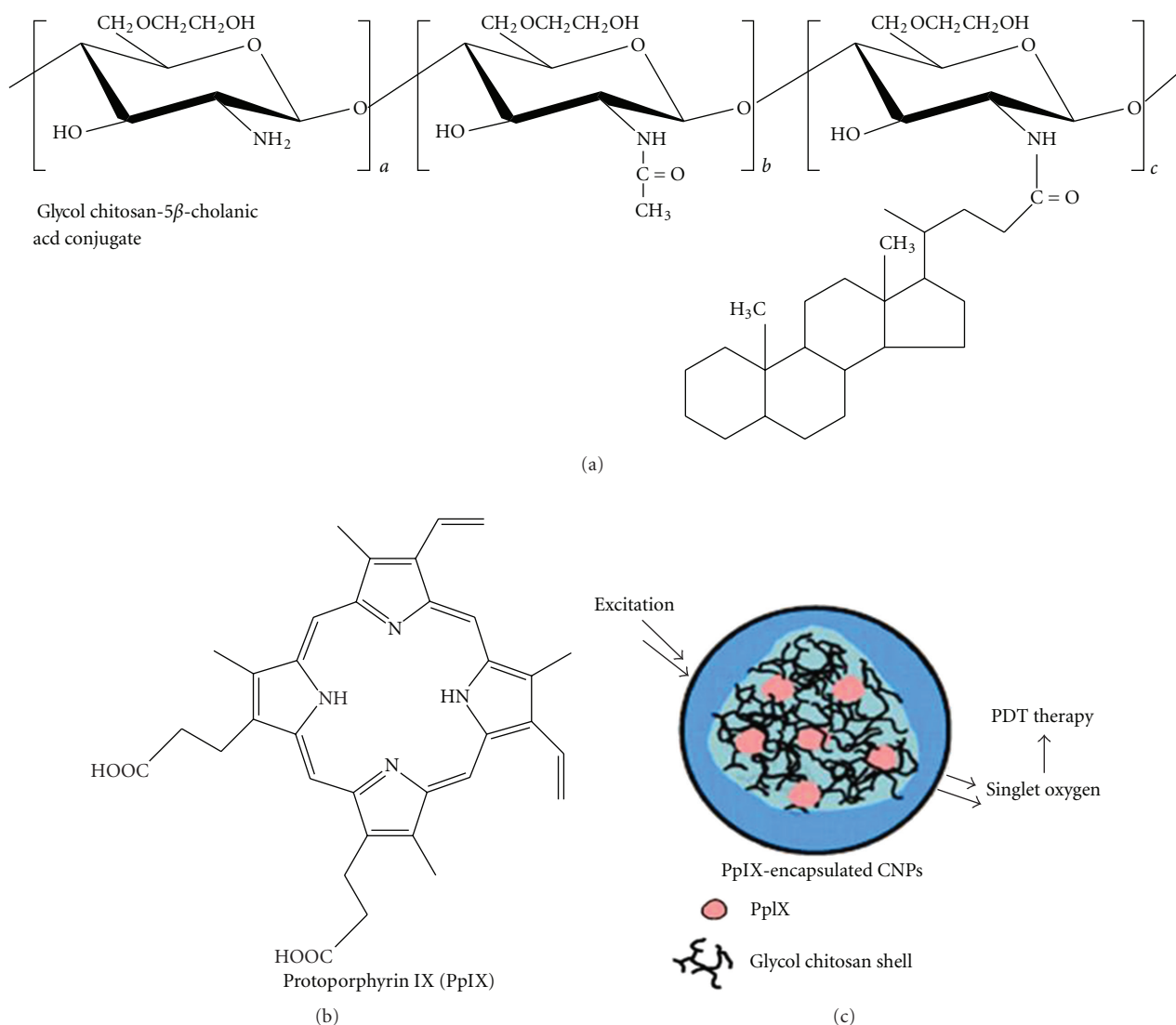


FIGURE 9: Chemical structure of glycol chitosan-5 β -cholanic acid conjugate and schematic representation of photosensitizer-encapsulated chitosan-based nanoparticles for PDT [15].

a HeLa cell culture system displayed rapid cellular uptake without any other ligands (Figure 6(a)) and fluorescence-activated cell sorting (FACS) analysis shows same result (Figure 6(b)). From these results, we suggest that this system may be instrumental in the design of new photodynamic therapies aiming to minimize phototoxicity.

Recently, polymeric PS with pH-triggered photoactivity was reported [26]. The system exploited the difference in extracellular pH between tumor and normal tissues (Figure 7). The system is composed of glycol chitosan (GCS) and PEG blocks for the hydrophilic outer shell and 3-diethylaminopropyl isothiocyanate (DEAP, pH sensitive material) and PS blocks for the hydrophobic inner core. In particular, incorporation of a PEG block may improve the stability of the drug conjugate in serum as well as its penetration into tumor vasculature [27]. Upon encountering the tumor environment, the polymeric carrier-PS conjugate undergoes conformational changes into an uncoiled structure. This

unique trait of polymeric PSs was confirmed experimentally (Figures 8(a)–8(d)). The magnitude of the particle-size changes for the polymeric PSs was large between pH 7.4 and 6.8; that is, the particle was 150 nm in diameter at pH 7.4 and 3.4 nm at pH 6.8. Figure 8(c) shows that polymeric PS was almost spherical in shape at pH 7.4. However, it became disentangled at pH 6.8, although very few aggregates were observed in this case (Figure 8(d)). Moreover, the zeta potential of polymeric PSs changed from -8.0 mV to $+1.3$ mV as the pH of the solution decreased from pH 7.4 to 6.8; the negative value originated from the PEG block at pH 7.4 and was offset by the protonation of the DEAP block at pH 6.8 (Figure 8(e)). It is known that the extracellular pH value in most clinical tumors is more acidic (pH, 6.5–7.0) than in normal tissues (ca. pH 7.4) [47, 48]. The different response of polymeric PSs at pH 7.4 (normal tissue pH) and at pH 6.8 (pH in tumors) presents a new route for the functionalization of photosensitizing drug conjugates.

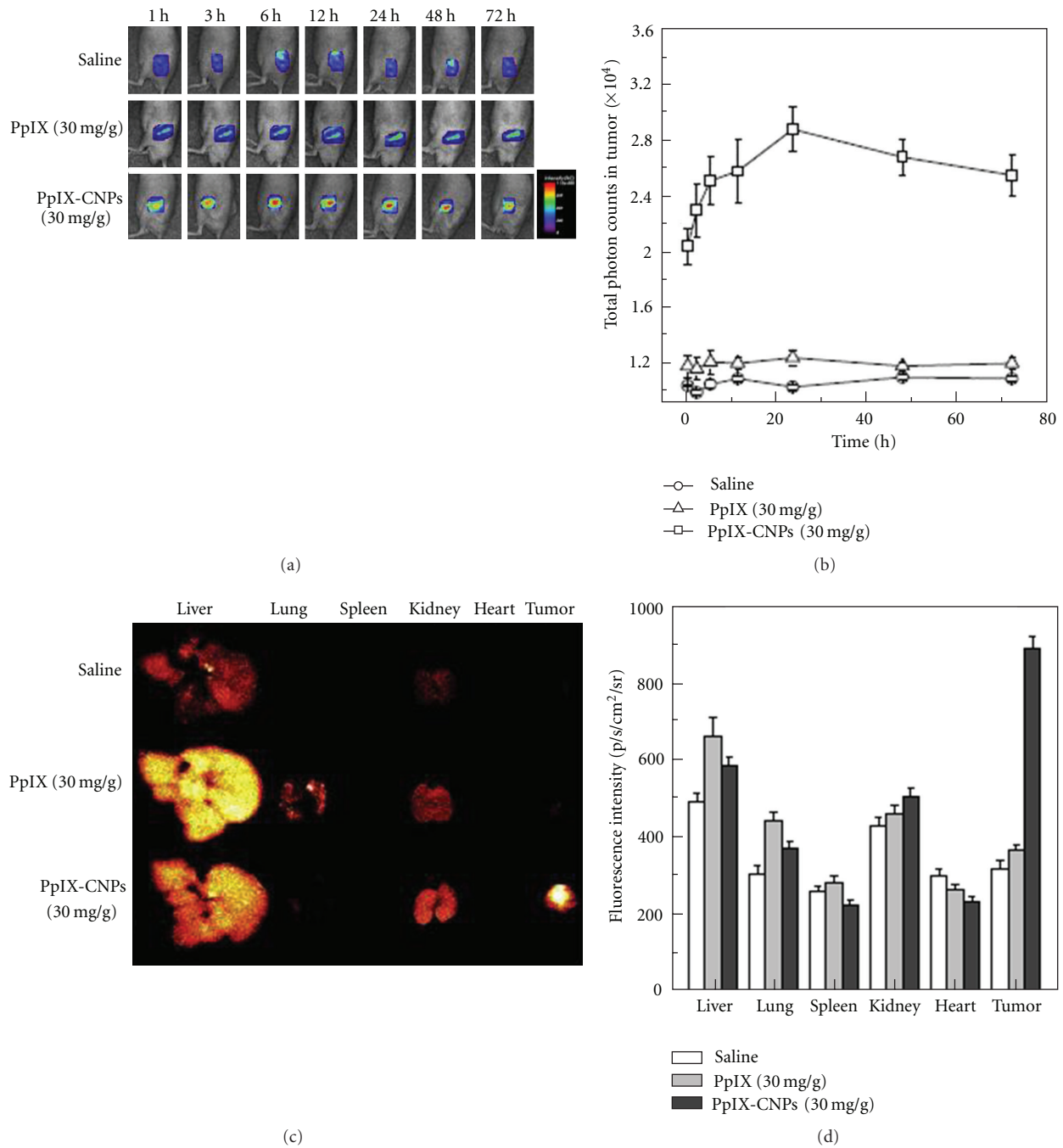


FIGURE 10: *In vivo* advantage of noninvasive fluorescence imaging tumor specificity compared to free PpIX and PpIX-polymeric nanocarriers [15].

5. Physical Loaded PSs in Nanocarriers

On the other hand, various nanocarriers with biodegradable and biocompatible polymers have been investigated for delivery of PSs. PSs are readily loaded in a nanocarrier by hydrophobic interactions between the hydrophobic moieties in the polymer and PSs. Hydrophobically modified glycol chitosan nanocarrier loaded with protoporphyrin IX (PpIX), which is a porphyrin-based PS (Figure 9) [15], has been reported. The nanocarrier range from 200~300 nm shows

a much better accumulation rate at the tumor site than free PSs *in vivo*. In a previous study in SCC7 tumor-bearing mice, PpIX-glycol chitosan nanocarrier exhibited enhanced tumor specificity and increased therapeutic efficacy compared to free PpIX (Figure 10). Unfortunately, the system did not show controllable photoactivity via self-quenching, which can minimize damage against normal tissue and blood cells.

PSs were also loaded in nanocarriers via an ionic complex (Figure 11) [17]. In that study, the complex decreased the hydrophobicity of PSs, which produced a nanocarrier

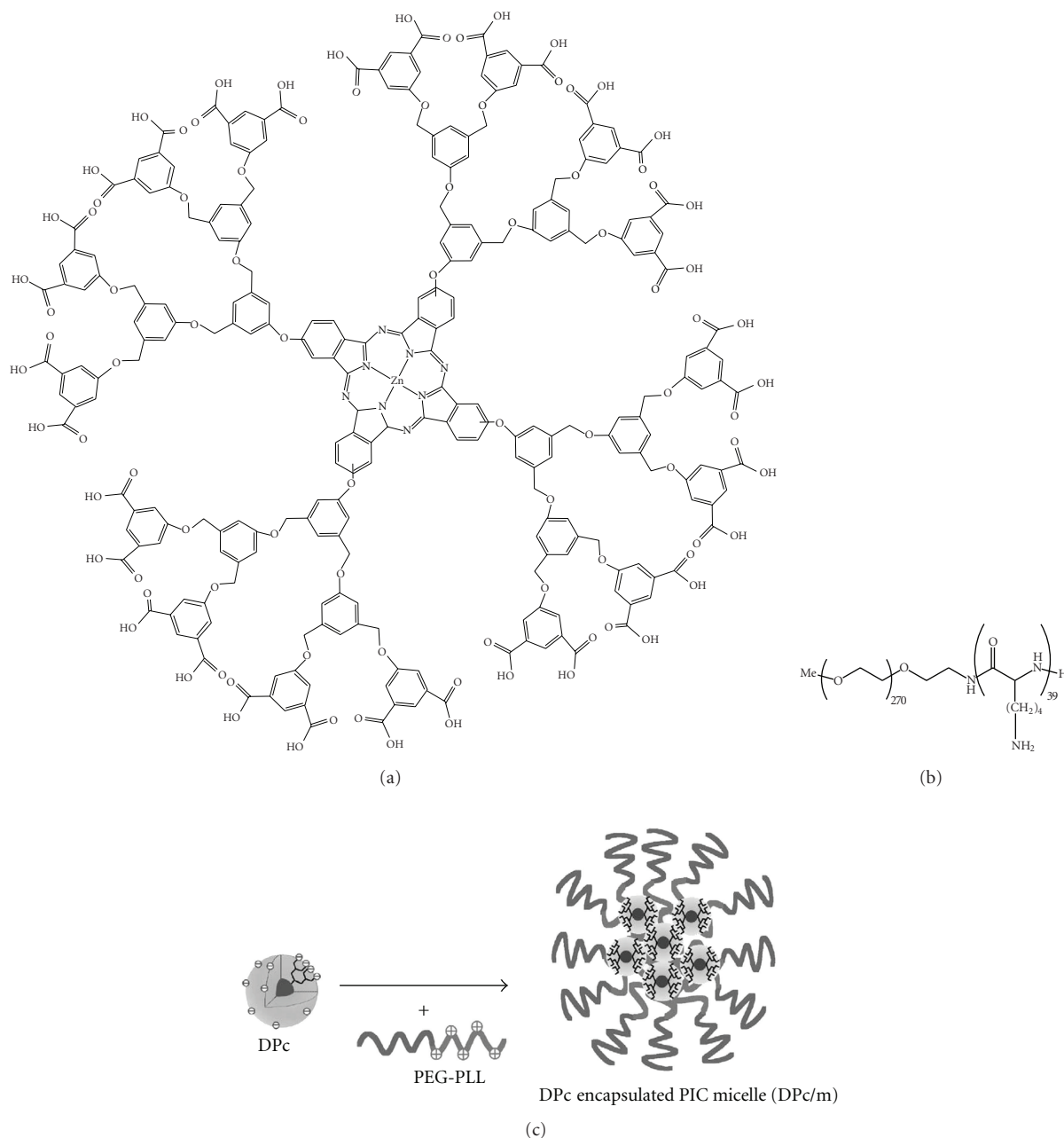


FIGURE 11: Chemical structures of anionic dendrimer PSs (a) and poly(ethylene glycol)-poly(L-lysine) (PEG-PLL) block copolymer (b). Dendrimer PSs-encapsulated ionic complex micelle was formed by mixing PSs and PEG-PLL at a charge stoichiometric ratio (c) [17].

composed of a core with sufficient photoactivity and an outer shell with dendrimer form. The dendrimer form of PSs becomes available to ionic complex using PEG, which contains a cationic charge. PEG is well known for its strong hydrophilic groups, which increase the retention time in the blood circulation by exposure on the surface of the nanocarrier [49–52]. Further, this system increases the tumor target specificity by binding with antibody or a target moiety [34] and does not require control of drug release, which is always hurdle in drug delivery system. However, the system has side-effects associated with PDT such as skin toxicity.

Recently, gold nanoparticles have been developed (Figure 12) [14], this gold nanorod-PS complex was developed for noninvasive near-infrared fluorescence imaging and cancer therapy. A previous study showed that fluorescence emission and singlet oxygen generation by AlPcS4 (photosensitizer, Al(III) phthalocyanine chloride tetrasulfonic acid) were quenched after complex formation with GNRs (gold nanorods); 4-fold greater intracellular uptake and better *in vitro* phototoxicity were observed in GNR-AlPcS4-treated cells than in free AlPcS4-treated cells, and after intravenous injection of the GNR-AlPcS4 complex, tumor sites were clearly identified in near-infrared fluorescence images as

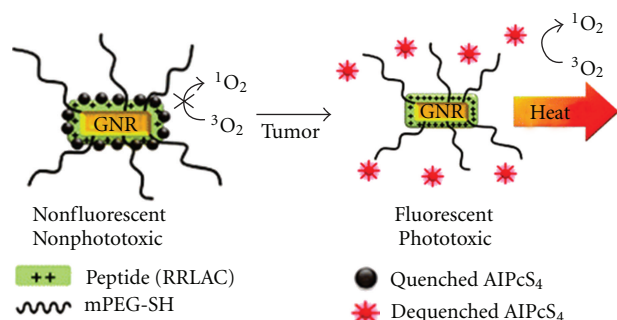


FIGURE 12: Polymeric carrier for thermo- and photodynamic therapy [14].

early as 1 h after injection. The tumor-to-background ratio increased over time and reached 3.7 at 24 h; tumor growth was reduced by 79% with photodynamic therapy (PDT) alone and by 95% with dual photothermal therapy (PTT) [53] and PDT. Based on these results, novel multifunctional nanomedicine may be useful for near-infrared fluorescence imaging and PTT/PDT in various cancers. Moreover, during circulation in the blood, these polymeric nanocarrier system can be completely suppressed until it reaches the target site, where the suppression can be rapidly reversed by decomplex. And, this system currently attempts the introduction of targeting ligands at the end of the PEG chain, which may further improve tumor targeting efficiency of GNR-PS complexes.

6. Conclusion

As suggested previously, many studies on PDT based on polymeric carriers such as polymeric PSs and nanocarrier loaded with PSs have been carried out in order to improve the poor water solubility and target specificity of PSs. For this purpose, polymeric carriers increase water solubility and targeting ratio. In particular, polymeric PSs composed of a conjugate of polymer and PS display controllable photoactivity between the target site and normal tissue via the FRET effect. And, this property provides the basis for various applications in the fields of diagnostics and biosensors. Although there are still tasks that must be solved, such as a more specific targeting rate, high photo-adsorption efficiency, and easy light source delivery to tumor sites, the development of polymeric carriers can dramatically increase the potential of PDT in the diagnosis and treatment of diseases.

Acknowledgments

This paper was financially supported by the Fundamental R&D Program for Core Technology of Materials, Republic of Korea, the Gyeonggi Regional Research Center (GRRC), the Korea Ministry of Education, Science and Technology through Strategic Research (2011-0028726), the Next-Generation BioGreen 21 Program (PJ0071862011), Rural Development Administration, Republic of Korea, and Hi

Seoul Science/Humanities Fellowship from Seoul Scholarship Foundation.

References

- [1] C. Raab, "Über die Wirkung fluoreszierender Stoffe auf Infusoria," *Zeitschrift für Biologie*, vol. 39, pp. 524–526, 1900.
- [2] D. E. Dolmans and R. K. J. D. Fukumura, "Photodynamic therapy for cancer," *Nature Reviews Cancer*, vol. 3, no. 5, pp. 380–387, 2003.
- [3] T. J. Dougherty, C. J. Gomer, B. W. Henderson et al., "Photodynamic therapy," *Journal of the National Cancer Institute*, vol. 90, no. 12, pp. 889–905, 1998.
- [4] N. Nishiyama, Y. Morimoto, W. D. Jang, and K. Kataoka, "Design and development of dendrimer photosensitizer-incorporated polymeric micelles for enhanced photodynamic therapy," *Advanced Drug Delivery Reviews*, vol. 61, no. 4, pp. 327–338, 2009.
- [5] I. J. MacDonald and T. J. Dougherty, "Basic principles of photodynamic therapy," *Journal of Porphyrins and Phthalocyanines*, vol. 5, no. 2, pp. 105–129, 2001.
- [6] A. M. R. Fisher, A. L. Murphree, and C. J. Gomer, "Clinical and preclinical photodynamic therapy," *Lasers in Surgery and Medicine*, vol. 17, no. 1, pp. 2–31, 1995.
- [7] J. S. Nelson, W. G. Roberts, and M. W. Berns, "In vivo studies on the utilization of mono-L-aspartyl chlorin (NPe6) for photodynamic therapy," *Cancer Research*, vol. 47, no. 17, pp. 4681–4685, 1987.
- [8] C. J. Gomer and A. Ferrario, "Tissue distribution and photosensitizing properties of mono-L-aspartyl chlorin e6 in a mouse tumor model," *Cancer Research*, vol. 50, no. 13, pp. 3985–3990, 1990.
- [9] B. W. Henderson, D. A. Bellnier, W. R. Greco et al., "An in vivo quantitative structure-activity relationship for a congeneric series of pyropheophorbide derivatives as photosensitizers for photodynamic therapy," *Cancer Research*, vol. 57, no. 18, pp. 4000–4007, 1997.
- [10] P. Morliere, J. C. Mazière, R. Santus et al., "Tolyporphin: a natural product from cyanobacteria with potent photosensitizing activity against tumor cells in vitro and in vivo," *Cancer Research*, vol. 58, no. 16, pp. 3571–3578, 1998.
- [11] B. C. Bae, F. Li, D. Ling, and K. Na, "Self-organized nanogel from pullulan/pheophorbide-A conjugate as a macromolecular photodynamic agent," *Journal of Porphyrins and Phthalocyanines*, vol. 14, no. 10, pp. 851–858, 2010.
- [12] B. C. Bae and K. Na, "Self-quenching polysaccharide-based nanogels of pullulan/folate-photosensitizer conjugates for photodynamic therapy," *Biomaterials*, vol. 31, no. 24, pp. 6325–6335, 2010.
- [13] F. Li, B. C. Bae, and K. Na, "Acetylated hyaluronic acid/photosensitizer conjugate for the preparation of nanogels with controllable phototoxicity: synthesis, characterization, autophotoquenching properties, and in vitro phototoxicity against hela cells," *Bioconjugate Chemistry*, vol. 21, no. 7, pp. 1312–1320, 2010.
- [14] B. Jang, J. Y. Park, C. H. Tung, I. H. Kim, and Y. Choi, "Gold nanorod-photosensitizer complex for near-infrared fluorescence imaging and photodynamic/photothermal therapy in vivo," *ACS Nano*, vol. 5, no. 2, pp. 1086–1094, 2011.
- [15] S. J. Lee, K. Park, Y. K. Oh et al., "Tumor specificity and therapeutic efficacy of photosensitizer-encapsulated glycol chitosan-based nanoparticles in tumor-bearing mice," *Biomaterials*, vol. 30, no. 15, pp. 2929–2939, 2009.

- [16] S. Y. Park, H. J. Baik, Y. T. Oh, K. T. Oh, Y. S. Youn, and E. S. Lee, "A smart polysaccharide/drug conjugate for photodynamic therapy," *Angewandte Chemie*, vol. 50, no. 7, pp. 1644–1647, 2011.
- [17] N. Nishiyama, Y. Nakagishi, Y. Morimoto et al., "Enhanced photodynamic cancer treatment by supramolecular nanocarriers charged with dendrimer phthalocyanine," *Journal of Controlled Release*, vol. 133, no. 3, pp. 245–251, 2009.
- [18] K. Masumoto, I. Yamada, H. Tanaka, Y. Fujise, and K. Hashimoto, "Tissue distribution of a new photosensitizer ATX-S10Na(II) and effect of a diode laser (670 nm) in photodynamic therapy," *Lasers in Medical Science*, vol. 18, no. 3, pp. 134–138, 2003.
- [19] K. Plaetzer, B. Krammer, J. Berlanda, F. Berr, and T. Kiesslich, "Photophysics and photochemistry of photodynamic therapy: fundamental aspects," *Lasers in Medical Science*, vol. 24, no. 2, pp. 259–268, 2009.
- [20] J. P. Rovers, A. E. Saarnak, A. Molina, J. J. Schuitmaker, H. J. C. M. Sterenborg, and O. T. Terpstra, "Effective treatment of liver metastases with photodynamic therapy, using the second-generation photosensitizer meta-tetra(hydroxyphenyl)chlorin (mTHPC), in a rat model," *British Journal of Cancer*, vol. 81, no. 4, pp. 600–608, 1999.
- [21] J. Usuda, H. Kato, T. Okunaka et al., "Photodynamic therapy (PDT) for lung cancers," *Journal of Thoracic Oncology*, vol. 1, no. 5, pp. 489–493, 2006.
- [22] I. L. Medintz, A. R. Clapp, H. Mattoussi, E. R. Goldman, B. Fisher, and J. M. Mauro, "Self-assembled nanoscale biosensors based on quantum dot FRET donors," *Nature Materials*, vol. 2, no. 9, pp. 630–638, 2003.
- [23] A. Orenstein, G. Kostenich, L. Roitman et al., "A comparative study of tissue distribution and photodynamic therapy selectivity of chlorin e6, Photofrin II and ALA-induced protoporphyrin IX in a colon carcinoma model," *British Journal of Cancer*, vol. 73, no. 8, pp. 937–944, 1996.
- [24] N. L. Krinick, Y. Sun, D. A. Joyner et al., "Polymer-bound meso-chlorin e6 for PDT," in *Proceedings of the Optical Methods for Tumor Treatment and Detection: Mechanisms and Techniques in Photodynamic Therapy*, pp. 142–154, Los Angeles, Calif, USA, January 1992.
- [25] N. Nishiyama, H. R. Stapert, G. D. Zhang et al., "Light-harvesting ionic dendrimer porphyrins as new photosensitizers for photodynamic therapy," *Bioconjugate Chemistry*, vol. 14, no. 1, pp. 58–66, 2003.
- [26] J. G. Shiah, Y. Sun, C. M. Peterson, R. C. Straight, and J. Kopeček, "Antitumor activity of N-(2-hydroxypropyl)methacrylamide copolymer-mesochlorin e6 and Adriamycin conjugates in combination treatments," *Clinical Cancer Research*, vol. 6, no. 3, pp. 1008–1015, 2000.
- [27] M. R. Hamblin, J. L. Miller, I. Rizvi, B. Ortel, E. V. Maytin, and T. Hasan, "Pegylation of a chlorine6 polymer conjugate increases tumor targeting of photosensitizer," *Cancer Research*, vol. 61, no. 19, pp. 7155–7162, 2001.
- [28] A. S. L. Derycke and P. A. M. de Witte, "Liposomes for photodynamic therapy," *Advanced Drug Delivery Reviews*, vol. 56, no. 1, pp. 17–30, 2004.
- [29] C. L. Peng, M. J. Shieh, M. H. Tsai, C. C. Chang, and P. S. Lai, "Self-assembled star-shaped chlorin-core poly(ϵ -caprolactone)-poly(ethylene glycol) diblock copolymer micelles for dual chemo-photodynamic therapies," *Biomaterials*, vol. 29, no. 26, pp. 3599–3608, 2008.
- [30] B. Li, E. H. Moriyama, F. Li, M. T. Jarvi, C. Allen, and B. C. Wilson, "Diblock copolymer micelles deliver hydrophobic protoporphyrin IX for photodynamic therapy," *Photochemistry and Photobiology*, vol. 83, no. 6, pp. 1505–1512, 2007.
- [31] L. O. Cinteza, T. Y. Ohulchanskyy, Y. Sahoo, E. J. Bergey, R. K. Pandey, and P. N. Prasad, "Diacyllipid micelle-based nanocarrier for magnetically guided delivery of drugs in photodynamic therapy," *Molecular Pharmaceutics*, vol. 3, no. 4, pp. 415–423, 2006.
- [32] D. le Garrec, J. Taillefer, J. E. van Lier, V. Lenaerts, and J. C. Leroux, "Optimizing pH-responsive polymeric micelles for drug delivery in a cancer photodynamic therapy model," *Journal of Drug Targeting*, vol. 10, no. 5, pp. 429–437, 2002.
- [33] G. D. Zhang, A. Harada, N. Nishiyama et al., "Polyion complex micelles entrapping cationic dendrimer porphyrin: effective photosensitizer for photodynamic therapy of cancer," *Journal of Controlled Release*, vol. 93, no. 2, pp. 141–150, 2003.
- [34] H. Maeda, "Polymer conjugated macromolecular drugs for tumor-specific targeting," in *Polymeric Site-Specific Pharmacotherapy*, pp. 95–116, John Wiley & Sons Ltd, New York, NY, USA, 1994.
- [35] Y. Matsumura and H. Maeda, "A new concept for macromolecular therapeutics in cancer chemotherapy: mechanism of tumoritropic accumulation of proteins and the antitumor agent smancs," *Cancer Research*, vol. 46, no. 12, part 1, pp. 6387–6392, 1986.
- [36] R. Duncan and Y. Sat, "Tumor targeting by enhanced permeability and retention (EPR) effect," *Annals of Oncology*, vol. 9, supplement 2, p. 39, 1998.
- [37] J. Gravier, R. Schneider, C. Frochet et al., "Improvement of meta-tetra(hydroxyphenyl)chlorin-like photosensitizer selectivity with folate-based targeted delivery. Synthesis and in vivo delivery studies," *Journal of Medicinal Chemistry*, vol. 51, no. 13, pp. 3867–3877, 2008.
- [38] A. E. O'Connor, W. M. Gallagher, and A. T. Byrne, "Porphyrin and nonporphyrin photosensitizers in oncology: preclinical and clinical advances in photodynamic therapy," *Photochemistry and Photobiology*, vol. 85, no. 5, pp. 1053–1074, 2009.
- [39] F. Li and K. Na, "Self-assembled chlorin e6 conjugated chondroitin sulfate nanodrug for photodynamic therapy," *Biomacromolecules*, vol. 12, no. 5, pp. 1724–1730, 2011.
- [40] S. Kim, K. M. Park, J. Y. Ko et al., "Minimalism in fabrication of self-organized nanogels holding both anti-cancer drug and targeting moiety," *Colloids and Surfaces B*, vol. 63, no. 1, pp. 55–63, 2008.
- [41] J. Cummings and C. S. McArdle, "Studies on the in vivo disposition of adriamycin in human tumours which exhibit different responses to the drug," *British Journal of Cancer*, vol. 53, no. 6, pp. 835–838, 1986.
- [42] D. Goren, A. T. Horowitz, D. Tzemach, M. Tarshish, S. Zalipsky, and A. Gabizon, "Nuclear delivery of doxorubicin via folate-targeted liposomes with bypass of multidrug-resistance efflux pump," *Clinical Cancer Research*, vol. 6, no. 5, pp. 1949–1957, 2000.
- [43] S. D. Weitman, A. G. Weinberg, L. R. Coney, V. R. Zurawski, D. S. Jennings, and B. A. Kamen, "Cellular localization of the folate receptor: potential role in drug toxicity and folate homeostasis," *Cancer Research*, vol. 52, no. 23, pp. 6708–6711, 1992.
- [44] A. Aruffo, I. Stamenkovic, M. Melnick, C. B. Underhill, and B. Seed, "CD44 is the principal cell surface receptor for hyaluronate," *Cell*, vol. 61, no. 7, pp. 1303–1313, 1990.
- [45] M. Culty, H. A. Nguyen, and C. B. Underhill, "The hyaluronan receptor (CD44) participates in the uptake and degradation of hyaluronan," *Journal of Cell Biology*, vol. 116, no. 4, pp. 1055–1062, 1992.

- [46] C. Underhill, "CD44: the hyaluronan receptor," *Journal of Cell Science*, vol. 103, no. 2, pp. 293–298, 1992.
- [47] E. S. Lee, K. T. Oh, D. Kim, Y. S. Youn, and Y. H. Bae, "Tumor pH-responsive flower-like micelles of poly(L-lactic acid)-b-poly(ethylene glycol)-b-poly(L-histidine)," *Journal of Controlled Release*, vol. 123, no. 1, pp. 19–26, 2007.
- [48] E. S. Lee, K. Na, and Y. M. Bae, "Super pH-sensitive multifunctional polymeric micelle," *Nano Letters*, vol. 5, no. 2, pp. 325–329, 2005.
- [49] E. S. Lee, H. J. Shin, K. Na, and Y. H. Bae, "Poly(L-histidine)-PEG block copolymer micelles and pH-induced destabilization," *Journal of Controlled Release*, vol. 90, no. 3, pp. 363–374, 2003.
- [50] N. A. Peppas, K. B. Keys, M. Torres-Lugo, and A. M. Lowman, "Poly(ethylene glycol)-containing hydrogels in drug delivery," *Journal of Controlled Release*, vol. 62, no. 1-2, pp. 81–87, 1999.
- [51] K. Na, K. H. Lee, D. H. Lee, and Y. H. Bae, "Biodegradable thermo-sensitive nanoparticles from poly(L-lactic acid)/poly(ethylene glycol) alternating multi-block copolymer for potential anti-cancer drug carrier," *European Journal of Pharmaceutical Sciences*, vol. 27, no. 2-3, pp. 115–122, 2006.
- [52] J. M. Harris and R. B. Chess, "Effect of pegylation on pharmaceuticals," *Nature Reviews Drug Discovery*, vol. 2, no. 3, pp. 214–221, 2003.
- [53] I. H. El-Sayed, X. Huang, and M. A. El-Sayed, "Selective laser photo-thermal therapy of epithelial carcinoma using anti-EGFR antibody conjugated gold nanoparticles," *Cancer Letters*, vol. 239, no. 1, pp. 129–135, 2006.

Review Article

Nanophotonics for Molecular Diagnostics and Therapy Applications

João Conde,^{1,2} João Rosa,^{1,3} João C. Lima,³ and Pedro V. Baptista¹

¹ CIGMH, Departamento de Ciências da Vida, Faculdade de Ciências e Tecnologia, Universidade Nova de Lisboa, Campus de Caparica, 2829-516 Caparica, Portugal

² Instituto de Nanociencia de Aragón, Universidad de Zaragoza, Campus Río Ebro, Edificio I+D, Mariano Esquillor s/n, 50018 Zaragoza, Spain

³ REQUIMTE, Departamento de Química, Faculdade de Ciências e Tecnologia, Universidade Nova de Lisboa, Campus de Caparica, 2829-516 Caparica, Portugal

Correspondence should be addressed to Pedro V. Baptista, pmvb@fct.unl.pt

Received 15 June 2011; Accepted 10 July 2011

Academic Editor: Danuta Wrobel

Copyright © 2012 João Conde et al. This is an open access article distributed under the Creative Commons Attribution License, which permits unrestricted use, distribution, and reproduction in any medium, provided the original work is properly cited.

Light has always fascinated mankind and since the beginning of recorded history it has been both a subject of research and a tool for investigation of other phenomena. Today, with the advent of nanotechnology, the use of light has reached its own dimension where light-matter interactions take place at wavelength and subwavelength scales and where the physical/chemical nature of nanostructures controls the interactions. This is the field of nanophotonics which allows for the exploration and manipulation of light in and around nanostructures, single molecules, and molecular complexes. What is more is the use of nanophotonics in biomolecular interactions—nanobiophotonics—has prompted a plethora of molecular diagnostics and therapeutics making use of the remarkable nanoscale properties. In this paper, we shall focus on the uses of nanobiophotonics for molecular diagnostics involving specific sequence characterization of nucleic acids and for gene delivery systems of relevance for therapy strategies. The use of nanobiophotonics for the combined diagnostics/therapeutics (theranostics) will also be addressed, with particular focus on those systems enabling the development of safer, more efficient, and specific platforms. Finally, the translation of nanophotonics for theranostics into the clinical setting will be discussed.

1. Introduction

Nanophotonics deals with the interaction of light with matter at a nanometer scale, providing challenges for fundamental research and opportunities for new technologies, encompassing the study of new optical interactions, materials, fabrication techniques, and architectures, including the exploration of natural and synthetic, or artificially engineered, structures such as photonic crystals, holey fibers, quantum dots, subwavelength structures, and plasmonics [1, 2]. The use of photonic nanotechnologies in medicine is a rapidly emerging and potentially powerful approach for disease protection, detection, and treatment. The high speed of light manipulation and the remote nature of optical methods suggest that light may successfully connect diagnostics, treatment, and even the guidance of the treatment

in one theranostic procedure combination of therapeutics with diagnostics (including patient prescreening and therapy monitoring).

Limitations in medical practice are closely associated with the fact that diagnostics, therapy, and therapy guidance are three discrete and isolated stages. In order to overcome some of the sensitivity and specificity of current medicines, theranostics unites the three above stages in one single process, supporting early-stage diagnosis and treatment [3, 4]. Nowadays, there is an ever increasing need to enhance the capability of theranostics procedures where nanophotonics-based sensors may provide for the simultaneous detection of several gene-associated conditions and nanodevices utilizing light-guided and light-activated therapy with the ability to monitor real-time drug action (see Figure 1).

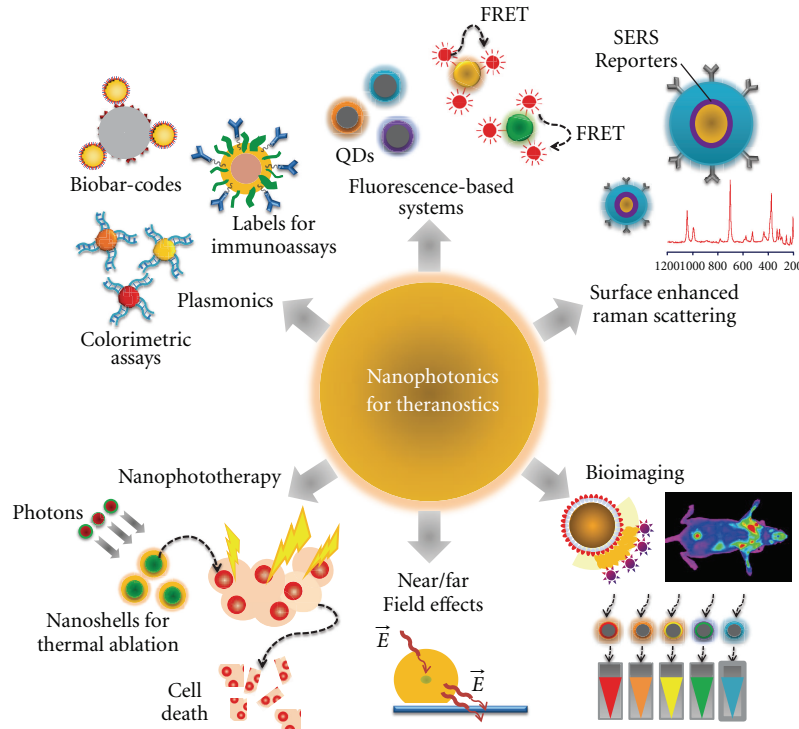


FIGURE 1: *Nanophotonics for theranostics*. Nanoparticles-based strategies can be used for biosensing using *plasmonic nanosensors*, such as metal nanoparticles functionalized with nucleic acid strand for colorimetric assays and biobar codes for protein detection or intense labels for immunoassays. Some nanoparticle systems can also be used for sensing by exploring a typical *FRET system* or can be surrounded with *Raman reporters* in order to provide *in vivo* detection and tumour targeting. In fact, NPs symbolize an important class of materials with unique features suitable for *biomedical imaging* applications such as increased sensitivity in detection and high quantum yields for fluorescence. Alternatively, NPs can survey *near/far field* enhancing qualities that hold promise for a bounty of novel applications in optics and photonics. Engineered NPs can also act as *phototherapeutic agents* that can be attached to specific targets for selective damage to cancer cells.

2. Nanophotonics For Diagnostics

2.1. Surface Plasmons on Nanoparticles and Surfaces. Surface plasmons are collective charge oscillations that occur at the interface between conductors and dielectrics. They can take various forms, ranging from freely propagating electron density waves along metal surfaces to localized electron oscillations on metal nanoparticles (NPs) [5, 6]. When light passes through a metal nanoparticle, it induces dipole moments that oscillate at the respective frequency of the incident wave, consequently dispersing secondary radiation in all directions. This collective oscillation of the free conduction electrons is called localized surface plasmon resonance (LSPR). Light on NP induces the conduction electrons to oscillate collectively with a resonant frequency that depends on the nanoparticles' size, shape, composition, interparticle distance, and environment (dielectric properties) [7–10]. As a result of these SPR modes, the nanoparticles absorb and scatter light so intensely that single NPs are easily observed by eye using dark-field (optical scattering) microscopy. Plasmonic NPs provide a nearly unlimited photon resource for observing molecular binding for longer periods of time, once they do not blink or bleach like fluorophores [11].

Nanoparticle-based colorimetric assays for diagnostics have been a subject of intensive research, where LSPR can

be used to detect DNA or proteins by the changes in the local index of refraction upon adsorption of the target molecule to the metal surface. Due to the intense SPR in the visible yielding extremely bright colors, gold nanoparticle colloids have been widely used of molecular diagnostics. In fact, gold nanoparticles (AuNPs) functionalized with ssDNA capable of specifically hybridizing to a complementary target in biological samples have been extensively used [12–27]. Other approaches use the AuNPs' plasmonic as a core/seed that can be tailored with a wide variety of surface functionalities to provide highly selective nanoprobe for diagnostics [28] or the SPR scattering imaging or SPR absorption spectroscopy generated from antibody-conjugated AuNPs in molecular biosensor techniques for the diagnosis of oral epithelial living cancer cells *in vivo* and *in vitro* [29] and the use of multi-functional AuNPs which incorporate both cytosolic delivery and targeting moieties on the same particle functioning as intracellular sensors to monitor actin rearrangement in live fibroblasts [30].

Plasmonic NPs have also been used as extremely intense labels for immunoassays [31–34] and biochemical sensors [19, 35–37]. Also, the use of colloidal silver plasmon resonant particles (PRPs) coated with standard ligands as target-specific labels has been reported for *in situ* hybridization and

immunocytology assays [34]. Most notably, a nanoparticle-based Biobar code has been developed for the detection of proteins that relies on magnetic microparticle probes with antibodies that specifically bind a target of interest and nanoparticle probes that are encoded with DNA that is unique to the protein target of interest and antibodies that can sandwich the target captured by the microparticle probes [33]. Haes and coworkers have reported on an optical biosensor based on localized surface plasmon resonance spectroscopy developed to monitor the interaction between the antigen, amyloid- β -derived diffusible ligands (ADDLs), and specific anti-ADDL antibodies, used in the detection of a biomarker for Alzheimer's Disease [35].

2.2. Raman-Spectroscopy-Based Systems. When light interacts with a substance, it can be absorbed, transmitted, or scattered. Scattered radiation can result from an elastic collision (Rayleigh scattering) or inelastic (Raman scattering). Raman spectroscopy is based on a change of frequency when light is inelastically scattered by molecules or atoms resulting in a molecular fingerprint information on molecular structure or intermolecular interaction of a specific process or molecule. The potential of Raman spectroscopy as biomedical diagnostics tool is rather low due to its low cross-section ($\sim 10^{-30}$ cm²) that results in low sensitivity [38]. However, in 1977, two groups independently described the use of noble metal surfaces to enhance the Raman scattering signal of target molecules [39, 40]—Surface enhancement raman spectroscopy (SERS). Jeanmaire and Van Duynne proposed a twofold electromagnetic field enhancement that was later associated with the interaction between the incident and scattered photons with the nanostructure's LSPR [41]. Simultaneously, Albrecht and Creighton suggested the source of the enhancement to be caused by a specific interaction between an adsorbate and the nanoparticle surface, briefly, a charge transfer from the adsorbate into the empty energetic levels on the metal surface or from the occupied levels of the nanoparticle's surface to the adsorbate [42–44].

Generally, SERS requires that the biological analyte reaches a suitable surface where the substrates are treated as two-dimensional macroscopic surfaces onto which adsorbed molecules suffer a local-field enhancement. Despite direct adsorption not being a good solution because of its dependence on the affinity between substrate and analyte, a method to identify and distinguish different strains of virus based on signal differences generated by the surface aminoacids using silver nanorods has been successfully developed [45]. Using a similar approach of direct adsorption, Pinzary et al. used naked silver nanoparticles to differentiate *in situ* healthy colon from carcinoma colon tissue [46]. Nanotags have been widely employed to address the lack of specificity [47, 48]. These nanotags usually possess a metallic colloidal core functionalized with a Raman reporting molecule and the specific molecule used to capture the analyte and have been used to directly detect DNA sequences [49, 50] and amplified DNA products of epizootic pathogens using complementary DNA strands so that only the complementary target hybridizes with the probes [51]. Using a similar

system, but exploring the distance-dependent enhancement of the electromagnetic field with a hairpin probe molecule, Wabuyele has also been used to distinguish single nucleotide polymorphisms in cancer-related genes [52]. Combining nanotags with other nanoparticles or binding surfaces that target the same analyte in a sandwich conformation proved useful to detect antibodies in serum [53]. A similar approach using a flat substrate instead of NPs had already been proposed to detect DNA, RNA, and proteins [54, 55]. However, in this approach, the substrate is used only to immobilize the analyte; a gold-nanoparticle-based nanotag is used to identify the analyte and the surface enhancement is obtained by silver coating of the nanotag. miRNA profiling has also been pursued via a slightly different approach based on the hybridization of the target molecules with a thiolated oligonucleotide and subsequent functionalization on a silver substrate [56]. SERS have also been explored to identify changes in the analyzed system such as interaction between DNA and xenobiotic molecules like cisplatin [57] or DNA-binding proteins [58, 59]. The combination of magnetic iron/gold core-shell nanoparticles with gold nanorods has also been used to specifically enumerate *E. coli* in water samples in a rapid and sensitive test [60]. In this case, the magnetic nanoparticles are used to concentrate the bacteria, improving the Raman signal by concentration and the posteriorly added gold nanorods serve as Raman signal enhancers.

SERS can also be used in conjunction with colloidal gold to detect and target tumors *in vivo*, where the AuNPs are surrounded with Raman reporters that provide light emission 200 times brighter than quantum dots [61, 62]. It was also found that the Raman reporters became more stable and yielded larger optical enhancements when NPs were encapsulated with a thiol-modified polyethylene glycol coat, which also allows for increased biocompatibility and circulation times *in vivo*. When conjugated to tumor-targeting ligands, these conjugated SERS-NPs were able to target tumor markers at surface of malignant cells, such as epidermal growth factor receptor (EGFR) that is sometimes overexpressed in cells of certain cancer types [29] and used to locate the tumor in xenograft tumor models [50].

2.3. Fluorescence-Based Systems. Quantum dots (QDs) are semiconductor nanoparticles with narrow, tunable, symmetrical emission spectra, and high quantum yields [63–65], and together with compatibility with DNA and proteins, make QDs exceptional substitutes as fluorescence labels. The use of QDs for nucleic acid characterization has long been proposed, for example, CdSe/ZnS QDs for SNP identification on human TP53 gene, multiallele detection of hepatitis B and C viruses [66], and *in situ* detection of chromosome abnormalities and mutations [67]. QDs have also been used as chemical sensors by exploring a typical FRET system where a dark quencher is placed at a protein-binding site attached to a QD surface. The quantum dots emission is quenched in presence of the analyte and upon analyte displacement the emission is restored [68]. A simpler approach was used to detect adenine using fluorescent ZnS nanoparticles at pH7, making use of capability of

adenine itself to quench emission of the quantum-dot-like nanoparticles [69].

Several studies report on the modulation of fluorophores at the vicinity of nanoparticles (e.g., gold, silver, and quantum dots) [70, 71], an interaction that has found application in a variety of systems to detect biologically relevant targets with particular focus upon AuNPs due to their ease in functionalization with biomolecules [72–75]. Several methods based on the quenching of fluorescence have been proposed for DNA detection consisting of fluorophore-labeled ssDNA electrostatically adsorbed onto gold nanoparticles [76], carbon nanotubes [77], and carbon nanoclots [78], where the presence of a complementary target triggers desorption of the newly formed dsDNA from the nanostructures due to the electrostatic variation between ssDNA and dsDNA, and fluorescence emission is restored. Also, fluorescence quenching of fluorophores close to metal nanoparticles functionalized with thiol-modified oligonucleotides has been explored in different conformations. Tang and co-workers proposed a method to probe hydroxyl radicals using an AuNP-oligonucleotide-FAM system where the hydroxyl radical promotes strand breakage and consequent release of FAM, restoring the previously quenched fluorescence [79]. The same quenching mechanism was used to detect specific DNA strands using two probes (one with an AuNP label and another labeled with TAMRA) that hybridize to two DNA sequences near each other [80], bringing the fluorophore and AuNP close enough to quench fluorescence emission.

Proteins have also been probed through nanoparticle-fluorescence-mediated systems, for example, human blood proteins have been let to interact with fluorescent AuNPs and detected through quenching [81]. In another example, a sandwich immunoassay using AuNPs quenching has been proposed for the detection of the protein cardiac troponin T by its interaction with two different antibodies, one attached to AuNPs and the other labeled with fluorescent dyes [82]. By means of an opposite modulation, infrared fluorescent nanoparticles showed enhanced fluorescence when interacting with protein [83].

A popular application of fluorescence modulation by nanoparticles has been specific ion sensing. Su and co-workers developed a copper sensor by covering fluorescent DNA-Cu/Ag nanoclusters with mercaptopropionic acid which quenches the intrinsic fluorescence of the nanoparticle; in the presence of Cu^{2+} , the capping agent is oxidized to form a disulfide compound resulting in release of the nanoparticle and restoration of emission suitable for quantification between 5 and 200 nM [84]. A very specific colorimetric and fluorimetric method to detect Hg^{2+} ions was developed with porphyrin-modified $\text{Au}@\text{SiO}_2$ nanoparticles, where the intensively fluorescent red complex turns green and weakly fluorescent in presence of Hg^{2+} [85]. Another examples include sensing of Pb^{2+} and adenosine by combining an adenosine aptamer and a DNAzyme with an abasic site where 2-amino-5,6,7-trimethyl-1,8-naphthyridine is trapped to quench its fluorescence [86]. When in solution, Pb^{2+} enables the DNAzyme to cleave its substrate thus removing the fluorescent compound from the abasic site restoring its fluorescence. Similarly, the presence

of adenosine induces structural change of the aptamer, resulting in the release of the fluorescent molecule from the DNA duplex and a subsequent fluorescence enhancement.

2.4. Nanophotonics Bioimaging. Nanoparticles show unique features suitable for biomedical imaging applications, such as an increased sensitivity in detection through amplification of signal changes (e.g., magnetic resonance imaging); high fluorescence quantum yields and large magnetic moments; properties that induce phagocytosis and selective uptake by macrophages (e.g., liposomes); physicochemical manipulations of energy (i.e., quantum dots); among others [87]. Because light absorption from biologic tissue components is minimized at near infrared (NIR) wavelengths, most nanoparticles (e.g., noble metal and magnetic NPs, nanoshells, nanoclusters, nanocages, nanorods and quantum dots) for *in vivo* imaging and therapy have been designed to strongly absorb in the NIR and used for *in vivo* diagnostics [83, 88, 89]. Ex vivo and *in vivo* imaging applications of nanoparticles have included their use as contrast agents for magnetic resonance imaging (MRI) [90], optical coherence tomography (OCT) [91–93], photoacoustic imaging (PAI) [94], and two-photon luminescence (TPL) spectroscopy [95].

2.4.1. Magnetic Resonance Imaging. Magnetic resonance imaging (MRI) is based heavily on nuclear magnetic resonance (NMR), first described by R. Damadian. Magnetic resonance measurements cause no obvious deleterious effects on biological tissue, and the incident radiation consists of common radio frequencies at right angles to a static magnetic field [96]. Iron oxide nanoparticles show superparamagnetism, allowing for the facile alignment of the magnetic moments to an applied magnetic field, thus of great interest as contrast agents for MRI [97]. Presently, magnetic iron oxide nanoparticles are routinely used as contrast agents to enhance an MRI image, providing sharper contrast between soft and hard tissue in the body (e.g. liver and spleen or lymph nodes) [98]. Jun et al. presented a synthetically controlled magnetic nanocrystal model system that led to the improvement of high-performance nanocrystal—antibody probe systems for the diagnosis of breast cancer cells via magnetic resonance imaging [99]. Also, MnFe_2O_4 nanocrystals *functionalized* with an antibody conjugate (herceptin) capable of specific targeting of cancerous cells was successfully used for *in vivo* MRI in mice [88]. Driehuysb et al. developed an imaging method to detect submillimeter-sized metastases with molecular specificity by targeting cancer cells with iron oxide nanoparticles functionalized with cancer-binding ligands, demonstrating *in vivo* detection of pulmonary micrometastases in mice injected with breast adenocarcinoma cells [100]. Hybrid NPs with a superparamagnetic iron oxide/silica core and a gold nanoshell, with significant absorbance and scattering in the NIR region, have been used *in vivo* as contrast agents for MRI presenting a good MR signal in hepatoma, each moiety providing for a distinct signal that enhanced detection [101].

2.4.2. Optical Coherence Tomography. Optical Coherence Tomography (OCT) is an imaging modality that provides cross-sectional subsurface imaging of biological tissue with micrometer scale resolution which is based on a broadband light source and a fiber-optic interferometer. It captures three-dimensional images from within optical scattering media, typically employing near-infrared light. The use of relatively long wavelength light allows it to penetrate into the scattering medium [102–104]. The extra scattering provided by Au-nanoshells enhances optical contrast and brightness for improved diagnostic imaging of tumors in mice due to the preferential accumulation of the nanoshells in the tumor [105]. Tseng et al. developed nanorings with a localized surface plasmon resonance covering a spectral range of 1300 nm that produced both photothermal and image contrast enhancement effects in OCT when delivered into pig adipose samples [106]. Additionally, the image contrast enhancement effect could be isolated by continuously scanning the sample with a lower scan frequency, allowing to effectively control the therapeutic modality. In the same way, gold capped nanoroses have been used in photothermal OCT to detect macrophages in *ex vivo* rabbit arteries [107].

2.4.3. Photoacoustic Imaging. In photoacoustic imaging (PAI) and photoacoustic tomography (PAT), a pulse of NIR laser light, typically 757 nm, is used in resonance with the surface plasmon instead of a continuous NIR source. With this technique causing rapid thermal expansion of the surrounding media, the generated sound wave can be detected on the surface of the subject. NIR reduces the amount of absorption that occurs, but absorption of light by various other organs is unavoidable [108, 109]. Yang et al. demonstrated the feasibility of using poly(ethylene glycol)-coated Au nanocages as a new *in vivo* NIR contrast-enhancing agent for photoacoustic tomography and image their distribution in the vasculature of rat brain. These Au-nanocages enhanced the contrast between blood and the surrounding tissues by up to 81%, achieving a more detailed image of vascular structures at greater depths. Additionally, they were shown to present slight advantages over Au-nanoshells, being better suited for *in vivo* applications, specially due to their more compact size (<50 nm compared to >100 nm for Au-nanoshells) and larger optical absorption cross-sections [110]. Due to the ability of gold-nanorods to have the maximum of the plasmon resonance tuned further into the NIR, Motamedi et al. reported a contrast agent for a laser optoacoustic imaging system for *in vivo* detection of gold nanorods and to enhance the diagnostic power of optoacoustic imaging [111]. Song et al. proposed a noninvasive *in vivo* spectroscopic photoacoustic sentinel lymph node mapping in a rat model using gold nanorods as lymph node tracers [112].

2.4.4. Two-Photon Luminescence. In two-photon luminescence (TPL) spectroscopy, an electron is excited from the conduction band to the valence band of the metal nanoparticles using two photons. As the electron relaxes to the conduction band, light is released and amplified

due to a resonant coupling with localized surface plasmons, enhancing a variety of linear and nonlinear optical properties [113, 114]. TPL was first described by Boyd et al. that found that roughened metal surfaces exhibited much higher induced luminescence efficiency than smooth surfaces [115]. In fact, TPL is a potentially powerful technique for noninvasive imaging at the micron scale hundreds of microns deep into scattering tissue. This way, it ought to be possible to discriminate cancerous and healthy tissue based on two-photon imaging from endogenous fluorophores. For enhanced imaging, two-photon contrast agents have been developed showing the ability to increase signal-to-noise ratio and targeted to molecular signatures of interest that are not fluorescent. Because imaging of intrinsic fluorophores is often difficult due to their relatively weak signals, the use of such a bright contrast agent holds the promise to enable *in vivo* applications of two photon imaging in a clinical setting [113, 116, 117]. Wang et al. collected images of single gold nanorods flowing in the mouse ear blood vessels with luminescence three times stronger than background [114]. It is worth mentioning that the TPL signal from a single nanorod is 58 times that of the two-photon fluorescence signal from a single rhodamine molecule.

2.4.5. QDs for In Vivo Imaging. In the last decade, water soluble bioconjugated QDs have been increasingly applied for imaging [63, 64, 118] However, QD probes for imaging show poor stability once inside cytosolic environment and reduced biocompatibility in living organisms [119], which constitutes a serious drawback for widespread *in vivo* application.

Despite the serious concerns related to the *in vivo* use of QDs, these nanocrystals show remarkable imaging properties that may be judged of value for improved diagnostics. In fact, QDs have proven of great value when imaging vascular networks of mammals such as lymphatic and cardiovascular systems [120–124]. Also, Kim et al. demonstrated that quantum dots allowed a major cancer surgery to be performed in large animals (mice and pigs) under complete image guidance, by locating the position of sentinel lymph nodes [125]. With similar potential to that observed when imaging the lymph system, the imaging of cardiovascular systems has also been achieved using QDs [126, 127]. Larson et al. demonstrated that QDs retained their fluorescence after injection and could be detected in the capillaries of skin and adipose tissue of a mouse [128]. The fluorescent emission and multiplexing capabilities of QDs are being exploited to improve the sensitivity and selectivity in the early detection of tumors [61, 129, 130]. Åkerman et al. described for the first time the application of targeted cancer imaging by using ZnS-capped CdSe QDs coated with a lung-targeting peptide that accumulate in the lungs of mice, whereas two other peptides specifically direct QDs to blood vessels or lymphatic vessels in tumors [131]. Later, Gao et al. described the development of multifunctional nanoparticle probes based on QDs with a copolymer linked to tumor-targeting ligands and drug-delivery functionalities for cancer targeting and imaging in living animals [132]. Once the toxicological aspects associated with QDs have been clarified, such studies

demonstrate the potential of QDs for ultrasensitive and multiplexed imaging of molecular targets *in vivo*.

3. Nanophotonics for Therapy

Nanophototherapy uses pulsed lasers and absorbing nanoparticles attached to specific targets for selective damage to cancer cells. Plasmonic photothermal therapy (PPTT) and photodynamic therapy (PDT) are two of the main techniques that take advantage of the selective absorbance of the surface plasmon resonance and the fact that the nanoparticles relax by liberating heat into their surrounding environment.

3.1. Plasmonic Photothermal Therapy. Plasmonic photothermal therapy is a less invasive experimental technique that holds great promise for the treatment of cell malignancies and, in particular, of cancer. It combines two key components: (i) light source, specifically lasers with a spectral range of 650–900 nm for deep tissue penetration and (ii) optical absorption of AuNPs which release the optical irradiation as heat in the picoseconds time scale, thereby inducing photothermal ablation [133–135]. Kirui et al. reported the use of gold and iron oxide hybrid nanoparticles in targeting, imaging, and selective thermal killing of colorectal cancer cells [136]. Huang and colleagues have demonstrated that gold nanorods have a longitudinal absorption band in the NIR on account of SPR oscillations and are effective as photothermal agents [137]. Gold nanorods aspect ratios allow tuning the SPR band from the visible to the NIR (transmits readily through human skin and tissue), making them suitable for photothermal converters of near infrared light for *in vivo* applications [138, 139]. Effective photothermal destruction of cancer cells and tissue have been demonstrated for other gold nanostructures, such as branched gold nanoparticles [140], gold nanoshells [141–143], gold nanocages [134], and gold nanospheres [144].

3.2. Photodynamic Therapy. Photodynamic therapy employs chemical photosensitizers that generate reactive oxygen species (ROS), such as a singlet oxygen ($^1\text{O}_2$), capable of tumor destruction [145, 146]. This technique is noninvasive and can be applied locally or systemically without noticeable cumulative toxicity effects without high costs. To attain maximal killing efficiency of tumor cells, the photosensitizer must be in close proximity to the tumor cells, thus requiring specific targeting when administered systemically. One of the major limitations is the poor tissue penetration of high-energy light and the systemic dispersal of the photosensitizer [147, 148].

Aiming at circumventing some of the limitations of photodynamic therapy, Zhang et al. reported a new type of photosensitizers based on photon upconverting nanoparticles (a process where low energy light, usually near-infrared (NIR) or infrared (IR), is converted to higher energies, ultraviolet (UV), or visible, via multiple absorptions or energy transfer steps) [149, 150]. One year later, Yong et al. reported the use of NPs modified with zinc phthalocyanin photosensitizer that produce green/red emission on near-infrared (NIR)

excitation and is capable of singlet oxygen sensitization; upon targeted binding to cancer cells, significant cell destruction was induced [151]. Recently, Qian et al. published similar results with the use of zinc phthalocyanine nanocrystals coated with a uniform layer of mesoporous silica [152].

4. Conclusions

Light is an amazing intermediate with a gargantuan capacity for carrying multiple information and functions. Instinctively, we view light as rays, which propagate in a single direction, either being absorbed or reflected to some extent by any object on which it impinges. However, the propagation of light through a material is itself a quantum effect, involving the excitation and relaxation of electrons in the material. It is well known that light has the facility to act through biological, chemical, mechanical, and thermal pathways at molecular/cellular levels in diagnostic and therapeutic applications.

Currently, we are in the dawn of a new age in therapy driven by nanotechnology vehicles. Although there are technical challenges associated with the therapeutic application of nanodevices, the integration of therapy with diagnostic profiling has accelerated the pace of discovery of new nanotechnology methods. In addition to continuing to push forward on the above challenges, nanotechnology together with photonics can be used both for identifying useful target candidates and for validating their importance in disease states. Nanophotonics may present new opportunities for personalized medicine in which diagnosis and treatment are based on each individual's molecular profile. Further research into the fundamental mechanisms that efficiently control light using nanodevices could unveil new dimensions of nanoparticle-mediated theranostic systems.

Here, we have attempted to give the reader a limited overview of some aspects of the current state of research into the fascinating aspects and control over nanophotonics in molecular diagnostics and therapy applications.

Acknowledgment

The authors acknowledge FCT/MCTES—CIGMH (Portugal) for financial support.

References

- [1] M. Ohtsu, K. Kobayashi, T. Kawazoe, T. Yatsui, and M. Naruse, *Principles of Nanophotonics*, Series in Optics and Optoelectronics, Taylor & Francis, CRC Press, 2008.
- [2] Y. Shen and P. N. Prasad, "Nanophotonics: a new multidisciplinary frontier," *Applied Physics B*, vol. 74, no. 7-8, pp. 641–645, 2002.
- [3] T. Lammers, S. Aime, W. E. Hennink, G. Storm, and F. Kiessling, "Theranostic nanomedicines," *Accounts of Chemical Research*. In press.
- [4] F. Pene, E. Courtine, A. Cariou, and J. P. Mira, "Toward theragnostics," *Critical Care Medicine*, vol. 37, no. 1, pp. S50–S58, 2009.

- [5] W. L. Barnes, A. Dereux, and T. W. Ebbesen, "Surface plasmon subwavelength optics," *Nature*, vol. 424, no. 6950, pp. 824–830, 2003.
- [6] U. Kreibig and M. Vollmer, *Optical Properties of Metal Clusters*, vol. 25 of *Springer Series in Materials Science*, Springer, Berlin, Germany, 1995.
- [7] M. C. Daniel and D. Astruc, "Gold nanoparticles: assembly, supramolecular chemistry, quantum-size-related properties, and applications toward biology, catalysis, and nanotechnology," *Chemical Reviews*, vol. 104, no. 1, pp. 293–346, 2004.
- [8] S. Eustis and M. A. El-Sayed, "Why gold nanoparticles are more precious than pretty gold: Noble metal surface plasmon resonance and its enhancement of the radiative and nonradiative properties of nanocrystals of different shapes," *Chemical Society Reviews*, vol. 35, no. 3, pp. 209–217, 2006.
- [9] S. K. Ghosh and T. Pal, "Interparticle coupling effect on the surface plasmon resonance of gold nanoparticles: from theory to applications," *Chemical Reviews*, vol. 107, no. 11, pp. 4797–4862, 2007.
- [10] W. Zhao, M. A. Brook, and Y. Li, "Design of gold nanoparticle-based colorimetric biosensing assays," *ChemBioChem*, vol. 9, no. 15, pp. 2363–2371, 2008.
- [11] J. N. Anker, W. P. Hall, O. Lyandres, N. C. Shah, J. Zhao, and R. P. Van Duyne, "Biosensing with plasmonic nanosensors," *Nature Materials*, vol. 7, no. 6, pp. 442–453, 2008.
- [12] P. Baptista, G. Doria, D. Henriques, E. Pereira, and R. Franco, "Colorimetric detection of eukaryotic gene expression with DNA-derivatized gold nanoparticles," *Journal of Biotechnology*, vol. 119, no. 2, pp. 111–117, 2005.
- [13] P. Baptista, E. Pereira, P. Eaton et al., "Gold nanoparticles for the development of clinical diagnosis methods," *Analytical and Bioanalytical Chemistry*, vol. 391, no. 3, pp. 943–950, 2008.
- [14] Y. C. Cao, R. Jin, C. S. Thaxton, and C. A. Mirkin, "A two-color-change, nanoparticle-based method for DNA detection," *Talanta*, vol. 67, no. 3, pp. 449–455, 2005.
- [15] M. M. C. Cheng, G. Cuda, Y. L. Bunimovich et al., "Nanotechnologies for biomolecular detection and medical diagnostics," *Current Opinion in Chemical Biology*, vol. 10, no. 1, pp. 11–19, 2006.
- [16] J. Conde, J. M. de la Fuente, and P. V. Baptista, "RNA quantification using gold nanoprobe - application to cancer diagnostics," *Journal of Nanobiotechnology*, vol. 8, article no. 5, 2010.
- [17] P. Costa, A. Amaro, A. Botelho, J. Inácio, and P. V. Baptista, "Gold nanoprobe assay for the identification of mycobacteria of the *Mycobacterium tuberculosis* complex," *Clinical Microbiology and Infection*, vol. 16, no. 9, pp. 1464–1469, 2010.
- [18] G. Doria, R. Franco, and P. Baptista, "Nanodiagnosics: fast colorimetric method for single nucleotide polymorphism/mutation detection," *IET Nanobiotechnology*, vol. 1, no. 4, pp. 53–57, 2007.
- [19] R. Elghanian, J. J. Storhoff, R. C. Mucic, R. L. Letsinger, and C. A. Mirkin, "Selective colorimetric detection of polynucleotides based on the distance-dependent optical properties of gold nanoparticles," *Science*, vol. 277, no. 5329, pp. 1078–1081, 1997.
- [20] H. Li and L. Rothberg, "Colorimetric detection of DNA sequences based on electrostatic interactions with unmodified gold nanoparticles," *Proceedings of the National Academy of Sciences of the United States of America*, vol. 101, no. 39, pp. 14036–14039, 2004.
- [21] C. A. Mirkin, R. L. Letsinger, R. C. Mucic, and J. J. Storhoff, "A DNA-based method for rationally assembling nanoparticles into macroscopic materials," *Nature*, vol. 382, no. 6592, pp. 607–609, 1996.
- [22] W. J. Qin and L. Y. L. Yung, "Nanoparticle-based detection and quantification of DNA with single nucleotide polymorphism (SNP) discrimination selectivity," *Nucleic Acids Research*, vol. 35, no. 17, article no. e111, 2007.
- [23] K. Sato, K. Hosokawa, and M. Maeda, "Rapid aggregation of gold nanoparticles induced by non-cross-linking DNA hybridization," *Journal of the American Chemical Society*, vol. 125, no. 27, pp. 8102–8103, 2003.
- [24] K. Sato, K. Hosokawa, and M. Maeda, "Non-cross-linking gold nanoparticle aggregation as a detection method for single-base substitutions," *Nucleic Acids Research*, vol. 33, no. 1, article e4, 2005.
- [25] J. J. Storhoff, A. D. Lucas, V. Garimella, Y. P. Bao, and U. R. Müller, "Homogeneous detection of unamplified genomic DNA sequences based on colorimetric scatter of gold nanoparticle probes," *Nature Biotechnology*, vol. 22, no. 7, pp. 883–887, 2004.
- [26] T. A. Taton, C. A. Mirkin, and R. L. Letsinger, "Scanometric DNA array detection with nanoparticle probes," *Science*, vol. 289, no. 5485, pp. 1757–1760, 2000.
- [27] C. S. Thaxton, D. G. Georganopoulou, and C. A. Mirkin, "Gold nanoparticle probes for the detection of nucleic acid targets," *Clinica Chimica Acta*, vol. 363, no. 1-2, pp. 120–126, 2006.
- [28] C. C. You, O. R. Miranda, B. Gider et al., "Detection and identification of proteins using nanoparticle-fluorescent polymer 'chemical nose' sensors," *Nature Nanotechnology*, vol. 2, no. 5, pp. 318–323, 2007.
- [29] I. H. El-Sayed, X. Huang, and M. A. El-Sayed, "Surface plasmon resonance scattering and absorption of anti-EGFR antibody conjugated gold nanoparticles in cancer diagnostics: applications in oral cancer," *Nano Letters*, vol. 5, no. 5, pp. 829–834, 2005.
- [30] S. Kumar, N. Harrison, R. Richards-Kortum, and K. Sokolov, "Plasmonic nanosensors for imaging intracellular biomarkers in live cells," *Nano Letters*, vol. 7, no. 5, pp. 1338–1343, 2007.
- [31] W.-C. Law, K.-T. Yong, A. Baev, and P. N. Prasad, "Sensitivity improved surface plasmon resonance biosensor for cancer biomarker detection based on plasmonic enhancement," *ACS Nano*, vol. 5, no. 6, pp. 4858–4864, 2011.
- [32] J. S. Mitchell and T. E. Lowe, "Ultrasensitive detection of testosterone using conjugate linker technology in a nanoparticle-enhanced surface plasmon resonance biosensor," *Biosensors and Bioelectronics*, vol. 24, no. 7, pp. 2177–2183, 2009.
- [33] J. M. Nam, C. S. Thaxton, and C. A. Mirkin, "Nanoparticle-based bio-bar codes for the ultrasensitive detection of proteins," *Science*, vol. 301, no. 5641, pp. 1884–1886, 2003.
- [34] S. Schultz, D. R. Smith, J. J. Mock, and D. A. Schultz, "Single-target molecule detection with nonbleaching multicolor optical immunolabels," *Proceedings of the National Academy of Sciences of the United States of America*, vol. 97, no. 3, pp. 996–1001, 2000.
- [35] A. J. Haes, L. Chang, W. L. Klein, and R. P. Van Duyne, "Detection of a biomarker for Alzheimer's disease from synthetic and clinical samples using a nanoscale optical biosensor," *Journal of the American Chemical Society*, vol. 127, no. 7, pp. 2264–2271, 2005.

- [36] A. D. McFarland and R. P. Van Duyne, "Single silver nanoparticles as real-time optical sensors with zeptomole sensitivity," *Nano Letters*, vol. 3, no. 8, pp. 1057–1062, 2003.
- [37] G. Raschke, S. Kowarik, T. Franzl et al., "Biomolecular recognition based on single gold nanoparticle light scattering," *Nano Letters*, vol. 3, no. 7, pp. 935–938, 2003.
- [38] M. K. Hossain and Y. Ozaki, "Surface-enhanced Raman scattering: facts and inline trends," *Current Science*, vol. 97, no. 2, pp. 192–201, 2009.
- [39] D. L. Jeanmaire and R. P. Van Duyne, "Surface Raman spectroelectrochemistry Part I. Heterocyclic, aromatic, and aliphatic amines adsorbed on the anodized silver electrode," *Journal of Electroanalytical Chemistry*, vol. 84, no. 1, pp. 1–20, 1977.
- [40] M. G. Albrecht and J. A. Creighton, "Anomalous intense Raman spectra of pyridine at a silver electrode," *Journal of the American Chemical Society*, vol. 99, no. 15, pp. 5215–5217, 1977.
- [41] B. Pettinger, "Light scattering by adsorbates at Ag particles: quantum-mechanical approach for energy transfer induced interfacial optical processes involving surface plasmons, multipoles, and electron-hole pairs," *The Journal of Chemical Physics*, vol. 85, no. 12, pp. 7442–7451, 1986.
- [42] A. M. Michaels, M. Nirmal, and L. E. Brus, "Surface enhanced Raman spectroscopy of individual rhodamine 6G molecules on large Ag nanocrystals," *Journal of the American Chemical Society*, vol. 121, no. 43, pp. 9932–9939, 1999.
- [43] P. Etchegoin, H. Liem, R. C. Maher et al., "A novel amplification mechanism for surface enhanced Raman scattering," *Chemical Physics Letters*, vol. 366, no. 1-2, pp. 115–121, 2002.
- [44] A. Otto, "On the electronic contribution to single molecule surface enhanced Raman spectroscopy," *Indian Journal of Physics*, vol. 77B, pp. 63–73, 2003.
- [45] S. Shanmukh, L. Jones, J. Driskell, Y. Zhao, R. Dluhy, and R. A. Tripp, "Rapid and sensitive detection of respiratory virus molecular signatures using a silver nanorod array SERS substrate," *Nano Letters*, vol. 6, no. 11, pp. 2630–2636, 2006.
- [46] S. C. Pinzaru, L. M. Andronie, I. Domsa, O. Cozar, and S. Astilean, "Bridging biomolecules with nanoparticles: surface-enhanced Raman scattering from colon carcinoma and normal tissue," *Journal of Raman Spectroscopy*, vol. 39, no. 3, pp. 331–334, 2008.
- [47] S. P. Mulvaney, M. D. Musick, C. D. Keating, and M. J. Natan, "Glass-coated, analyte-tagged nanoparticles: a new tagging system based on detection with surface-enhanced Raman scattering," *Langmuir*, vol. 19, no. 11, pp. 4784–4790, 2003.
- [48] W. E. Doering, M. E. Piotti, M. J. Natan, and R. G. Freeman, "SERS as a foundation for nanoscale, optically detected biological labels," *Advanced Materials*, vol. 19, no. 20, pp. 3100–3108, 2007.
- [49] L. Sun, C. Yu, and J. Irudayaraj, "Surface-enhanced Raman scattering based nonfluorescent probe for multiplex DNA detection," *Analytical Chemistry*, vol. 79, no. 11, pp. 3981–3988, 2007.
- [50] X. Qian, X. Zhou, and S. Nie, "Surface-enhanced Raman nanoparticle beacons based on bioconjugated gold nanocrystals and long range plasmonic coupling," *Journal of the American Chemical Society*, vol. 130, no. 45, pp. 14934–14935, 2008.
- [51] K. K. Strelau, A. Brinker, C. Schnee, K. Weber, R. Möller, and J. Popp, "Detection of PCR products amplified from DNA of epizootic pathogens using magnetic nanoparticles and SERS," *Journal of Raman Spectroscopy*, vol. 42, no. 3, pp. 243–250, 2011.
- [52] M. B. Wabuyele, F. Yan, and T. Vo-Dinh, "Plasmonics nanoprobes: detection of single-nucleotide polymorphisms in the breast cancer BRCA1 gene," *Analytical and Bioanalytical Chemistry*, vol. 398, no. 2, pp. 729–736, 2010.
- [53] J. Neng, M. H. Harpster, H. Zhang, J. O. Mecham, W. C. Wilson, and P. A. Johnson, "A versatile SERS-based immunoassay for immunoglobulin detection using antigen-coated gold nanoparticles and malachite green-conjugated protein A/G," *Biosensors and Bioelectronics*, vol. 26, no. 3, pp. 1009–1015, 2010.
- [54] Y. C. Cao, R. Jin, and C. A. Mirkin, "Nanoparticles with Raman spectroscopic fingerprints for DNA and RNA detection," *Science*, vol. 297, no. 5586, pp. 1536–1540, 2002.
- [55] Y. C. Cao, R. Jin, J. M. Nam, C. S. Thaxton, and C. A. Mirkin, "Raman dye-labeled nanoparticle probes for proteins," *Journal of the American Chemical Society*, vol. 125, no. 48, pp. 14676–14677, 2003.
- [56] J. D. Driskell and R. A. Tripp, "Label-free SERS detection of microRNA based on affinity for an unmodified silver nanorod array substrate," *Chemical Communications*, vol. 46, no. 19, pp. 3298–3300, 2010.
- [57] A. Barhoumi, D. Zhang, F. Tam, and N. J. Halas, "Surface-enhanced Raman spectroscopy of DNA," *Journal of the American Chemical Society*, vol. 130, no. 16, pp. 5523–5529, 2008.
- [58] D. Graham, R. Stevenson, D. G. Thompson, L. Barrett, C. Dalton, and K. Faulds, "Combining functionalised nanoparticles and SERS for the detection of DNA relating to disease," *Faraday Discussions*, vol. 149, pp. 291–299, 2011.
- [59] C. V. Pagba, S. M. Lane, H. Cho, and S. Wachsmann-Hogiu, "Direct detection of aptamer-thrombin binding via surface-enhanced Raman spectroscopy," *Journal of Biomedical Optics*, vol. 15, no. 4, Article ID 047006, 2010.
- [60] B. Guven, N. Basaran-Akgul, E. Temur, U. Tamer, and I. H. Boyaci, "SERS-based sandwich immunoassay using antibody coated magnetic nanoparticles for Escherichia coli enumeration," *Analyst*, vol. 136, no. 4, pp. 740–748, 2011.
- [61] W. Cai, D. W. Shin, K. Chen et al., "Peptide-labeled near-infrared quantum dots for imaging tumor vasculature in living subjects," *Nano Letters*, vol. 6, no. 4, pp. 669–676, 2006.
- [62] J. Kneipp, H. Kneipp, M. McLaughlin, D. Brown, and K. Kneipp, "In vivo molecular probing of cellular compartments with gold nanoparticles and nanoaggregates," *Nano Letters*, vol. 6, no. 10, pp. 2225–2231, 2006.
- [63] W. C. W. Chan and S. Nie, "Quantum dot bioconjugates for ultrasensitive nonisotopic detection," *Science*, vol. 281, no. 5385, pp. 2016–2018, 1998.
- [64] M. Bruchez Jr., M. Moronne, P. Gin, S. Weiss, and A. P. Alivisatos, "Semiconductor nanocrystals as fluorescent biological labels," *Science*, vol. 281, no. 5385, pp. 2013–2016, 1998.
- [65] H. Weller, "Colloidal semiconductor Q-particles: chemistry in the transition region between solid state and molecules," *Angewandte Chemie - International Edition*, vol. 32, no. 1, pp. 41–53, 1993.
- [66] D. Gerion, F. Chen, B. Kannan et al., "Room-temperature single-nucleotide polymorphism and multiallele DNA detection using fluorescent nanocrystals and microarrays," *Analytical Chemistry*, vol. 75, no. 18, pp. 4766–4772, 2003.
- [67] S. Pathak, S. K. Choi, N. Arnheim, and M. E. Thompson, "Hydroxylated quantum dots as luminescent probes for in situ hybridization," *Journal of the American Chemical Society*, vol. 123, no. 17, pp. 4103–4104, 2001.

- [68] I. L. Medintz, A. R. Clapp, H. Mattoussi, E. R. Goldman, B. Fisher, and J. M. Mauro, "Self-assembled nanoscale biosensors based on quantum dot FRET donors," *Nature Materials*, vol. 2, no. 9, pp. 630–638, 2003.
- [69] L. M. Devi and D. P. S. Negi, "Sensitive and selective detection of adenine using fluorescent ZnS nanoparticles," *Nanotechnology*, vol. 22, no. 24, Article ID 245502, 2011.
- [70] J. Gersten and A. Nitzan, "Spectroscopic properties of molecules interacting with small dielectric particles," *The Journal of Chemical Physics*, vol. 75, no. 3, pp. 1139–1152, 1981.
- [71] K. A. Kang, J. Wang, J. B. Jasinski, and S. Achilefu, "Fluorescence manipulation by gold nanoparticles: from complete quenching to extensive enhancement," *Journal of Nanobiotechnology*, vol. 9, article 16, 2011.
- [72] A. Quarta, R. D. Corato, L. Manna, A. Ragusa, and T. Pellegrino, "Fluorescent-magnetic hybrid nanostructures: preparation, properties, and applications in biology," *IEEE Transactions on Nanobioscience*, vol. 6, no. 4, pp. 298–308, 2007.
- [73] J. R. Lakowicz, J. Malicka, E. Matveeva, I. Gryczynski, and Z. Gryczynski, "Plasmonic technology: novel approach to ultrasensitive immunoassays," *Clinical Chemistry*, vol. 51, no. 10, pp. 1914–1922, 2005.
- [74] J. R. Lakowicz, "Plasmonics in biology and plasmon-controlled fluorescence," *Plasmonics*, vol. 1, no. 1, pp. 5–33, 2006.
- [75] I. L. Medintz and H. Mattoussi, "Quantum dot-based resonance energy transfer and its growing application in biology," *Physical Chemistry Chemical Physics*, vol. 11, no. 1, pp. 17–45, 2009.
- [76] P. C. Ray, G. K. Darbha, A. Ray, J. Walker, and W. Hardy, "Gold nanoparticle based FRET for DNA detection," *Plasmonics*, vol. 2, no. 4, pp. 173–183, 2007.
- [77] Y. Liu, Y. Wang, J. Jin, H. Wang, R. Yang, and W. Tan, "Fluorescent assay of DNA hybridization with label-free molecular switch: reducing background-signal and improving specificity by using carbon nanotubes," *Chemical Communications*, no. 6, pp. 665–667, 2009.
- [78] W. Bai, H. Zheng, Y. Long, X. Mao, M. Gao, and L. Zhang, "A carbon dots-based fluorescence turn-on method for DNA determination," *Analytical Sciences*, vol. 27, no. 3, pp. 243–246, 2011.
- [79] B. Tang, N. Zhang, Z. Chen et al., "Probing hydroxyl radicals and their imaging in living cells by use of FAM-DNA-Au nanoparticles," *Chemistry*, vol. 14, no. 2, pp. 522–528, 2008.
- [80] Z. S. Wu, J. H. Jiang, L. Fu, G. L. Shen, and R. Q. Yu, "Optical detection of DNA hybridization based on fluorescence quenching of tagged oligonucleotide probes by gold nanoparticles," *Analytical Biochemistry*, vol. 353, no. 1, pp. 22–29, 2006.
- [81] S. H. De Paoli Lacerda, J. J. Park, C. Meuse et al., "Interaction of gold nanoparticles with common human blood proteins," *ACS Nano*, vol. 4, no. 1, pp. 365–379, 2010.
- [82] S. Mayilo, M. A. Kloster, M. Wunderlich et al., "Long-range fluorescence quenching by gold nanoparticles in a sandwich immunoassay for cardiac troponin T," *Nano Letters*, vol. 9, no. 12, pp. 4558–4563, 2009.
- [83] X. He, J. Gao, S. S. Gambhir, and Z. Cheng, "Near-infrared fluorescent nanoprobe for cancer molecular imaging: status and challenges," *Trends in Molecular Medicine*, vol. 16, no. 12, pp. 574–583, 2010.
- [84] Y. T. Su, G. Y. Lan, W. Y. Chen, and H. T. Chang, "Detection of copper ions through recovery of the fluorescence of DNA-templated copper/silver nanoclusters in the presence of mercaptopropionic acid," *Analytical Chemistry*, vol. 82, no. 20, pp. 8566–8572, 2010.
- [85] Y. Cho, S. S. Lee, and J. H. Jung, "Recyclable fluorimetric and colorimetric mercury-specific sensor using porphyrin-functionalized Au@SiO₂ core/shell nanoparticles," *Analyst*, vol. 135, no. 7, pp. 1551–1555, 2010.
- [86] Y. Xiang, A. Tong, and Y. Lu, "Abasic site-containing DNzyme and aptamer for label-free fluorescent detection of Pb²⁺ and adenosine with high sensitivity, selectivity, and tunable dynamic range," *Journal of the American Chemical Society*, vol. 131, no. 42, pp. 15352–15357, 2009.
- [87] R. Gill, M. Zayats, and I. Willner, "Semiconductor quantum dots for bioanalysis," *Angewandte Chemie - International Edition*, vol. 47, no. 40, pp. 7602–7625, 2008.
- [88] J. H. Lee, Y. M. Huh, Y. W. Jun et al., "Artificially engineered magnetic nanoparticles for ultra-sensitive molecular imaging," *Nature Medicine*, vol. 13, no. 1, pp. 95–99, 2007.
- [89] E. I. Altinoğlu and J. H. Adair, "Near infrared imaging with nanoparticles," *Wiley Interdisciplinary Reviews: Nanomedicine and Nanobiotechnology*, vol. 2, no. 5, pp. 461–477, 2010.
- [90] P. Vartholomeos, M. Fruchard, A. Ferreira, and C. Mavroidis, "MRI-guided nanorobotic systems for therapeutic and diagnostic applications," *Annual Review of Biomedical Engineering*, vol. 13, pp. 157–184, 2011.
- [91] E. V. Zagaynova, M. V. Shirmanova, M. Y. Kirillin et al., "Contrasting properties of gold nanoparticles for optical coherence tomography: phantom, in vivo studies and Monte Carlo simulation," *Physics in Medicine and Biology*, vol. 53, no. 18, pp. 4995–5009, 2008.
- [92] J. C. Kah, M. Olivo, T. H. Chow et al., "Control of optical contrast using gold nanoshells for optical coherence tomography imaging of mouse xenograft tumor model in vivo," *Journal of Biomedical Optics*, vol. 14, no. 5, Article ID 054015, 2009.
- [93] A. L. Oldenburg, M. N. Hansen, T. S. Ralston, A. Wei, and S. A. Boppart, "Imaging gold nanorods in excised human breast carcinoma by spectroscopic optical coherence tomography," *Journal of Materials Chemistry*, vol. 19, no. 35, pp. 6407–6411, 2009.
- [94] X. Yang, E. W. Stein, S. Ashkenazi, and L. V. Wang, "Nanoparticles for photoacoustic imaging," *Wiley Interdisciplinary Reviews. Nanomedicine and nanobiotechnology*, vol. 1, no. 4, pp. 360–368, 2009.
- [95] M. B. Mohamed, V. Volkov, S. Link, and M. A. El-Sayed, "The 'lightning' gold nanorods: fluorescence enhancement of over a million compared to the gold metal," *Chemical Physics Letters*, vol. 317, no. 6, pp. 517–523, 2000.
- [96] R. Damadian, "Tumor detection by nuclear magnetic resonance," *Science*, vol. 171, no. 3976, pp. 1151–1153, 1971.
- [97] D. S. Mathew and R. S. Juang, "An overview of the structure and magnetism of spinel ferrite nanoparticles and their synthesis in microemulsions," *Chemical Engineering Journal*, vol. 129, no. 1–3, pp. 51–65, 2007.
- [98] S. Laurent, D. Forge, M. Port et al., "Magnetic iron oxide nanoparticles: synthesis, stabilization, vectorization, physicochemical characterizations and biological applications," *Chemical Reviews*, vol. 108, no. 6, pp. 2064–2110, 2008.
- [99] Y. W. Jun, Y. M. Huh, J. S. Choi et al., "Nanoscale size effect of magnetic nanocrystals and their utilisation for cancer diagnosis via magnetic resonance imaging," *Journal of the American Chemical Society*, vol. 127, no. 16, pp. 5732–5733, 2005.

- [100] R. T. Branca, Z. I. Cleveland, B. Fubara et al., "Molecular MRI for sensitive and specific detection of lung metastases," *Proceedings of the National Academy of Sciences of the United States of America*, vol. 107, no. 8, pp. 3693–3697, 2010.
- [101] D. Kim, M. K. Yu, T. S. Lee, J. J. Park, Y. Y. Jeong, and S. Jon, "Amphiphilic polymer-coated hybrid nanoparticles as CT/MRI dual contrast agents," *Nanotechnology*, vol. 22, no. 15, Article ID 155101, 2011.
- [102] D. Huang, E. A. Swanson, C. P. Lin et al., "Optical coherence tomography," *Science*, vol. 254, no. 5035, pp. 1178–1181, 1991.
- [103] J. M. Schmitt, "Optical Coherence Tomography (OCT): a review," *IEEE Journal on Selected Topics in Quantum Electronics*, vol. 5, no. 4, pp. 1205–1215, 1999.
- [104] H. G. Bezerra, M. A. Costa, G. Guagliumi, A. M. Rollins, and D. I. Simon, "Intracoronary optical coherence tomography: a comprehensive review. Clinical and research applications," *JACC: Cardiovascular Interventions*, vol. 2, no. 11, pp. 1035–1046, 2009.
- [105] A. M. Gobin, M. H. Lee, N. J. Halas, W. D. James, R. A. Drezek, and J. L. West, "Near-infrared resonant nanoshells for combined optical imaging and photothermal cancer therapy," *Nano Letters*, vol. 7, no. 7, pp. 1929–1934, 2007.
- [106] H. Y. Tseng, C. K. Lee, S. Y. Wu et al., "Au nanorings for enhancing absorption and backscattering monitored with optical coherence tomography," *Nanotechnology*, vol. 21, no. 29, Article ID 295102, 2010.
- [107] A. S. Paranjape, R. Kuranov, S. Baranov et al., "Depth resolved photothermal OCT detection of macrophages in tissue using nanorose," *Biomedical Optics Express*, vol. 1, no. 1, pp. 2–16, 2010.
- [108] Y. Su, F. Zhang, K. Xu, J. Yao, and R. K. Wang, "A photoacoustic tomography system for imaging of biological tissues," *Journal of Physics D*, vol. 38, no. 15, pp. 2640–2644, 2005.
- [109] K. S. Valluru, B. K. Chinni, and N. A. Rao, "Photoacoustic imaging: opening new frontiers in medical imaging," *Journal of Clinical Imaging Science*, vol. 1, article 24, 2011.
- [110] X. Yang, S. E. Skrabalak, Z. Y. Li, Y. Xia, and L. V. Wang, "Photoacoustic tomography of a rat cerebral cortex in vivo with Au nanocages as an optical contrast agent," *Nano Letters*, vol. 7, no. 12, pp. 3798–3802, 2007.
- [111] M. Eghtedari, A. Oraevsky, J. A. Copland, N. A. Kotov, A. Conjusteau, and M. Motamedi, "High sensitivity of in vivo detection of gold nanorods using a laser optoacoustic imaging system," *Nano Letters*, vol. 7, no. 7, pp. 1914–1918, 2007.
- [112] K. H. Song, C. Kim, K. Maslov, and L. V. Wang, "Noninvasive in vivo spectroscopic nanorod-contrast photoacoustic mapping of sentinel lymph nodes," *European Journal of Radiology*, vol. 70, no. 2, pp. 227–231, 2009.
- [113] M. B. Mohamed, V. Volkov, S. Link, and M. A. El-Sayed, "The 'lightning' gold nanorods: fluorescence enhancement of over a million compared to the gold metal," *Chemical Physics Letters*, vol. 317, no. 6, pp. 517–523, 2000.
- [114] H. Wang, T. B. Huff, D. A. Zweifel et al., "In vitro and in vivo two-photon luminescence imaging of single gold nanorods," *Proceedings of the National Academy of Sciences of the United States of America*, vol. 102, no. 44, pp. 15752–15756, 2005.
- [115] G. T. Boyd, Z. H. Yu, and Y. R. Shen, "Photoinduced luminescence from the noble metals and its enhancement on roughened surfaces," *Physical Review B*, vol. 33, no. 12, pp. 7923–7936, 1986.
- [116] N. J. Durr, T. Larson, D. K. Smith, B. A. Korgel, K. Sokolov, and A. Ben-Yakar, "Two-photon luminescence imaging of cancer cells using molecularly targeted gold nanorods," *Nano Letters*, vol. 7, no. 4, pp. 941–945, 2007.
- [117] K. Imura, T. Nagahara, and H. Okamoto, "Plasmon mode imaging of single gold nanorods," *Journal of the American Chemical Society*, vol. 126, no. 40, pp. 12730–12731, 2004.
- [118] K. T. Yong, I. Roy, H. Ding, E. J. Bergey, and P. N. Prasad, "Biocompatible near-infrared quantum dots as ultrasensitive probes for long-term in vivo imaging applications," *Small*, vol. 5, no. 17, pp. 1997–2004, 2009.
- [119] A. M. Smith, H. Duan, A. M. Mohs, and S. Nie, "Bioconjugated quantum dots for in vivo molecular and cellular imaging," *Advanced Drug Delivery Reviews*, vol. 60, no. 11, pp. 1226–1240, 2008.
- [120] E. G. Soltesz, S. Kim, R. G. Laurence et al., "Intraoperative sentinel lymph node mapping of the lung using near-infrared fluorescent quantum dots," *Annals of Thoracic Surgery*, vol. 79, no. 1, pp. 269–277, 2005.
- [121] C. P. Parungo, Y. L. Colson, S. W. Kim et al., "Sentinel lymph node mapping of the pleural space," *Chest*, vol. 127, no. 5, pp. 1799–1804, 2005.
- [122] J. P. Zimmer, S. W. Kim, S. Ohnishi, E. Tanaka, J. V. Frangioni, and M. G. Bawendi, "Size series of small indium arsenide-zinc selenide core-shell nanocrystals and their application to in vivo imaging," *Journal of the American Chemical Society*, vol. 128, no. 8, pp. 2526–2527, 2006.
- [123] H. Kobayashi, Y. Hama, Y. Koyama et al., "Simultaneous multicolor imaging of five different lymphatic basins using quantum dots," *Nano Letters*, vol. 7, no. 6, pp. 1711–1716, 2007.
- [124] Y. Hama, Y. Koyama, Y. Urano, P. L. Choyke, and H. Kobayashi, "Simultaneous two-color spectral fluorescence lymphangiography with near infrared quantum dots to map two lymphatic flows from the breast and the upper extremity," *Breast Cancer Research and Treatment*, vol. 103, no. 1, pp. 23–28, 2007.
- [125] S. Kim, Y. T. Lim, E. G. Soltesz et al., "Near-infrared fluorescent type II quantum dots for sentinel lymph node mapping," *Nature Biotechnology*, vol. 22, no. 1, pp. 93–97, 2004.
- [126] Y. T. Lim, S. Kim, A. Nakayama, N. E. Stott, M. G. Bawendi, and J. V. Frangioni, "Selection of quantum dot wavelengths for biomedical assays and imaging," *Molecular Imaging*, vol. 2, no. 1, pp. 50–64, 2003.
- [127] J. D. Smith, G. W. Fisher, A. S. Waggoner, and P. G. Campbell, "The use of quantum dots for analysis of chick CAM vasculature," *Microvascular Research*, vol. 73, no. 2, pp. 75–83, 2007.
- [128] D. R. Larson, W. R. Zipfel, R. M. Williams et al., "Water-soluble quantum dots for multiphoton fluorescence imaging in vivo," *Science*, vol. 300, no. 5624, pp. 1434–1436, 2003.
- [129] X. Yu, L. Chen, K. Li et al., "Immunofluorescence detection with quantum dot bioconjugates for hepatoma in vivo," *Journal of Biomedical Optics*, vol. 12, no. 1, Article ID 014008, 2007.
- [130] H. Tada, H. Higuchi, T. M. Wanatabe, and N. Ohuchi, "In vivo real-time tracking of single quantum dots conjugated with monoclonal anti-HER2 antibody in tumors of mice," *Cancer Research*, vol. 67, no. 3, pp. 1138–1144, 2007.
- [131] M. E. Åkerman, W. C. W. Chan, P. Laakkonen, S. N. Bhatia, and E. Ruoslahti, "Nanocrystal targeting in vivo," *Proceedings*

- of the National Academy of Sciences of the United States of America, vol. 99, no. 20, pp. 12617–12621, 2002.
- [132] X. Gao, Y. Cui, R. M. Levenson, L. W. K. Chung, and S. Nie, “In vivo cancer targeting and imaging with semiconductor quantum dots,” *Nature Biotechnology*, vol. 22, no. 8, pp. 969–976, 2004.
- [133] X. Huang, P. K. Jain, I. H. El-Sayed, and M. A. El-Sayed, “Determination of the minimum temperature required for selective photothermal destruction of cancer cells with the use of immunotargeted gold nanoparticles,” *Photochemistry and Photobiology*, vol. 82, no. 2, pp. 412–417, 2006.
- [134] J. Chen, D. Wang, J. Xi et al., “Immuno gold nanocages with tailored optical properties for targeted photothermal destruction of cancer cells,” *Nano Letters*, vol. 7, no. 5, pp. 1318–1322, 2007.
- [135] Y. Haba, C. Kojima, A. Harada, T. Ura, H. Horinaka, and K. Kono, “Preparation of poly(ethylene glycol)-modified poly(amido amine) dendrimers encapsulating gold nanoparticles and their heat-generating ability,” *Langmuir*, vol. 23, no. 10, pp. 5243–5246, 2007.
- [136] D. K. Kirui, D. A. Rey, and C. A. Batt, “Gold hybrid nanoparticles for targeted phototherapy and cancer imaging,” *Nanotechnology*, vol. 21, no. 10, Article ID 105105, 2010.
- [137] X. Huang, I. H. El-Sayed, W. Qian, and M. A. El-Sayed, “Cancer cell imaging and photothermal therapy in the near-infrared region by using gold nanorods,” *Journal of the American Chemical Society*, vol. 128, no. 6, pp. 2115–2120, 2006.
- [138] X. Huang, I. H. El-Sayed, and M. A. El-Sayed, “Applications of gold nanorods for cancer imaging and photothermal therapy,” *Methods in Molecular Biology*, vol. 624, pp. 343–357, 2010.
- [139] W. S. Kuo, C. N. Chang, Y. T. Chang et al., “Gold nanorods in photodynamic therapy, as hyperthermia agents, and in near-infrared optical imaging,” *Angewandte Chemie - International Edition*, vol. 49, no. 15, pp. 2711–2715, 2010.
- [140] B. Van De Broek, N. Devoogdt, A. Dhollander et al., “Specific cell targeting with nanobody conjugated branched gold nanoparticles for photothermal therapy,” *ACS Nano*, vol. 5, no. 6, pp. 4319–4328, 2011.
- [141] L. R. Hirsch, R. J. Stafford, J. A. Bankson et al., “Nanoshell-mediated near-infrared thermal therapy of tumors under magnetic resonance guidance,” *Proceedings of the National Academy of Sciences of the United States of America*, vol. 100, no. 23, pp. 13549–13554, 2003.
- [142] C. Loo, L. Hirsch, M. H. Lee et al., “Gold nanoshell bioconjugates for molecular imaging in living cells,” *Optics Letters*, vol. 30, no. 9, pp. 1012–1014, 2005.
- [143] C. Loo, A. Lowery, N. Halas, J. West, and R. Drezek, “Immunotargeted nanoshells for integrated cancer imaging and therapy,” *Nano Letters*, vol. 5, no. 4, pp. 709–711, 2005.
- [144] X. Huang, P. K. Jain, I. H. El-Sayed, and M. A. El-Sayed, “Plasmonic photothermal therapy (PPTT) using gold nanoparticles,” *Lasers in Medical Science*, vol. 23, no. 3, pp. 217–228, 2008.
- [145] S. B. Brown and S. H. Ibbotson, “Photodynamic therapy and cancer,” *BMJ*, vol. 339, Article ID b2459, 2009.
- [146] J. Cadet, “The photodynamic therapy of cancer cells,” *Photochemistry and photobiology*, vol. 87, no. 1, p. 1, 2011.
- [147] A. Lin and S. M. Hahn, “Photodynamic therapy: a light in the darkness?” *Clinical Cancer Research*, vol. 15, no. 13, pp. 4252–4253, 2009.
- [148] M. A. MacCormack, “Photodynamic therapy,” *Advances in Dermatology*, vol. 22, pp. 219–258, 2006.
- [149] P. Zhang, W. Steelant, M. Kumar, and M. Scholfield, “Versatile photosensitizers for photodynamic therapy at infrared excitation,” *Journal of the American Chemical Society*, vol. 129, no. 15, pp. 4526–4527, 2007.
- [150] B. Ungun, R. K. Prud’homme, S. J. Budijono et al., “Nanofabricated upconversion nanoparticles for photodynamic therapy,” *Optics Express*, vol. 17, no. 1, pp. 80–86, 2009.
- [151] D. K. Chatterjee and Z. Yong, “Upconverting nanoparticles as nanotransducers for photodynamic therapy in cancer cells,” *Nanomedicine*, vol. 3, no. 1, pp. 73–82, 2008.
- [152] H. S. Qian, H. C. Guo, P. C. L. Ho, R. Mahendran, and Y. Zhang, “Mesoporous-silica-coated up-conversion fluorescent nanoparticles for photodynamic therapy,” *Small*, vol. 5, no. 20, pp. 2285–2290, 2009.

Research Article

Mannan-Modified PLGA Nanoparticles for Targeted Gene Delivery

Fansheng Kong, Linfu Ge, Ximin Liu, Ning Huang, and Fang Zhou

Department of Hematology, General Hospital of Ji'nan Command, PLA, 25 Shifan Road, Ji'nan 250031, China

Correspondence should be addressed to Fang Zhou, zhoufangphd@yahoo.com.cn

Received 28 April 2011; Revised 28 May 2011; Accepted 15 June 2011

Academic Editor: Rodica-Mariana Ion

Copyright © 2012 Fansheng Kong et al. This is an open access article distributed under the Creative Commons Attribution License, which permits unrestricted use, distribution, and reproduction in any medium, provided the original work is properly cited.

The studies of targeted gene delivery nanocarriers have gained increasing attention during the past decades. In this study, mannan modified DNA loaded bioadhesive PLGA nanoparticles (MAN-DNA-NPs) were investigated for targeted gene delivery to the Kupffer cells (KCs). Bioadhesive PLGA nanoparticles were prepared and subsequently bound with *pEGFP*. Following the coupling of the mannan-based PE-grafted ligands (MAN-PE) with the DNA-NPs, the MAN-DNA-NPs were delivered intravenously to rats. The transfection efficiency was determined from the isolated KCs and flow cytometry was applied for the quantitation of gene expression after 48 h post transfection. The size of the MAN-DNA-NPs was found to be around 190 nm and the Zeta potential was determined to be -15.46mV . The *pEGFP* binding capacity of MAN-DNA-NPs was $(88.9 \pm 5.8)\%$ and the *in vitro* release profiles of the MAN-DNA-NPs follow the Higuchi model. When compared with non-modified DNA-NPs and Lipofectamine 2000-DNA, MAN-DNA-NPs produced the highest gene expressions, especially *in vivo*. The *in vivo* data from flow cytometry analysis showed that MAN-DNA-NPs displayed a remarkably higher transfection efficiency (39%) than non-modified DNA-NPs (25%) and Lipofectamine 2000-DNA (23%) in KCs. The results illustrate that MAN-DNA-NPs have the ability to target liver KCs and could function as promising active targeting drug delivery vectors.

1. Introduction

Biodegradable nanoparticles have been used frequently as gene delivery vehicles due to their extensive bioavailability, better encapsulation, high stability, and minimal toxicity [1]. They can be tailor made to achieve both controlled drug release and tumor targeting by tuning the polymer characteristics and shaping the surface through nanoengineering [2]. A number of different polymers, both synthetic and natural, have been utilized in formulating biodegradable nanoparticles [3–5]. One of the most extensively investigated polymers for nanoparticles is the biodegradable and biocompatible poly(D,L-lactide-co-glycolide) (PLGA), which has been approved by the FDA for certain human clinical uses [6].

Active targeting is a noninvasive approach to transport drugs and genes to target sites with the help of site-specific ligands [7]. Nanocarriers with active targeting properties

could potentially be delivered to specific organs, tissues, cells, or even cellular organelles. Various kinds of targeting residues such as antibodies, peptides, and saccharides have been applied towards the modification of nanocarriers to achieve active targeting [8, 9]. Nanocarriers modified with saccharides, have seen advancement due to their high specificity, low toxicity, and low immunogenicity. Recently, bioadhesive PLGA nanoparticles were established as promising drug delivery systems [6, 10], and mannan-based PE-grafted ligands (MAN-PEs) were synthesized and applied for the surface modification of nanocarriers to achieve active targeting [11]. In this study, MAN-PE-modified bioadhesive PLGA nanoparticles were investigated as active targeting gene delivery system using plasmid enhanced green fluorescent protein (*pEGFP*) as the model gene.

In the present study, MAN-PEs were applied for the surface modification of PLGA nanoparticles to achieve active targeting to the liver. *In vitro* and *in vivo* behavior

of mannan-modified DNA-loaded PLGA nanoparticles was investigated in comparison with nonmodified DNA-loaded PLGA nanoparticles.

2. Materials and Methods

2.1. Materials. Poly(D,L-lactic-co-glycolic) (PLGA, 50:50, Av.MW 25,000) was obtained from Shandong Institute of Medical Instrument (China). Mannan and L- α -phosphatidylethanolamine (PE) were purchased from Sigma-Aldrich Co. (USA). *pEGFP-N1* was provided by Shandong University (China). PicoGreen reagent and Lipofectamine 2000 were obtained from Invitrogen Corporation (USA). MTT (3-[4,5-dimethyl-2-thiazolyl]-2,5-diphenyl-2H-tetrazolium bromide) was purchased from Sigma-Aldrich (China). All other chemicals were of analytical grade or higher.

2.2. Animals. Adult male Sprague-Dawley rats (10-to-15-week old) were purchased from the Medical Animal Test Center of Shandong Province and housed under standard laboratory conditions. All animal experiments complied with the requirements of the National Act on the Use of Experimental Animals (People's Republic of China).

2.3. Preparation of Bioadhesive PLGA Nanoparticles. Bioadhesive PLGA nanoparticles (NPs) were prepared following the methods described by Zou et al. [6, 10]. Carbopol 940 (CP) was dispersed in distilled water at room temperature and left overnight to swell. Neutralization of the CP dispersion was achieved by adding the required amount of 1 M NaOH until pH 7.0 was reached. The resulting CP stock solution was diluted with distilled water to afford a 0.02% (w/v) CP solution. Bioadhesive PLGA nanoparticles were prepared under optimized conditions by a nanoprecipitation method (solvent displacement technique) [12, 13]. 50 mg of PLGA polymer was accurately weighted and dissolved in 3 mL acetone. The organic phase was added dropwise into the 0.02% CP solution being stirred at 600 rpm and room temperature. When complete evaporation of the organic solvent had occurred, the redundant stabilizers and the nanoparticles were separated by ultracentrifugation at 1000 g, 4°C for 20 min. The pellet was resuspended in Milli-Q water, washed three times, and filtered through a 0.45 μ m membrane. The resulting nanoparticle suspensions were stored at 4°C until use.

2.4. Fabrication of DNA-Loaded Nanoparticles. The reporter gene *pEGFP* was mixed with the PLGA nanoparticles by vortexing the nanoparticle suspension with a 1 mg/mL solution of DNA for 20 s. Incubation of the mixture for 30 min at RT facilitated the formation of the DNA-loaded PLGA nanoparticles (DNA-NPs).

2.5. Surface Modification of DNA-NPs with Mannan-PE. Mannan-PE was synthesized in accordance with the method described by Yu et al. [11]. Surface modification of DNA-NPs with mannan-PE ligands was accomplished according to the

procedure developed by Vyas et al. [14]. Mannan-PE ligands were dissolved in 5 mL of phosphate buffered saline (PBS, pH 7.4). Then, the solution was added at dropwise into 10 mL of DNA-NPs that were stirred at 800 rpm by a laboratory magnetic stirrer at RT. The suspension was continually stirred at 600 rpm until the completion of modification. The excessive nonmodified ligands were removed by spinning the resultant suspension through a Sephadex G-50 column at 2,000 rpm for 5 min. The pellet was resuspended in Milli-Q water, washed three times, and filtered through a 0.80 μ m membrane to obtain the desired mannan-modified DNA-loaded PLGA nanoparticles (MAN-DNA-NPs).

As a result of the modification process, the hydrophobic PE domains coated the surface of bioadhesive DNA-NPs, masking the inherent charge on the carriers. The total ligand-to-carrier weight ratio was optimized by measuring the change in Zeta potential. The optimum ratio was found to occur when increasing the ligand-to-carrier weight ratio resulted in no significant change in Zeta potential.

2.6. Characterization of MAN-DNA-NPs and DNA-NPs. The surface morphologies of both the MAN-DNA-NPs and the nonmodified DNA-NPs were examined by transmission electronic microscopy (TEM). The mean particle size and Zeta potential of the NPs were analyzed by photon correlation spectroscopy (PCS) and laser Doppler anemometry, respectively.

PicoGreen-fluorometry assay was carried out to measure the adsorption efficiency of the DNA loaded NPs [9, 15]. The *pEGFP* was isolated from the MAN-DNA-NPs and DNA-NPs by centrifugation at 1000 g, 4°C for 20 min. Analysis of the *pEGFP* containing supernatants by a fluorescence spectrophotometer afforded the concentration of plasmid DNA.

2.7. In Vitro DNA Release Studies. The MAN-DNA-NPs and DNA-NPs were placed in phosphate buffered solution (PBS, pH 7.4) to characterize the DNA release profile [16]. Typically, aliquots of complexes (equivalent to 1 μ g DNA) were suspended in Eppendorf tubes containing 1 mL of PBS and vortexed. The tubes were continuously shaken in a 37°C water bath at 100 rpm. Separate tubes were used for each data point. At predetermined time intervals, the nanoparticle suspensions were centrifuged (1000 g, 4°C for 20 min) and the amount of DNA released in the supernatant was analyzed by the PicoGreen assay mentioned above. Background readings were obtained using the supernatants from the blank PLGA-NPs.

2.8. Isolation and Culture of Kupffer Cells. Kupffer cells (KCs) were isolated from SD rats under pentobarbitone anaesthesia [17–20]. The rats' portal vein were cannulated and perfused with HBSS for 10 min at RT. During this time, the liver was excised and the perfusate discarded. The liver was then perfused with 0.2% pronase (60 mL at RT) which was discarded. Then, the liver was perfused with a recirculating solution of 0.05% pronase and 0.05% collagenase (60 mL at RT) until the liver was digested as judged by the softening of the liver parenchyma beneath the capsule. The liver was then cut into

small pieces, suspended in 100 mL solution containing 0.02% pronase, 0.05% collagenase, and 0.005% DNase, and agitated at RT for 20 min. Following digestion, the liver homogenate was filtered through sterile gauze and centrifuged (1000 g, 4°C for 10 min). The supernatant was removed and the pellet resuspended in 10 mL Percoll gradient. Aliquots (5 mL) of this cell suspension were added to 5 mL aliquots of Percoll gradient. These were carefully overlaid with 5 mL HBSS and centrifuged at 1000 g, 4°C for 20 min. The nonparenchymal cell-enriched layer observed at the interface between the two layers was carefully harvested and diluted with 10 mL of HBSS. The suspension was then centrifuged (1000 g, 4°C for 20 min) to precipitate the KCs, which were then seeded into a 96-well microtiter plate at a density of 2×10^4 cells/well in 200 μ L RPMI 1640 supplemented with 10% fetal bovine serum (FBS) and antibiotics. After incubation at 37°C for 2 h under 5% CO₂ atmosphere, the culture medium was replaced by 200 μ L fresh RPMI 1640 to yield the purified KCs.

2.9. In Vitro Cytotoxicity Evaluation and Transfection Analysis.

The *in vitro* cytotoxicity of MAN-NPs was evaluated by MTT assay [21] in the above cultured KCs. After incubation at 37°C for 24 h under 5% CO₂ atmosphere, the culture medium was replaced with 200 μ L of fresh RPMI 1640 containing various concentrations of the MAN-NPs or Lipofectamine 2000 for comparison, and the cells were incubated for another 24 h. The cell viability was then assessed by MTT assay. 5 mg/mL of MTT in PBS was then added to each well, and the plate was incubated for an additional 4 h at 37°C under the aforementioned 5% CO₂ atmosphere. Then, the MTT containing medium was removed, and the crystals formed by living cells were dissolved in 100 μ L DMSO. The absorbance at 570 nm was determined by a microplate reader. Untreated cells were taken as a control with 100% viability, and cells without the addition of MTT were used as a blank to calibrate the spectrophotometer to zero absorbance. The relative cell viability (%) compared to control cells was calculated using $(\text{Abs}_{\text{sample}}/\text{Abs}_{\text{control}}) \times 100$.

For transfection efficiency analysis, the KCs were seeded into 24-well plates at a density of 1×10^5 cells/well in 1 mL of RPMI-1640 with 10% FBS, 24 h prior to transfection. When the cells were at about 80% confluence, the media was replaced with 200 μ L serum-free media containing MAN-DNA-NPs and DNA-NPs. Naked DNA was used as a negative control. Lipofectamine 2000 was used as a positive control. The original incubation medium was replaced with 1 mL of complete medium after incubation at 37°C for 4 h under a 5% CO₂ atmosphere. The cells were incubated and were studied every 12 h until 48 h after transfection. The fluorescent cells were observed using an inversion fluorescence microscope, at which time pictures were taken for the record.

2.10. In Vivo Delivery and Transfection. Adult male Sprague-Dawley rats (10-to-15-week old) were divided into five groups (six rats in each group) and injected intravenously with 1 mL of both MAN-DNA-NPs and DNA-NPs. Identical intravenous doses of blank NPs, naked *pEGFP*, and Lipofectamine 2000-DNA served as controls. At predetermined time

TABLE 1: Particle size and Zeta potential of NPs, DNA-NPs, and MAN-DNA-NPs (mean \pm SD, $n = 3$).

Sample	Mean particle size (nm)	Polydispersity index (PDI)	Zeta potential (mV)
NPs	116.7 \pm 3.2	0.19 \pm 0.05	-29.18 \pm 3.54
DNA-NPs	145.3 \pm 8.7	0.23 \pm 0.08	-36.58 \pm 1.32
MAN-DNA-NPs	189.7 \pm 5.3	0.15 \pm 0.07	-15.46 \pm 1.09

intervals, the rats' KCs were isolated under pentobarbitone anaesthesia as described in Section 2.8. The KCs were then seeded into 24-well plates in 1 mL of RPMI 1640 with 10% FBS. The fluorescent cells were observed using an inversion fluorescence microscope, and the pictures were captured.

For further quantitation of the transfection efficiency, flow cytometry was used. Cells were washed with 1 mL of PBS (100 g, 4°C for 5 min) and were detached with trypsin/EDTA. The supernatant was discarded and resuspended with 300 μ L of PBS, mixed well, and added into the flow cytometer to determine the amount of KCs which has been successfully transfected.

2.11. Statistical Analysis. All studies were repeated a minimum of three times and all measurements were carried out in triplicate. Results were reported as means \pm SD (SD = standard deviation). Statistical significance was analyzed using the Student's *t*-test. Differences between experimental groups were considered significant when the *P* value was less than 0.05 ($P < 0.05$).

3. Results

3.1. Characterization of DNA Loaded NPs. The transmission electron micrograph (TEM) pictures of the MAN-DNA-NPs and DNA-NPs were shown in Figure 1. DNA-NPs had spherical shapes (Figure 1(a)) while the MAN-DNA-NPs had dark coats on the white particles (Figure 1(b)). Mean particle size, polydispersity index (PDI), Zeta potential of blank PLGA nanoparticles (NPs), DNA-NPs, and MAN-DNA-NPs were characterized and summarized in Table 1.

To optimize the mannan-PE to DNA-NPs weight ratio, the change in Zeta potential was measured and the optimum ratio was obtained when no significant change in Zeta potential was observed after increasing the mannan-PE percent. The optimum ratio was obtained at 1/2 (mannan-PE/DNA-NPs, w/w) (Figure 2).

3.2. Gene Loading Capacity and In Vitro Release Studies. PicoGreen fluorometry assay was carried out to quantitate the loading efficiencies of the gene delivery systems. DNA binding quantity (%) = (total amount of DNA - the amount of free DNA)/total amount of DNA \times 100. The *pEGFP* binding capacities of MAN-DNA-NPs and DNA-NPs were (88.9 \pm 5.8)% and (89.5 \pm 4.5)%, respectively.

The *in vitro* release profiles of modified and nonmodified DNA-NPs are illustrated in Figure 3 and the release behavior of the MAN-DNA-NPs and DNA-NPs follow the Higuchi model best.

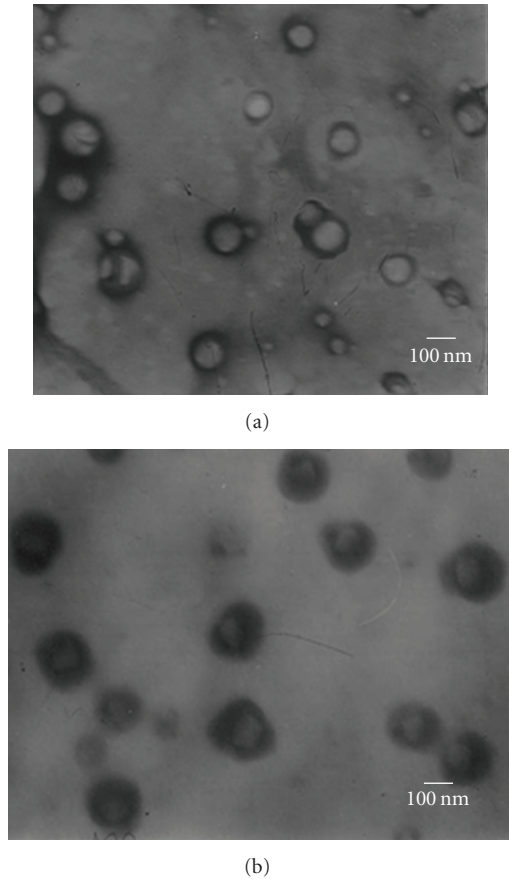


FIGURE 1: TEM imaging of DNA-NPs (a) and MAN-DNA-NPs (b).

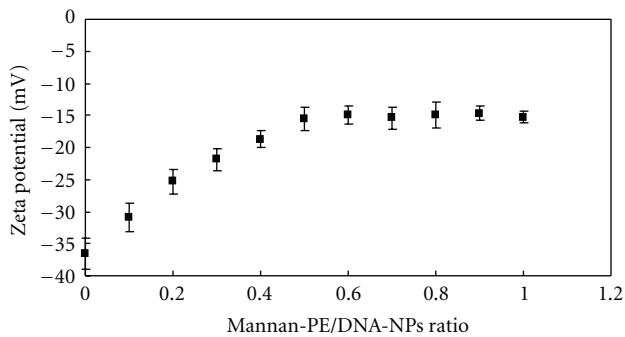


FIGURE 2: Optimization of mannan-modified DNA-NPs: MAN-PEs to DNA-NPs weight ratio (w/w).

3.3. *In Vitro* Cytotoxicity and Transfection. The isolated Kupffer cells were defined on the basis of the presence of phagocytosis of latex beads and/or positive immunostaining with antibody to the epitope ED2. With the above-mentioned method, about 81.52×10^6 /rat liver Kupffer cells were obtained, purity was around 92% (to 88.69×10^6 /rat liver NPC), and more than 95% cells were alive. The isolated and purified rat Kupffer cells retained their *in vivo* morphological, biological and immunological characteristics.

In vitro toxicity of modified and nonmodified NPs was evaluated by MTT assay in rat KCs. The cytotoxicity of

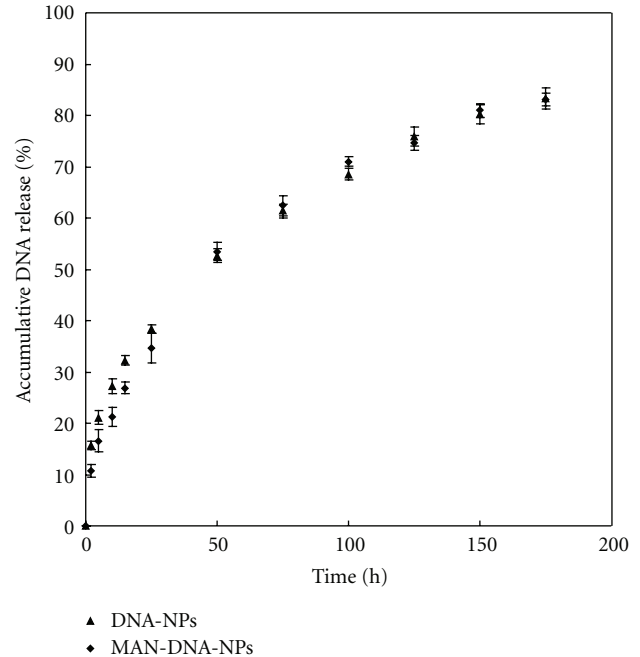


FIGURE 3: *In vitro* release profile of MAN-DNA-NPs and DNA-NPs (mean \pm SD, $n = 3$).

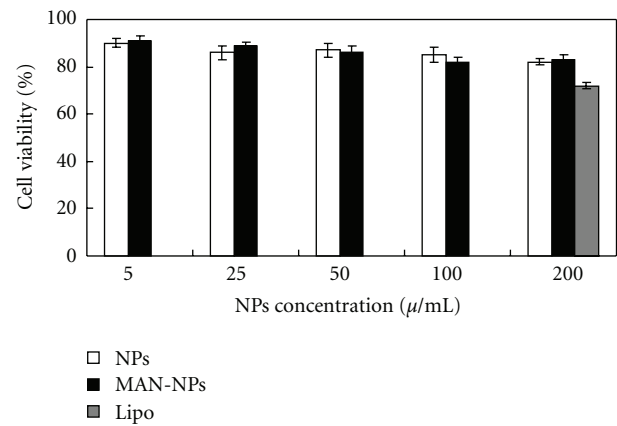
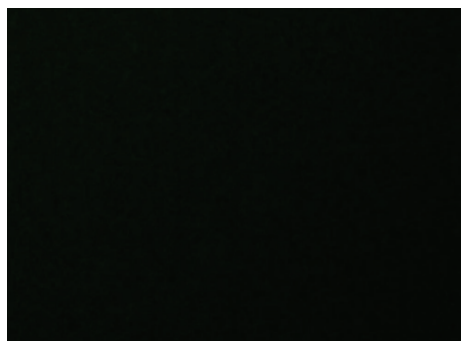


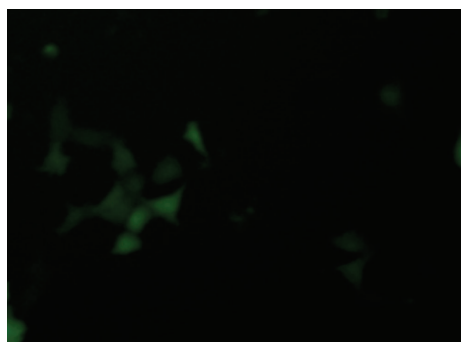
FIGURE 4: Cell viabilities of MAN-DNA-NPs and DNA-NPs (mean \pm SD, $n = 3$).

MAN-NPs and NPs at various concentrations (5, 25, 50, 100, and 200 $\mu\text{g/mL}$) was evaluated. Lipofectamine 2000 at the concentration of transfection was used as comparison. The cell viabilities in the presence of NPs and MAN-NPs over the studied concentration range (5–200 $\mu\text{g/mL}$) were between 80 and 120% compared with controls (Figure 4). MAN-NPs and NPs exhibited a lower cytotoxicity than Lipofectamine 2000 at all concentrations ($P < 0.05$).

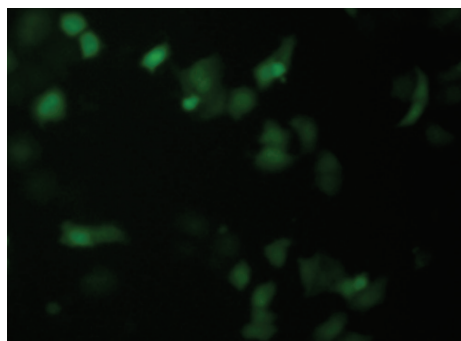
The *in vitro* transfection efficiencies of MAN-DNA-NPs and DNA-NPs in KCs after 48 h of transfection are shown in Figure 5. When compared with naked DNA, DNA-NPs, and Lipofectamine-DNA, MAN-DNA-NPs had higher transfection efficiency.



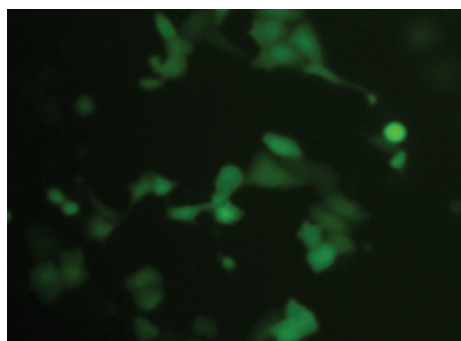
(a)



(b)



(c)



(d)

FIGURE 5: Fluorescent micrographs of KCs transfected by plasmid EGFP with DNA-NPs (c) and MAN-DNA-NPs (d). The KCs transfected by naked DNA (a), and Lipofectamine-DNA (b) was used as control.

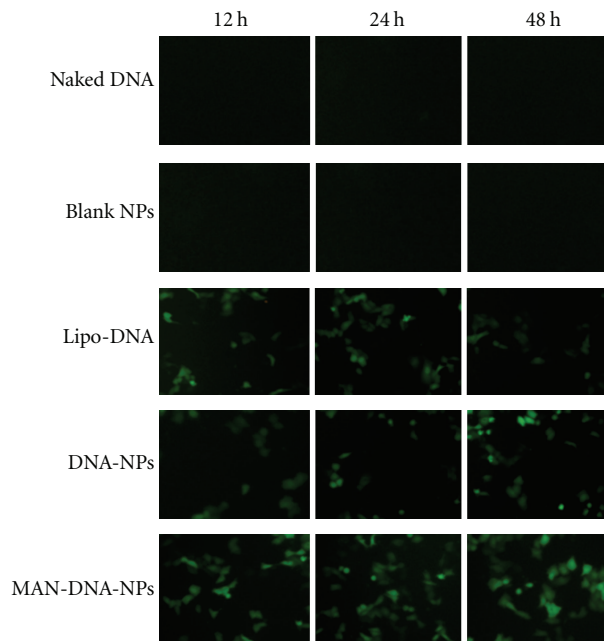


FIGURE 6: Fluorescent micrographs of KCs transfected by plasmid EGFP *in vivo*. Gene expression was examined after 12, 24 and 48 h post injection.

3.4. *In Vivo Gene Delivery in Rats.* After intravenous injection of naked DNA, blank NPs, Lipofectamine 2000-DNA, DNA-NPs, and MAN-DNA-NPs, the KCs were isolated at 12 h, 24 h, and 48 h. The fluorescent cells were observed using an inverted fluorescence microscope (Figure 6). The pictures apparently showed that MAN-DNA-NPs had better transfection efficiency in rats compared with nonmodified DNA-NPs and Lipofectamine 2000-DNA. Flow cytometry was applied for the further quantitation of gene expression after 48 h following transfection. As shown in Figure 7, the percentage of KCs transfected with *pEGFP* appeared at the UR and LR quadrants, MAN-DNA-NPs displayed a remarkably higher transfection efficiency than nonmodified DNA-NPs ($P < 0.05$) and Lipofectamine 2000-DNA ($P < 0.05$) in KCs.

4. Discussion

In the present study, novel mannan-modified bioadhesive PLGA nanocarriers were constructed as active targeting gene delivery system. As illustrated in Figure 1 and Table 1, nonmodified DNA-NPs had spherical shapes while the mannan-modified MAN-DNA-NPs had a dark coat on the white balls, which may be employed to identify the successful coating of mannan-PE. The mean particle size of NPs was around 100–200 nm, which is ideal for the nanoparticulate system.

During the modification procedure, mannan containing ligands were extensively coated onto the DNA-NPs' surface, which covered their original charge and caused the change in Zeta potential. The optimization of ligand-to-carrier ratio was carried out by measure the Zeta potential. The optimum ratio was obtained at 1/2 (mannan-PE/DNA-NPs, w/w)

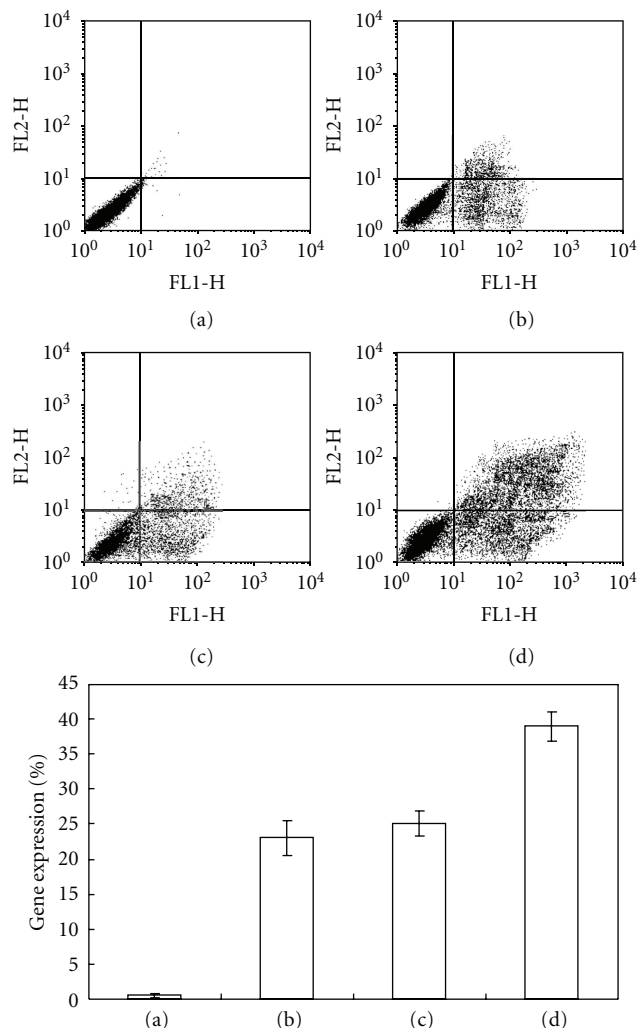


FIGURE 7: Flow cytometry analysis of KCs transfected by plasmid EGFP *in vivo*. Gene expression was examined after 48 h following injection. (a) Naked DNA, (b) Lipofectamine-DNA, (c) DNA-NPs, and (d) MAN-DNA-NPs (mean \pm SD, $n = 3$).

(Figure 2) and the optimum MAN-DNA-NPs had a Zeta potential of -15.46 mV (Table 1).

PicoGreen fluorometry method was applied to quantitate the loading capacity and *in vitro* release behavior of MAN-DNA-NPs. The binding efficiency of MAN-DNA-NPs and DNA-NPs was 88.9% and 89.5%, which had no significant difference. The results demonstrated that binding of mannan containing ligand onto the NPs surface did not detach the DNA from the complexes. The *in vitro* release profiles (Figure 3) of MAN-DNA-NPs and DNA-NPs were nearly identical. These findings support the notion that the coating of mannan did not hinder the release of DNA. The release profiles of the MAN-DNA-NPs and DNA-NPs both follow the Higuchi model, MAN-DNA-NPs: $Q\% = 0.0654t^{1/2} + 0.0206$, $r = 0.9952$; DNA-NPs: $Q\% = 0.063t^{1/2} + 0.05848$, $r = 0.9958$.

Macrophages play a major role in the immune response to foreign antigens, targeting macrophages is one of the important therapeutic ways to treat genetic metabolic diseases

such as Gaucher's disease and human immunodeficiency virus (HIV) infection [22]. KCs are liver-specific resident macrophages that play an integral part in the physiological homeostasis of the liver. Kupffer cells have significant roles in acute and chronic responses of the liver to bacterial and viral infections, toxic or carcinogenic attack, as well as mediating hepatotoxicity [23]. In this study, rat KCs were isolated and used as model cells for *in vitro* toxicity and transfection evaluation. For cell viability study, both MAN-NPs and blank NPs showed lower cytotoxicity compared with Lipofectamine 2000 ($P < 0.05$, Figure 4), most probably due to the better biodegradability and bioavailability. The *in vitro* transfection of MAN-DNA-NPs and DNA-NPs was carried on KCs (Figure 6). After transfection for 48 h, MAN-DNA-NPs gained better transfection results than DNA-NPs, which may be explained by the sugar-lectin-mediated active targeting mechanism. The modified *pEGFP* loaded NPs were bound to the KCs and delivered the DNA into the cells to express EGFP.

The *in vivo* gene delivery and expression studies were applied in rats. After intravenous injection, the KCs were isolated, cultured, and analyzed with fluorescence microscope and flow cytometer. As shown in Figure 6, MAN-DNA-NPs achieved the best transfection efficacy in every data point. For further quantitation of the fluorescent KCs, flow cytometry was applied and the KCs with green fluorescence appeared at the UR and LR quadrants (Figure 7). The modified MAN-DNA-NPs showed higher transfection efficiency in rats compared with nonmodified DNA-NPs and Lipofectamine 2000-DNA ($P < 0.05$) which demonstrates that the mannan modified PLGA NPs had the ability to target liver KCs and could function as promising active targeting drug delivery vectors.

5. Conclusions

In conclusion, MAN-PEs-modified *pEGFP*-loaded bioadhesive PLGA-NPs could be targeted delivered to the liver and successfully transfected the KCs. This may be explained by the sugar-lectin-mediated active targeting mechanism. The results indicate that this kind of modification could be generalized to other kinds of nanocarriers and construct many kinds of active targeting drug delivery systems.

Acknowledgment

The authors thank Dr. Sebastian Temme (Department of Chemistry, Brandeis University) for language editing of the paper.

References

- [1] A. Kumari, S. K. Yadav, and S. C. Yadav, "Biodegradable polymeric nanoparticles based drug delivery systems," *Colloids and Surfaces B*, vol. 75, no. 1, pp. 1–18, 2010.
- [2] D. B. Shenoy and M. M. Amiji, "Poly(ethylene oxide)-modified poly(epsilon-caprolactone) nanoparticles for targeted delivery of tamoxifen in breast cancer," *International Journal of Pharmaceutics*, vol. 293, no. 1-2, pp. 261–270, 2005.

- [3] S. M. Moghimi, A. C. Hunter, and J. C. Murray, "Long-circulating and target-specific nanoparticles: theory to practice," *Pharmacological Reviews*, vol. 53, no. 2, pp. 283–318, 2001.
- [4] K. S. Soppimath, T. M. Aminabhavi, A. R. Kulkarni, and W. E. Rudzinski, "Biodegradable polymeric nanoparticles as drug delivery devices," *Journal of Controlled Release*, vol. 70, no. 1-2, pp. 1–20, 2001.
- [5] J. Panyam and V. Labhasetwar, "Biodegradable nanoparticles for drug and gene delivery to cells and tissue," *Advanced Drug Delivery Reviews*, vol. 55, no. 3, pp. 329–347, 2003.
- [6] W. Zou, C. Liu, Z. Chen, and N. Zhang, "Studies on bioadhesive PLGA nanoparticles: a promising gene delivery system for efficient gene therapy to lung cancer," *International Journal of Pharmaceutics*, vol. 370, no. 1-2, pp. 187–195, 2009.
- [7] A. Beduneau, P. Saulnier, and J. P. Benoit, "Active targeting of brain tumors using nanocarriers," *Biomaterials*, vol. 28, no. 33, pp. 4947–4967, 2007.
- [8] W. Y. Yu and N. Zhang, "Surface modification of nanocarriers for cancer therapy," *Current Nanoscience*, vol. 5, no. 2, pp. 123–134, 2009.
- [9] W. Yu, N. Zhang, and C. Li, "Saccharide modified pharmaceutical nanocarriers for targeted drug and gene delivery," *Current Pharmaceutical Design*, vol. 15, no. 32, pp. 3826–3836, 2009.
- [10] W. Zou, G. Cao, Y. Xi, and N. Zhang, "New approach for local delivery of rapamycin by bioadhesive PLGA-carbopol nanoparticles," *Drug Delivery*, vol. 16, no. 1, pp. 15–23, 2009.
- [11] W. Yu, C. Liu, Y. Liu, N. Zhang, and W. Xu, "Mannan-modified solid lipid nanoparticles for targeted gene delivery to alveolar macrophages," *Pharmaceutical Research*, vol. 27, no. 8, pp. 1584–1596, 2010.
- [12] H. Fessi, F. Piusieux, J. P. Devissaguet, N. Ammoury, and S. Benita, "Nanocapsule formation by interfacial polymer deposition following solvent displacement," *International Journal of Pharmaceutics*, vol. 55, no. 1, pp. R1–R4, 1989.
- [13] U. Bilati, E. All'emann, and E. Doelker, "Development of a nanoprecipitation method intended for the entrapment of hydrophilic drugs into nanoparticles," *European Journal of Pharmaceutical Sciences*, vol. 24, no. 1, pp. 67–75, 2005.
- [14] S. P. Vyas, V. Sihorkar, and S. Jain, "Mannosylated liposomes for bio-film targeting," *International Journal of Pharmaceutics*, vol. 330, no. 1-2, pp. 6–13, 2007.
- [15] S. J. Ahn, J. Costa, and J. R. Emanuel, "PicoGreen quantitation of DNA: effective evaluation of samples pre- or post-PCR," *Nucleic Acids Research*, vol. 24, no. 16, pp. 2623–2635, 1996.
- [16] J. Ye, A. Wang, C. Liu, Z. Chen, and N. Zhang, "Anionic solid lipid nanoparticles supported on protamine/DNA complexes," *Nanotechnology*, vol. 19, no. 28, Article ID 285708, 2008.
- [17] J. K. Olynyk and S. L. Clarke, "Isolation and primary culture of rat Kupffer cells," *Journal of Gastroenterology and Hepatology*, vol. 13, no. 8, pp. 842–845, 1998.
- [18] H. Liu, H. Cao, and Z. Y. Wu, "Isolation of Kupffer cells and their suppressive effects on T lymphocyte growth in rat orthotopic liver transplantation," *World Journal of Gastroenterology*, vol. 13, no. 22, pp. 3133–3136, 2007.
- [19] Z. Zeng, H. Huang, F. Song, and J. Duan, "Isolation of rat Kupffer cells by ex vivo perfusion and their primary culture," *Shijie Huaren Xiaohua Zazhi*, vol. 17, pp. 2550–2554, 2009.
- [20] F. Liu, J. Y. Zhu, T. Li, and X. S. Leng, "Improving the ways to isolate, cultivate and identify rat Kupffer cells," *Zhonghua Gan Zang Bing Za Zhi*, vol. 14, no. 7, pp. 532–535, 2006.
- [21] Y. Gao, W. Gu, L. Chen, Z. Xu, and Y. Li, "A multifunctional nano device as non-viral vector for gene delivery: in vitro characteristics and transfection," *Journal of Controlled Release*, vol. 118, no. 3, pp. 381–388, 2007.
- [22] M. Yamada, M. Nishikawa, S. Kawakami et al., "Tissue and intrahepatic distribution and subcellular localization of a mannosylated lipoplex after intravenous administration in mice," *Journal of Controlled Release*, vol. 98, no. 1, pp. 157–167, 2004.
- [23] H. Kitani, T. Takenouchi, M. Sato, M. Yoshioka, and N. Yamanaka, "A novel isolation method for macrophage-like cells from mixed primary cultures of adult rat liver cells," *Journal of Immunological Methods*, vol. 360, no. 1-2, pp. 47–55, 2010.